# UNIVERSITAT POLITÈCNICA DE VALÈNCIA

ESCUELA TÉCNICA SUPERIOR DE INGENIERÍA DEL DISEÑO

Máster Universitario en Ingeniería Aeronáutica

## Trabajo de fin de máster

La organización de las grandes escalas en flujos de pared


Author:

Sergio Gandía Barberá

Supervisor:

Sergio Hoyas Calvo


Valencia, July 2018

# Abstract

The recent investigation of the turbulent features in flows dominated by a shear stress, like Couette flows, have proven the presence of strong and long unexpected turbulent structures. Despite different scientific publications have described these structures since the early nineties, little has been said about their stability and length. It has very recently been shown that the length of these structures grows with the Reynolds number, which makes in some cases the determination of their length beyond the possibilities of the largest supercomputers. On the other hand, these structures are curiously not present in pressure driven flows, such as Poiseuille flow.

The aim of this master's thesis is to analyse the stability of these large turbulent structures by adding a certain percentage of Poiseuille flow to each case until a pure Poiseuille flow is achieved. Thus, a stepped transition between both scenarios can be studied. Additionally, different domain sizes are employed in order to study the length of these turbulent features. Due to the potential extent of the structures studied, our biggest domain is indeed considered among the longest simulation channels in turbulence.

# Resumen

Las recientes investigaciones sobre las características de la turbulencia en flujos dominados por el esfuerzo cortante, como en los flujos de Couette, han demostrado la presencia de estructuras turbulentas extensas y persistentes. A pesar de que diversas publicaciones científicas han descrito estas estructuras desde el principio de los noventa, poco se ha dicho sobre su estabilidad y longitud. Hace poco se demostró que su longitud crece con el número de Reynolds, lo cual hace que casos con elevado número de Reynolds sobrepasen la capacidad de los supercomputadores más grandes. Por otra parte, curiosamente estas estructuras no están presentes en flujos regidos por un gradiente de presión, como el flujo de Poiseuille.

El objetivo de este TFM es analizar la estabilidad de estas grandes estructuras turbulentas. Para ello, se estudiarán diversos casos, los cuales cubren una transición escalonada desde un flujo de Poiseuille puro hasta un flujo de Couette puro. Además, dominios con diferentes tamaños se usarán en el estudio de la longitud de estas estructuras turbulentas. Debido a su posible longitud, nuestro dominio más grande está considerado actualmente como uno de los canales turbulentos más extensos.

# Resum

Les investigacions recents sobre les característiques de la turbulència en fluxos dominats per l'esforç tallant, com el flux de Couette, han demostrat la presència d'estructures turbulentes extenses i persistents. Encara que diverses publicacions científiques han descrit estes estructures des del principi dels noranta, poc s'ha dit sobre la seua estabilitat i longitud. De fet, fa poc s'ha desmostrat que la seua longitud creix amb el número de Reynolds; açò fa que casos amb un elevant número de Reynolds sobrepassen la capacitat de les supercomputadores més grans. Per altra part, curiosament estes estructures no estàn presents en els fluxos regits per un gradient de pressió, com és un flux de Poiseuille.

L'objectiu d'aquest TFM és analitzar l'estabilitat d'estes grans estructures turbulentes. Per a això, s'estudiaràn diversos casos, els cuals cobrixen una transició escalonada des d'un flux de Poiseuille pur fins un flux de Couette pur. A més, s'emplearàn dominis amb diferents tamanys en l'estudi de la longitud de les estructures turbulentes. Degut a la seua possible longitud, el nostre domini més gran està considerat actualment com un dels canals turbulents més extensos.

# Contents

# Chapter 1

# Introduction

An essential feature of turbulent flows is that the fluid velocity field varies significantly and irregularly in both space and time. When one imagines a turbulent flow, the first image that comes to the mind is an unsteady, irregular and chaotic flow. This idea is quite accurate indeed. As the instantaneous characterization of a flow gives little information, turbulence is best described through statistical techniques, which try to extract useful information from the chaos.

Broadly speaking, one can say if a flow is turbulent by measuring its Reynolds number. This non-dimensional number described in Eq. 1.0.1 compares the inertial forces (numerator) and the viscous forces (denominator). At low Reynolds numbers, where viscous forces are dominant, the flow becomes smooth, also known as laminar. On the other hand, at high Reynolds numbers, the predominant inertial forces produce chaotic eddies and flow instabilities. This case is called turbulent flow. In engineering, most flows are turbulent, being lubrication the only exception to this general rule.

In fluid mechanics, Reynolds number is employed to scale similar but different-sized flow situations. For instance, one can estimate the interaction between the air and an aircraft by measuring a scaled model, but ensuring a similar Reynolds number as in reality.

$$Re = \frac{\rho u L}{\mu} = \frac{u L}{\nu} \tag{1.0.1}$$

where:

- $\rho$ is the density of the fluid $[kg/m^3]$
- $u$ is the velocity of the fluid with respect to the object $[m/s]$
- $L$ is a characteristic linear dimension $[m]$
- $\mu$ is the dynamic viscosity of the fluid $[kg/\left(m \cdot s\right)]$
- $\nu$ is the kinematic viscosity of the fluid $[m^2/s]$

These characteristics were first observed by Osborne Reynolds in 1883, who also established that the transition between both types occurs at $Re \approx 2 \times 10^3$, in case of a flow

in a pipe. On the contrary, this value is approximately $Re \approx 5 \cdot 10^5$ for free-stream flow over a flat plate.

Since the kinematic viscosity $\nu = \mu/\rho$ of the air or water is small, at a moderate length $L$ or speed $u$, the Reynolds number is high enough for the flow to be turbulent. As a consequence, turbulent flows are present in our everyday surroundings. The smoke from a chimney, water flowing in a river or a strong wind are turbulent flow.

In order to describe the velocity fields as well as the fluid characteristics in a certain case, the Navier-Stokes equations were developed in the beginning of the XX century. See Eq. 1.0.2 for an incompressible case. These balance equations arise from applying Newton's second law to fluid motion, together with the assumption that the inertia in the fluid (left-side of the equation) is the sum of a diffusing viscous term (proportional to the gradient of velocity) and a pressure term; hence, describing viscous flow. Note that gravitational and external forces are neglected.

$$\frac{\partial u_i}{\partial t} + u_j \frac{\partial u_i}{\partial x_j} = -\frac{1}{\rho}\frac{\partial p}{\partial x_i} + \nu \frac{\partial^2 u_i}{\partial x_j^2} \tag{1.0.2}$$

In these equations, $i$ and $j$ are subscripts referred to Einstein summation convention. In Eq. 1.0.2, the subscript $i$ is a free index, which can take on the values 1, 2 and 3. Thus, Eq. 1.0.2 is in fact three separate equations.

In the previous equation, $\partial_t u$ is the non-stationary term, $u_j \frac{\partial u_i}{\partial x_j}$ is the convective term, $\frac{1}{\rho}\frac{\partial p}{\partial x_i}$ is related to the influence of the pressure gradient, and $\nu \nabla^2 u$ is the viscous term, which is related to the dissipation and controlled by the kinematic viscosity, $\nu$.

Despite more than one hundred years have passed since Navier-Stokes equations were released, the process of finding the solution of these equations is still one of the most important open problems in mathematics and physics. Even the existence and uniqueness of solutions is an open problem. Therefore, all the progress made up to now was acquired using experimental and numerical methods. This problem stems from a) the pressure term and b) the non-linearity of these equations, which is caused by the convective term. This term is, by the way, the main contributor to the turbulence in the equations.

Going deeper into turbulence organization, turbulent flows have complex characteristics that can not be appreciated with the naked eye, such as their wide variety of scales. From large eddies that fill the entire domain in Couette flows, to small and universal scales that escape from the visual range of the current measure devices.

## 1.1 Turbulent scales. Kolmogorov cascade

Kolmogorov described turbulence through vortexes with a wide variety of scales. His theory stated that the energy is introduced in the flow at the largest scales, where Reynolds number is high. Hence, the dissipation does not play a relevant role. Nevertheless, these vortexes are highly unstable, although nobody yet knows why, and they break into smaller vortexes, transferring completely the energy from one to the others. This process takes place until the scales of the eddies become small enough to locally achieve $Re \approx 1$, and the energy dissipation due to viscous effects becomes relevant.

The eddies in the largest size range are characterized by the length scale $l_0$, which is comparable to the flow scale $\mathcal{L}$. Their characteristic velocity $u_0 \equiv u(l_0)$ is on the order of the r.m.s. turbulence intensity $u'$. The Reynolds number of these eddies $Re_0 = u_0 l_0/\nu$ is therefore large, so the direct effects of viscosity are small, as stated. The length scale $l_0$ is commonly referred as integral scale in the literature, [1].

Then, the largest eddies become unstable after a certain time, which is similar to their wash-out time $T_0 = l_0/u_0$. Wash-out time is the time needed in order to cover the scale $l_0$ considering a speed $u_0$. Soon after, smaller eddies are created and they receive the energy of the bigger and unstable ones. This process is defined by the dissipation rate, $\varepsilon \sim u_0^2/T_0 = u_0^3/l_0$.

Finally, the Kolmogorov scale ($\eta$) describes at which moment the viscosity is relevant enough to dissipate the eddies instead of creating smaller ones. Hence, this scale is calculated by making the instability time of an eddy of size $l$, $T_l = l/u_l$, equal to the time required to dissipate that eddy, $T_\nu = l^2/\nu$.

$$\frac{\eta^2}{\nu} = \frac{\nu}{(\varepsilon\eta)^{1/3}} \rightarrow \eta = \left(\frac{\nu^3}{\varepsilon}\right)^{\frac{1}{4}} \tag{1.1.1}$$

See that in $T_l$ and $T_\nu$, longitude $l$ is substituted by Kolmogorov scale $\eta$. Moreover, $u_l$ is determined from the dissipation rate as $u_l = \sqrt[3]{\varepsilon\, l}$

According to the Kolmogorov hypotheses, at a high Reynolds number the turbulent scales can be classified in three different ranges, being $l$ the eddy size.

- Energy-containing range ($l > l_{EI}$): here the scales are comparable to the flow scale. The eddies located in this range are anisotropic and the turbulent velocity fields depend on each case. The demarcation parameter is defined as $l_{EI} = l_0/6$.

- Inertial subrange ($l_{EI} < l < l_{DI}$): in this subrange the transfer of energy to successively smaller scales occurs. It is part of the universal equilibrium range, so the statistics of the motions inside this range have a universal form that is uniquely determined by $\varepsilon$, independent of $\nu$, as viscous efforts are not relevant yet.

- Dissipation range ($l < l_{DI}$): dissipation occurs in this range, so Kolmogorov scale (Eq. 1.1.1) is contained. This range is also universal as the Inertial subrange, but now the universal form is determined by $\varepsilon$ and $\nu$.

For the sake of clarity, these ranges are graphically classified in Figure 1.1.

## 1.2 Numerical methods for turbulence resolution

The numerical simulation of turbulent flows, also known as CFD (Computational Fluid Dynamics), is still one of the most difficult problems in physics. It is generally admitted that a simulation can be considered at three levels of detail. As detail increases, simulations become more computationally demanding, and it is also the case of the initialization. Moreover, each level tackles the equations in a different way.

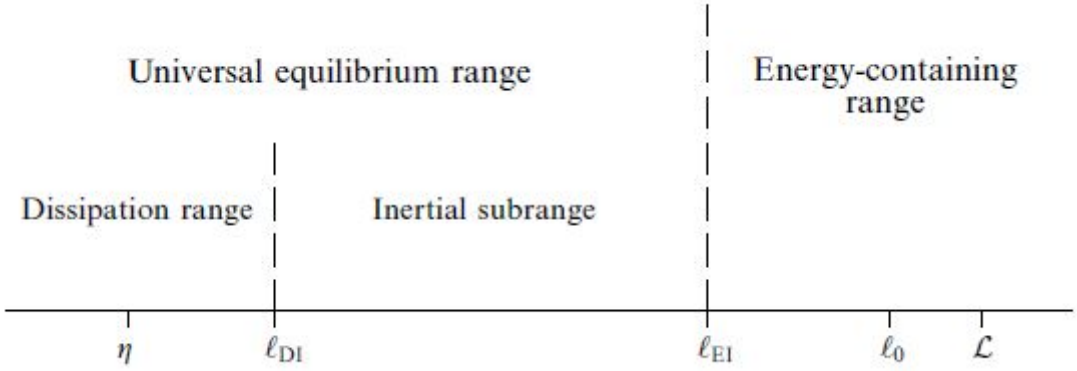


Figure 1.1: Various lengthscales and ranges for eddy sizes $l$ at high Reynolds number.

The lowest level corresponds to RANS (Reynolds Averaged Navier Stokes), in which Reynolds decomposition is applied to the Navier-Stokes equations. The objective of RANS is to compute the Reynolds stresses.

That is, the decomposition of the velocity $U(\vec{x},t)$ into its mean $\langle U(\vec{x},t)\rangle$ and its fluctuation $u(\vec{x},t)$, as follows

$$U(\vec{x},t) = \langle U(\vec{x},t)\rangle + u(\vec{x},t) \tag{1.2.1}$$

Employing Eq. 1.2.1 in Eq. 1.0.2 is complex and it is fully detailed in [1], pages 83, 84 and 85. The resulting equations are known as *Reynolds equations*.

$$\frac{\overline{D}\langle U_j\rangle}{\overline{D}t} = -\frac{1}{\rho}\frac{\partial\langle p\rangle}{\partial x_j} + \nu\,\nabla^2\langle U_j\rangle - \frac{\partial\langle u_i u_j\rangle}{\partial x_i} \tag{1.2.2}$$

See that on the right hand side of Eq. 1.2.2, the second term is the viscous stress. However, the third term is not a stress at all, but namely a re-worked version of the fluctuating contribution to the non-linear acceleration terms; that is, $\nabla^2\langle U_j\rangle$. This term is known as Reynolds stress.

In appearance, the Reynolds equations (Eq. 1.2.2) and the Navier-Stokes equations (Eq. 1.0.2) are the same, except for the Reynolds stress, $\langle u_i u_j\rangle$. That is a crucial difference. Physically, the Reynolds stress stems from momentum transfer by the fluctuating velocity field.

Even though we can assume it is a stress, the physics which give rise to it are very different from the viscous stress. The viscous stress is related to flow properties through constitutive equations. This approach works because constitutive equations average over characteristic length and time scales much smaller than those of the flows we are interested in. Unfortunately, this is not the case of Reynolds stress, so closure equations become complex[1].

The presence of the Reynolds stresses introduce new unknowns to the equations, leading to an unbalance between number of equations and unknowns. To be exact, there

[1]https://www.cfd-online.com/Wiki/Introduction_to_turbulence/Reynolds_averaged_equations

are six individual stress components we must deal with: $\langle u^2 \rangle$, $\langle v^2 \rangle$, $\langle w^2 \rangle$, $\langle uv \rangle$, $\langle uw \rangle$, $\langle vw \rangle$. Hence, the Reynolds equations are not closed, and the Reynolds stresses must be determined through empirical/theoretical turbulence models.

As a consequence, all the turbulent fluctuations are modelled, requiring the lowest resolution of the three methods. In this approach only the geometric aspects of the mean flow are solved, and all the unsteady eddies of the flow are included in the model. As the largest eddies of the flow are not universal and depend on the particular mechanism of energy injection, as stated in Section 1.1, each turbulence model must be adapted to each particular case.

There are three main categories of RANS-based turbulence models:

1. Linear eddy viscosity models
2. Nonlinear eddy viscosity models
3. Reynolds stress model (RSM)

In Linear eddy viscosity models, Reynolds stresses are modelled by a linear constitutive relationship with the mean flow straining field, as:

$$-\rho\langle u_i u_j \rangle = 2\mu_t S_{ij} - \frac{2}{3}\rho k \delta_{ij} \tag{1.2.3}$$

where

- $\mu_t$ is the turbulence viscosity (also known as eddy viscosity).
- $k = \frac{1}{2}\left(\langle u^2 \rangle + \langle v^2 \rangle + \langle w^2 \rangle\right)$ is the turbulent kinetic energy.
- $S_{ij} = \frac{1}{2}\left[\frac{\partial U_i}{\partial x_j} + \frac{\partial U_j}{\partial x_i}\right] - \frac{1}{3}\frac{\partial U_k}{\partial x_k}\delta_{ij}$ is the mean strain rate.

Depending on the empirical or transport equations employed to compute the eddy viscosity coefficient, there are different subcategories within this approach. For instance, the distinguished $k - \varepsilon$ model.

Nevertheless, linear eddy-viscosity models (EVM) are prone to calculate poor approximation in complex flows. For instance, in case of a curved domain a linear EVM does not reproduce the asymmetry in the velocity profile, because of the stress-strain relation employed for Reynolds stress. Moreover, in stagnation regions linear EVM tend to overestimate turbulence energy levels, by estimating incorrect normal stresses.

In recent times, non-linear eddy-viscosity models have received significant interest, as they offer better estimations than linear EVMs, but with only a moderate increase in computing resources. This approach considers a nonlinear relationship $f_{nl}$ between Reynolds stress, the mean strain rate $S_{ij}$ and the mean vorticity $\Omega_{ij}$, as:

$$-\rho\langle u_i u_j \rangle = 2\,\mu_t\, f_{nl}\left(S_{ij},\, \Omega_{ij}\right) \tag{1.2.4}$$

Finally, Reynolds Stress Models (RSM) are higher level turbulence closures and represent the most complete classical turbulence model. Here, model transport equations

are solved for the individual Reynolds stresses $\langle u_i u_j \rangle$ and for the dissipation $\varepsilon$. As a consequence, the turbulent-viscosity hypothesis is no longer needed. This fact removes the major defect of the eddy-viscosity models described before, since this convenient closure to the Reynolds equations shows deficiencies in many flows due to its intrinsic and specific assumptions. The interested reader is referred to the classic book of Pope [1], section 10.1.

For this approach, the exact transport equation for Reynolds stresses is obtained from the Navier-Stokes equations as specified in Pope [1] on page 319, resulting:

$$\frac{\overline{D}}{\overline{D}t}\langle u_i u_j \rangle + \frac{\partial}{\partial x_k} T_{kij} = P_{ij} + R_{ij} - \varepsilon_{ij} \tag{1.2.5}$$

In RSM, the known variables are $\langle U \rangle$, $\langle p \rangle$, $\langle u_i u_j \rangle$ and $\varepsilon$. Hence, in Eq. 1.2.5 both the mean-flow convection, $\overline{D}/\overline{D}t\langle u_i u_j \rangle$, and the production tensor $P_{ij}$, are in closed form. However, models for the dissipation tensor $\varepsilon_{ij}$, the pressure rate of strain tensor $R_{ij}$, and the Reynolds-stress flux $T_{kij}$ are required. For detailed information, we refer the reader to Pope [1], page 387.

The approach adopted in RSM makes it good for accurately predicting complex flows; that is, flows with streamlines curvature, swirl, rotation and high strain rates. I.e, cyclone flows, secondary flows and separation. However, the large amount of still necessary modelling and the complexity of this approach, makes it the least used of the RANS methods.

Going one step further, the second level of detail corresponds to the Large Eddy Simulation (LES). This model is based on space-filtered equations. Also this model is not time-averaged, and time dependent calculations are performed. Here the largest eddies of the flow, which depend on the particular case in study, are simulated directly, while the smallest scales are isolated by means of a filter and modelled as in RANS. This idea stems from the fact that small scales in inertial subrange or dissipative range are isotropic and universal.

The space-filtering can be conducted implicitly employing the domain grid as a filter itself, or explicitly through different techniques. For example, Fourier filter or subgrid filter, such as Smagorinsky, which removes high wave-numbers, corresponding to small scales. These small scales are therefore modelled.

Regarding computational expense, LES lies between Reynolds-stress models and DNS, and it is motivated by the limitations of each of these approaches. Because the large-scale unsteady motions are represented explicitly, LES can be expected to be more accurate and reliable than Reynolds-stress models for flows in which large-scale unsteadiness is significant, such as the flow over bluff bodies or meteorological simulations.

Since LES model is complex and will not be employed in this thesis, it will be no longer explained. For a deeper explanation, we refer the reader to [1], chapter 13.

The last level of detail is achieved through Direct Numerical Simulation (DNS), in which the equations are solved by a numerical scheme without any other approximation. This is the technique used in this project. With high enough computational power, the error can be reduced as much as is wanted. Nevertheless, the computational cost is very high. This depends on the Reynolds number. Every time the Reynolds is doubled, the cost of the simulation is multiplied by 7 approximately. This exponential grow makes still

impossible the simulation of large Reynolds, and only very simple geometries have been characterized with a good detail.

As a consequence, this method is not practical for industrial applications. Moreover, the grid spacing in the domain must accomplish certain precision requirements in order to solve both the large and small scales of turbulence.

The range of scales solved in each level of detail is depicted in Figure 1.2. Therefore, the resolution method for a specific turbulent flows is based on which scales should be calculated and which ones should be modelled.

More information about the DNS scheme used in our simulation is provided in the Chapter 2. Now, a short description of the classical Couette and Poiseuille flows is introduced in the following Section 1.3.

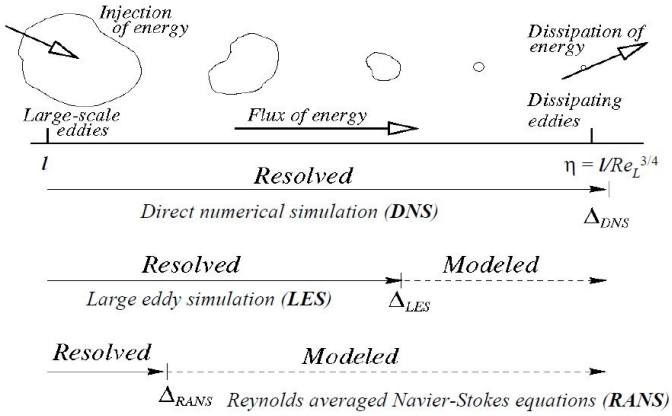


Figure 1.2: Diagram of the resolved/modelled turbulent scales at each level.

## 1.3 Description of Couette and Poiseuille flows

The main characteristics of the flows, that will be analysed in this master's thesis, are now presented. For the sake of understanding, both flows are initially described as laminar.

Both Couette and Poiseuille flows are steady flows between two infinitely long, parallel plates at a fixed distance. The difference is that in Couette flow the upper wall has a velocity $U$ in the direction parallel to the bottom wall. As a result, the driving force is the moving upper wall due to the effect of viscosity, but no pressure gradient in the fluid is applied. In contrast, in Poiseuille flow both walls are at rest, and the flow movement is caused by an external negative pressure gradient, $dp/dx < 0$, in the direction parallel to the walls.

The theoretical solution for a laminar Couette flow is obtained through the Navier-Stokes equations (Equation 1.0.2) for an incompressible fluid of constant and uniform viscosity as well as no gravitational potencial. It can be shown that this problem can be reduced to a one-dimensional problem in this case.

The no-slip condition at the stationary wall is specified through the boundary conditions. The pressure term in the Navier-Stokes equation can be removed. At the moving

wall ($y = h$), the boundary condition is $u_x(h) = U$. According to that, the stream-wise velocity is described as:

$$u_x\,(y) = \frac{U \cdot y}{h} \tag{1.3.1}$$

As there is a first order relationship between $u_x$ and $y$, the velocity profile is linear. (Figure 1.3). On the other hand, laminar Poiseuille flow is solved using the same equation 1.0.2 at $i = j = 1$. However, no-slip boundary condition is applied at both walls. The presence of a pressure gradient gives a different result for the profile of the stream-wise velocity, which is:

$$u_x = \frac{h^2}{2\mu}\frac{dp}{dx}\left(1 - \frac{y^2}{h^2}\right) \tag{1.3.2}$$

where $-h \leq y \leq h$.

As one can see, here there is a second order relationship between $u_x$ and $y$, so the velocity profile is described by a parabola. See Figure 1.3.

Applying the definition of shear stress in fluid mechanics (Eq. 1.3.3, left) to the Eq. 1.3.2, the result is shown in Eq. 1.3.3, right. As a matter of curiosity, the defined integral along the y-domain of the shear stress in Poiseuille flow is 0. That is, the shear force is balanced along the stream-wise velocity profile.

$$\tau = \mu \cdot \frac{\partial u}{\partial y} = \frac{1}{2} \cdot \frac{dp}{dx} \cdot (2y - h) \tag{1.3.3}$$

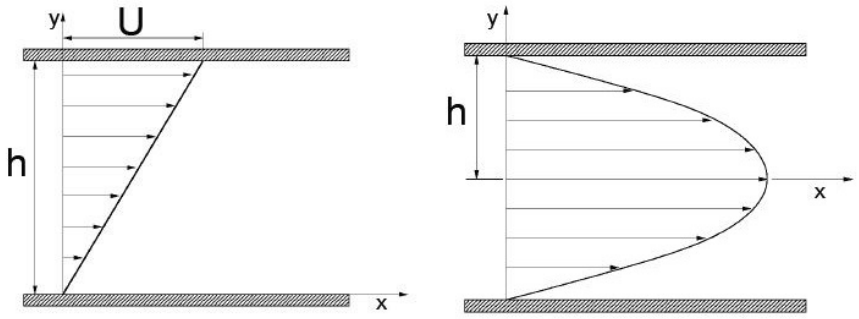


Figure 1.3: Laminar stream-wise velocity profile in Couette (left) and in Poiseuille (right) flows.

The analysis in this master's thesis is conducted through the transition from a turbulent Couette flow to a turbulent Poiseuille flow. Therefore, the stream-wise velocity profile for a pure Couette flow ($P = 0$), as well as for a case, where both flows are applied ($P > 0$) is defined in Figure 1.4. There, the profile in case of a positive pressure gradient ($P < 0$), $dp/dx > 0$, is also represented, but this case is less relevant.

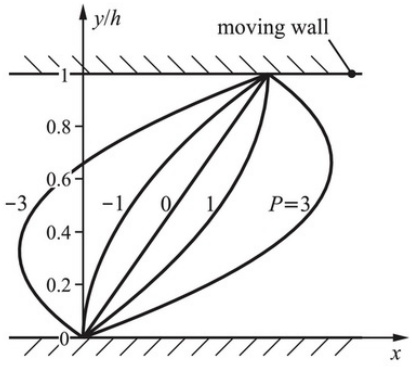


Figure 1.4: Stream-wise velocity profile in case of Couette with pressure gradient. Image from Pope [1].

## 1.4 Use of canonical turbulent wall flows

In contrast to the free shear flows, which are not explained in this study, most turbulent flows are influenced by the presence of a wall. Among the examples one can distinguish internal flows, such as flows through ducts and pipes, and external flows, such as the flow around an aircraft.

In a first approach, all these flows are studied in simple geometries in order to extract relevant information about their canonical turbulent structures near the wall. The interest stems from studying how the presence of a wall influences the turbulence in different cases. As stated by Pope [1] in page 264, these simple flows are of practical importance and played a prominent role in the historical development of the study of turbulent flows.

The used geometries are channel flows, pipe flows and flat-plate boundary layers. A characteristic of these domains is that the mean velocity vector is almost parallel to the wall, and the near-wall behaviours in each of these cases are very similar.

Couette and Poiseuille flows are generally studied employing DNS in channel domains, as it is easy to set a relative velocity between walls. Moreover, both flows are classical fluid mechanics problems, which are specially simple to model.

Poiseuille flows are employed to study the turbulent features and vortex organizations in the near-wall layers: viscous layer, buffer layer and logarithmic layer, if present. J. Jimenez [2] performed an extensive study in this direction. On the other hand, turbulent Couette flow studies point to the very large turbulent structures in the channel center, as well as their influence on the near-wall turbulence, as Pirozzoli et al. [3] did.

Aside from the conclusions extracted on each flow, the results are usually employed to improve and check other turbulent models, which are of course less accurate than a DNS. For example, for developing more accurate closure equations in RANS models.

For more information, the interested reader is referred to Pope [1], chapter 7.

# Chapter 2

# Direct Numerical Simulation. DNS

Among the numerical methods introduced in Section 1.2, we have selected Direct Numerical Simulation for our cases, because our aim is to analyse all the turbulent scales in the Couette, Poiseuille flows and their transition; that is, from the biggest ones in the center of the channel, to the smallest ones near the walls. All the research conducted in this field has been carried out through experiments [4, 5], which allow a high Reynolds number, and DNS [6, 7, 8], which is limited to a moderate Reynolds, whose maximum is currently located around $Re_\tau = 8000$ [9]. It is worth to mention that most of these works have been done by aerospace engineers of in AE-related schools and research center.

Employing DNS introduces several complexities to the resolution, which were explained before. Moreover, the definition of suitable initial and boundary conditions is fundamental in order to reduce the convergence time, and ensure a final solution independent of them.

The type of domain employed in our study is channel flow. Among the characteristic of this domain we find two advantages. First, wall-parallel dimensions are assumed periodical in their boundaries. Fortunately, this condition is easy to implement. Second, the flow is statistically fully developed in stream- and spanwise directions. Moreover, anisotropy in wall-normal direction allows us to study other turbulent cascades beyond the classical Kolmogorov cascade (Section 1.1). The interested reader is referred to Tennekes and Lumley [10].

In the wall normal direction, there are two walls that denote the beginning and end of the domain in this direction. Hence, no-penetration and no-slip conditions are implemented here. Considering the turbulence as homogeneous in this direction is consequently infeasible [1].

The numerical scheme employed in our simulations is explained in Section 2.1. This approach was first introduced by Kim, Moin and Moser [11], and it is specific for turbulent channel flows.

In addition, the code of the numerical scheme used for this work has been employed in different works for several different boundary conditions, [12, 13, 14, 15, 16, 17], so it will not be further validated.

## 2.1 Numerical Scheme

The scheme starts from the original Navier-Stokes equations for an incompressible flow, which are:

$$\nabla \cdot \vec{v} = 0 \tag{2.1.1}$$

$$\rho \frac{\partial \vec{v}}{\partial t} + \rho \vec{v} \cdot \nabla \vec{v} = -\nabla p + \nabla \tau' \tag{2.1.2}$$

where $\tau'$ is the viscous stress tensor, which is defined by the Navier-Poisson law. See Eq. 2.1.3. Notice that the mass forces per volume, $\rho \vec{f_m}$, are not included in Eq. 2.1.2.

$$\tau'_{ij} = 2\mu\gamma_{ij} + \left(\mu_v - \frac{2}{3}\mu\right)(\nabla \cdot \vec{v}) \tag{2.1.3}$$

here $\gamma_{ij}$ is strain-rate tensor, and $\delta_{ij}$ is the Dirac delta.

Considering an isotropic and incompressible fluid, the volumetric viscosity ($\mu_v$) and the divergence of the velocity $\nabla \cdot \vec{v}$ is zero in Eq. 2.1.3. So, now the viscous stress tensor is defined as:

$$\tau'_{ij} = \mu\left(\partial_i v_j + \partial_j v_i\right) \tag{2.1.4}$$

where $i$ and $j$ are subscripts referred to Einstein summation convention.

Despite viscosity $\mu$ is generally dependent from the temperature, it will be supposed that its variations in our desired range of temperatures can be neglected.

After these steps, the initial Navier-Stokes (Eq. 2.1.2) equation converts to:

$$\frac{\partial \vec{v}}{\partial t} + \vec{v} \cdot \nabla \vec{v} = -\frac{1}{p}\nabla p + \nu \nabla^2 \vec{v} \tag{2.1.5}$$

Until now the steps were quite straightforward. However, due to numerical considerations and advantages, that will be further explained, the equation system made up of the Eq. 2.1.1 and Eq. 2.1.5 must be transformed into two equation. One for the Laplacian of the wall-normal velocity component, $\phi = \nabla^2 v$, and another for the wall-normal vorticity component, $\omega_y$. These characteristics were developed by Kim et al [11].

Before starting the transformation, a new parameter called *helicity* is introduced. This parameter stems from the vectorial product of the velocity and vorticity.

$$\vec{H} = \vec{v} \times \vec{\omega} \tag{2.1.6}$$

where $\vec{H} = (H_1, H_2, H_3)$.

Writing Eq. 2.1.5 as non-dimensional and applying the definition of *helicity* (Eq. 2.1.6) to the convective term, $\vec{v} \cdot \nabla \vec{v}$, the result is:

$$\frac{\partial \vec{v}}{\partial t} + \frac{1}{2}\nabla\left(\vec{v} \cdot \vec{v}\right) - \vec{H} = -\frac{1}{\rho}\nabla p + \frac{1}{Re_b}\nabla^2 \vec{v} \tag{2.1.7}$$

Notice that in Eq. 2.1.7 the variables are no longer dimensional despite their symbols remain the same. Additionally, the half-height of the channel, $h$, and the stream-wise bulk velocity, $u_b$ (Eq. 2.1.8), were employed in order to develop the non-dimensional equation, as well as the Reynolds bulk, $Re_b = u_b\, h/\nu$.

$$u_b = \frac{1}{2h}\int_{-h}^{h} \langle U \rangle \, dy \tag{2.1.8}$$

The equations for $\phi$ and $\omega_y$ will be deducted from Eq. 2.1.7. The first step is to calculate the divergence of Eq. 2.1.7 in order to develop an equation for the divergence of $\vec{H}$. Additionally, the divergence of the gradient is called Laplacian $\nabla \cdot \nabla = \nabla^2$. Note that the divergence is commutable in Laplacians and time derivatives, so the condition imposed by the mass conservation in incompressible flows, $\nabla \cdot \vec{v} = 0$, is achieved.

$$0 + \frac{1}{2}\nabla^2 \left(\vec{v} \cdot \vec{v}\right) - \nabla \cdot \vec{H} = -\frac{1}{\rho}\nabla^2 p + 0 \;\Rightarrow\; \nabla \cdot \vec{H} = \frac{1}{2}\nabla^2 \left(\vec{v} \cdot \vec{v}\right) + \frac{1}{\rho}\nabla^2 p \tag{2.1.9}$$

Moreover, the Laplacian of Eq. 2.1.7 is calculated.

$$\frac{\partial}{\partial t}\nabla^2 \vec{v} + \nabla\left(\frac{1}{2}\nabla^2 \left(\vec{v} \cdot \vec{v}\right)\right) - \nabla^2 \vec{H} = -\nabla\left(\frac{1}{\rho}\nabla^2 p\right) + \frac{1}{Re_b}\nabla^4 \vec{v} \tag{2.1.10}$$

and adding the result (right) of Eq. 2.1.9 to the Laplacian of Eq. 2.1.7, gives:

$$\frac{\partial}{\partial t}\nabla^2 \vec{v} + \nabla\left(\nabla \cdot \vec{H}\right) - \nabla^2 \vec{H} = \frac{1}{Re_b}\nabla^4 \vec{v} \tag{2.1.11}$$

On the other hand, the curl of Eq. 2.1.7 is calculated:

$$\frac{\partial}{\partial t}\vec{\omega} + \frac{1}{2}\nabla \times \nabla \left(\vec{v} \cdot \vec{v}\right) + \nabla \times \vec{H} = -\frac{1}{\rho}\nabla \times \nabla p + \frac{1}{Re_b}\nabla^2 \vec{\omega} \tag{2.1.12}$$

Considering that the curl of a gradient is null, this equation becomes as follows:

$$\frac{\partial}{\partial t}\vec{\omega} + \nabla \times \vec{H} = \frac{1}{Re_b}\nabla^2 \vec{\omega} \tag{2.1.13}$$

Note that Eq. 2.1.11 and Eq. 2.1.13 are vectorial equations, but our interest is focused on the Laplacian of the wall-normal velocity component and on the wall-normal vorticity component, as explained before. Therefore, the wall-normal component of these equations is considered, and described as:

$$\frac{\partial}{\partial t}\phi = h_v + \frac{1}{Re_b}\nabla^2 \phi \tag{2.1.14}$$

$$\frac{\partial}{\partial t}\omega_y = h_g + \frac{1}{Re_b}\nabla^2 \omega_y \tag{2.1.15}$$

$$h_v = -\frac{\partial}{\partial y}\left(\frac{\partial H_1}{\partial x} + \frac{\partial H_3}{\partial z}\right) + \left(\frac{\partial^2}{\partial x^2} + \frac{\partial^2}{\partial z^2}\right) H_2 \tag{2.1.16}$$

$$h_g = \frac{\partial H_1}{\partial z} - \frac{\partial H_3}{\partial x} \tag{2.1.17}$$

According to Eq. 2.1.6, the *helicity* components are defined as:

$$\begin{aligned} H_1 &= v \cdot \omega_z - w \cdot \omega_y \\ H_2 &= w \cdot \omega_x - u \cdot \omega_z \\ H_3 &= u \cdot \omega_y - v \cdot \omega_x \end{aligned} \tag{2.1.18}$$

where $u$, $v$ and $w$ are the stream-wise, wall-normal and span-wise velocity components, respectively.

The system of equations is completed when the equations that relate $\phi$ and $\omega_y$ to the velocity and vorticity components are introduced.

$$\nabla^2 v = \phi \tag{2.1.19}$$

$$\frac{\partial u}{\partial x} + \frac{\partial w}{\partial z} = -\frac{\partial v}{\partial y} \tag{2.1.20}$$

$$\frac{\partial u}{\partial z} - \frac{\partial w}{\partial x} = \omega_y \tag{2.1.21}$$

$$\frac{\partial \omega_x}{\partial x} + \frac{\partial \omega_z}{\partial z} = -\frac{\partial \omega_y}{\partial y} \tag{2.1.22}$$

$$\frac{\partial \omega_z}{\partial x} - \frac{\partial \omega_x}{\partial z} = \phi \tag{2.1.23}$$

The advantages of this method are:

- The pressure is no longer required in order to solve the equations.
- Only two complex equations are needed to calculate $\phi$ and $\omega_y$. Then, the three velocity components are easily integrated. Hence, the execution becomes at least one third faster than solving an equation for each velocity component.

Regarding the selection of the solved variables, $\phi$ and $\omega_y$ were the only ones that gave the previously described advantages.

For the numerical scheme resolution, the spatial discretization uses dealiased Fourier expansions in $x$ and $z$, and seven-point compact finite differences in $y$, with fourth-order consistency and extended spectral-like resolution [18]. The temporal discretization is a third-order semi-implicit Runge-Kutta scheme [19].

## 2.2 Boundary Conditions

### At the walls

As depicted in Figure 1.3, the Couette flows and Poiseuille flows are enclosed by two walls in the Y-direction. However, in case of a Couette flow, the upper wall has a relative velocity in the wall-parallel direction, $U_W$, in comparison to the bottom wall.

Hence, the boundary condition of the velocity at the moving wall is $\vec{u}|_W = (U_W, 0, 0)$, where $U_W$ is 0 if it is a pure Poiseuille flow.

As a consequence, the velocity derivatives in stream-wise and span-wise directions are neglected at the wall. This fact provokes that, due to the Mass Conservation (Eq. 2.1.1), the derivative $\partial v/\partial y = 0$ at the walls. Additionally, the wall-normal component of the vorticity (Eq. 2.1.21) is 0 at the walls.

In case of a transition between Couette and Poiseuille, $U_W$ is not nullified and there is a negative pressure gradient, $-\partial p/\partial x$. At every case, despite the flow is driven by a constant velocity of the upper wall and/or a pressure gradient, selected parameters ensure that the bulk Reynolds number $Re_b = u_b\, h/\nu$ remains constant at approximately $Re_b = 2250$. For $u_b$ definition, see Eq. 2.1.8.

According to Pope [1] (page 266), the flow is laminar for $Re_b < 1350$, and fully turbulent for $Re_b > 1800$, although transitional effects are evident up to $Re_b = 3000$.

### At the parallel directions to the walls

The parallel directions to the walls are considered periodicals; so the longest wave-length of the structures in streamwise and spanwise direction is constrained by the domain length, $L_x$ and $L_z$, respectively. This fact must be taken into account while analysing the longest wave-lengths in the stream-wise direction, which take place in pure Couette flows. It is probed that periodical boundaries increase the coherence of these structures if the length of the domain is too short [8]; that is, in case their wave-lengths are similar to the streamwise size of the domain.

Due to the same periodical conditions and constant spacing (See Chapter 3) in $x$ and $z$ directions, the spatial discretization of the Numerical Scheme (Section 2.1) uses dealiased Fourier expansions. As this is not the case in $y$ direction, the discretization is not the same.

## 2.3 Initial Conditions and Steady-state

In every simulation, the flow had to evolve from an initial file, which has been taken from previous different simulations. The code was run until a transition phase was passed, and the flow adjusted to the new set of parameters. The transition is characterized by, among other variables, the value of the averaged total shear stress along the wall-normal dimension.

After estimating the averaged equations of Navier-Stokes, adapted to a Couette flow, we obtain the expression in Eq. 2.3.1. This is broadly known as the conservation of the mean momentum for C- flows. Physically, this equality states that the total shear flow in wall units contains two parts: one defined by the wall effect, and another defined by the velocity transmission from $u$ to $v$.

Once this parameter reaches a plateau at 1, statistics are collected. This quantity was confirmed in other calculations, such as in M. Lee and Moser [8] and Avsarkisov et al. [14].

$$\tau^{+}_{total} = \left\langle \frac{\partial u}{\partial y} \right\rangle^{+} - \langle u'v' \rangle^{+} = 1 \tag{2.3.1}$$

As is common in wall-bounded turbulence, the superscript + designates a quantity normalized in wall units; i.e. normalized by $u_\tau$ (See Eq. 3.0.2) and $\nu$.

The results on Eq. 2.3.1 of Avsarkisov et al. [14] are depicted in Figure 2.1. Here we can see a constant value at 1 for $\tau^{+}_{total}$, and a variable value of $\langle u'v' \rangle^{+}$ near the wall, as expected. Notice that diverse Couette flows at friction Reynolds numbers (Eq. 3.0.1) from 125 to 550 are represented using different colors. As $Re_\tau$ increases, $\langle u'v' \rangle^{+}$ reaches sooner a constant value.

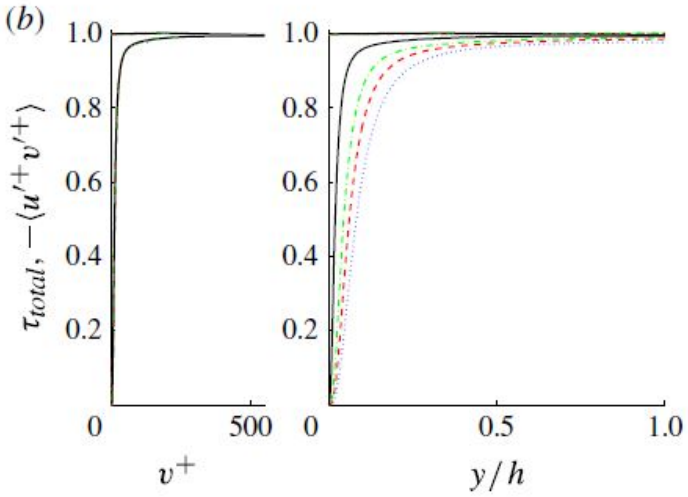


Figure 2.1: Total shear and Reynolds stresses of Couette flows in inner and outer scales at diverse $Re_\tau$. Extracted from Avsarkisov et al. [14].

# Chapter 3

# Description of the cases

Turbulent channel flows, as it is the case in this work, are studied generally through DNS since the first analysis conducted by Kim, Moin and Moser [11]. Once stated the type of flow, such as C-flow, P-flow or transition, each study is basically described through its friction Reynolds number, $Re_\tau$, and the size of the domain, specially in stream- ($L_x$) and spanwise ($L_z$) directions.

The friction Reynolds number is described as,

$$Re_\tau = \frac{u_\tau h}{\nu} \tag{3.0.1}$$

where:

- $u_\tau$ is the shear velocity, defined in Equation 3.0.2.
- $h$ is the half-height of the channel
- $\nu$ is the kinematic viscosity.

$$u_\tau = \sqrt{\frac{\tau}{\rho}} = \sqrt{\nu \left.\frac{\partial U}{\partial y}\right|_{y/h=-1}} \tag{3.0.2}$$

In this study, the shear velocity at the stationary wall is $u_\tau^s = 0.0525\, m/s$, and the friction Reynolds number is 125.

See also that according to Eq. 3.0.1 and the definition of the dimensionless wall distance, $y^+ = (u_\tau y)/\nu$, the relation in Eq. 3.0.3 is a useful tool to translate wall-units into physical units, and vice versa.

$$\frac{y^+}{Re_\tau} = \frac{y}{h} \tag{3.0.3}$$

For the study of the stability and origin of the longest coherent structures in Couette flows, a DNS dataset, which covers a stepped transition between Couette (C-flow) and Poiseuille (P-flow) was calculated. Each case is identified by an specific name, which describes the Couette and Poiseuille quantity present in the flow. The name is $CxxPzz$,

where $xx$ goes from 00 (no shear) to 10 (pure C-flow), and $zz$ is defined as $zz = 10 - xx$. Hence, pure Couette is called C10P00, pure Poiseuille is called C00P10, and both flows being same relevant is named as C05P05.

As briefly commented at the beginning of Chapter 2, all our simulations are performed in channel domains. This geometry is usually employed for canonical turbulent wall flows, as well as boundary layers and pipe flows. In our domains, axis X is parallel to the streamwise flow, axis Y is normal to the walls, and axis Z is parallel to the walls and normal to the streamwise flow. Their mean velocity components are $U$, $V$ and $W$, respectively. This way, $u'$, $v'$ and $w'$ are their respective fluctuation terms, according to Reynolds decomposition (Equation 1.2.1). Moreover, we assume that the bottom wall stays at $y/h = -1$, the upper wall at $y/h = 1$.

Our database was calculated in two domains. First one is a short domain, whose dimensions, described as $L_x \times L_y \times L_z$, are $16\pi h \times 2h \times 6\pi h$. On the contrary, a very long computational domain was also employed, whose dimensions are $128\pi h \times 2h \times 6\pi h$. Note that due to periodical boundary conditions as said in Section 2.2, the length and width of the domain is expressed in terms of $n$ times $\pi$ and multiplied by the half-height of the channel, $h$.

The simulation of pure Couette flow at this low Reynolds number is thus comparable to other simulations made by Tsukahara et al.[20] and Bernardini et al.[21]. Nevertheless, the streamwise size of the boxes ($L_x$) must be taken into account while comparing the results. Bernardini [21] performed DNS at $Re_\tau = 167$ in a box ($12\pi h \times 2h \times 4\pi h$). On the contrary, Tsukahara [20] performed DNS at $Re_\tau = 126$ in several boxes up to ($64h \times 2h \times 6h$). Pirozzoli et al. in a very interesting paper, [3], studied the transitions from C- to P- Flows at $Re_\tau = 250$. They related the absence of true large-dynamics scale for the P-flows to the lack of significant transport of turbulent kinetic energy. However, their box had a length of only $12\pi h$, so the largest structures of C-flows could not be studied in large.

Therefore, as the largest structures of C-flow could not be identified in the short boxes of other studies, we employed a very large domain in order to succeed in our analysis. Moreover, we want to analyse the differences in the results of a too short and an adequate domain.

Regarding the spacing on the domain, it remains constant along the wall-parallel directions; that is, the values are $\Delta x^+ \simeq 9.4$ and $\Delta z^+ \simeq 4.7$.

The wall-normal grid spacing is adjusted to keep the resolution at $\Delta y = 1.5\eta$, i.e., approximately constant in terms of the local isotropic Kolmogorov scale $\eta = (\nu^3/\epsilon)^{1/4}$, see Eq. 1.1.1. In wall units, $\Delta y^+$ varies from 0.83 at the wall, up to $\Delta y^+ \simeq 2.3$ at the centreline.

Once the cases are described, their mean velocity $U$ as well as velocity fluctuations and Reynolds stresses are discussed in the following section; that is, their one-point statistics. For the sake of clarity, only some of the cases are represented; however, they cover the whole transition between C- and P- flows. Additionally, the domain employed is the small one, because it is enough in order to ensure the independence of the results from the domain size, as it is stated by Lozano-Durán and Jimenez [22].

## 3.1 Mean velocity, fluctuations and Reynolds stress

Before describing the graphics that show the one-point statistics along the transition, each case is described in Table 3.1. Note that the line related to each case is kept in all the Figures in this section, so no further legend will be used.

Two different Reynolds numbers are given depending on the local $u_\tau$ at the moving (third column) or the stationary (fourth) wall. $N_x, N_y, N_z$ are number of collocation points in physical space. The last two columns denote the computational time span while statistics were taken in wash-outs ($U_b/L_x$) and eddy turn-overs ($u_\tau/h$). $T$ is the computational time spanned by those fields.

The velocity fluctuations $u'^+_{rms}$, $v'^+_{rms}$ and $w'^+_{rms}$, as well as the Reynolds stress $\overline{u'v'}^+$ are depicted in Figures 3.1 and 3.2. The overline illustrate an averaged quantity. All of them start on the stationary wall.

In every case, there is a minor sensitivity to wall motion near the stationary wall; hence, $u'^+_{rms}$ and $v'^+_{rms}$ collapse perfectly up to $y^+ \approx 25$; that is, in the viscous and buffer layers. On the contrary, $w'^+_{rms}$ shows at $y^+ \approx 7$ variations among the cases. This result was observed by Pirozzoli et al. [3].

| Case | Line | $Re^s_\tau$ | $Re^m_\tau$ | $N_x$ | $N_y$ | $N_z$ | $TU_b/L_x$ | $Tu_\tau/h$ |
|---|---|---|---|---|---|---|---|---|
| C10P00 | —○— | 132 | 132 | 512 | 151 | 383 | 8.9 | 188 |
| C08P02 | ····· | 133 | 83 | 512 | 151 | 383 | 10.9 | 235 |
| C06P04 | – – – – | 135 | 13 | 512 | 151 | 383 | 11.2 | 243 |
| C04P06 | —·— | 137 | 69 | 512 | 151 | 383 | 19.4 | 430 |
| C02P08 | ——— | 142 | 102 | 512 | 151 | 383 | 16.8 | 384 |
| C00P10 | —□— | 147 | 147 | 512 | 151 | 383 | 11.1 | 264 |

Table 3.1: Parameters of the simulations. Line shapes given in the second column are used to identify the cases through all the figures of the present section.

Additionally, in this paper Pirozzoli et al. analyses these fluctuations near the moving wall; in that case, curves show a larger spread and stronger deviations from the canonical channel behaviour. One can predict this result from the strong deviation among cases in Reynolds stress (Fig. 3.2b) near the moving wall ($y/h = 1$).

The minor sensitivity in $u'^+_{rms}$ and $v'^+_{rms}$ affects consequently the Reynolds stress, as a perfect collapse is shown up to $y/h \approx -0.8$, which is $y^+ \approx 25$, according[1] to Eq. 3.0.3.

Near the stationary wall, a peak in $u'^+_{rms}$ is appreciated for all the cases. This peak occurs at $y^+ \approx 12$ and it is independent from the Reynolds number, as stated in Pope [1] page 285. In addition, this peak is related to a peak of turbulent production, where the viscous stress equals the Reynolds shear stress.

Moreover, small and coherent turbulent scales are usually located near stationary walls. As stated in the Kolmogorov cascade (See Section 1.1), small scales in the inertial and dissipation ranges are considered universal, as defined in Figure 1.2. As a consequence,

[1]Since the reference is the stationary wall, the value employed in Equation 3.0.3 is $y/h = 0.2$

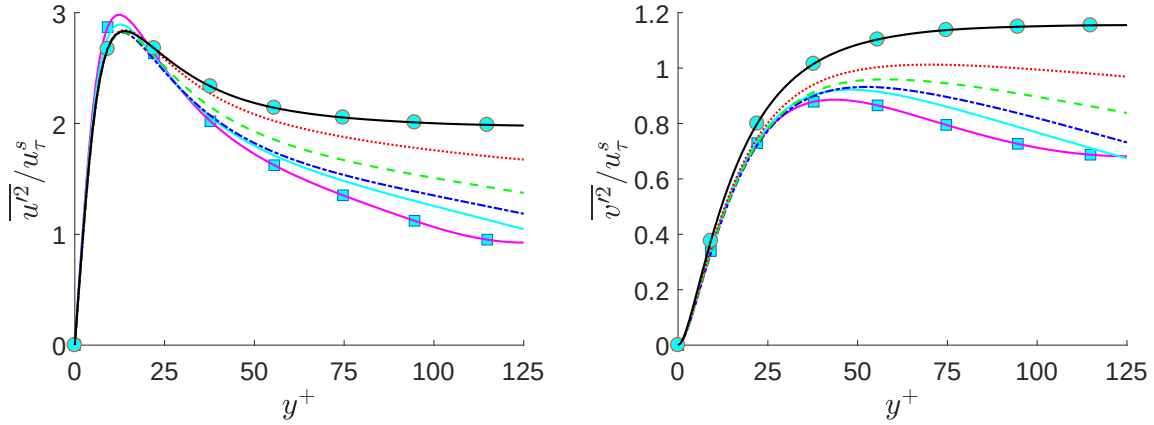


(a) (b)

Figure 3.1: Lines as in Table 3.1. (a) Root-mean-square of velocity fluctuation $u'$. (b) Root-mean-square of velocity fluctuation $v'$. Both are scaled with the shear velocity at the stationary wall, $u_\tau^s$.

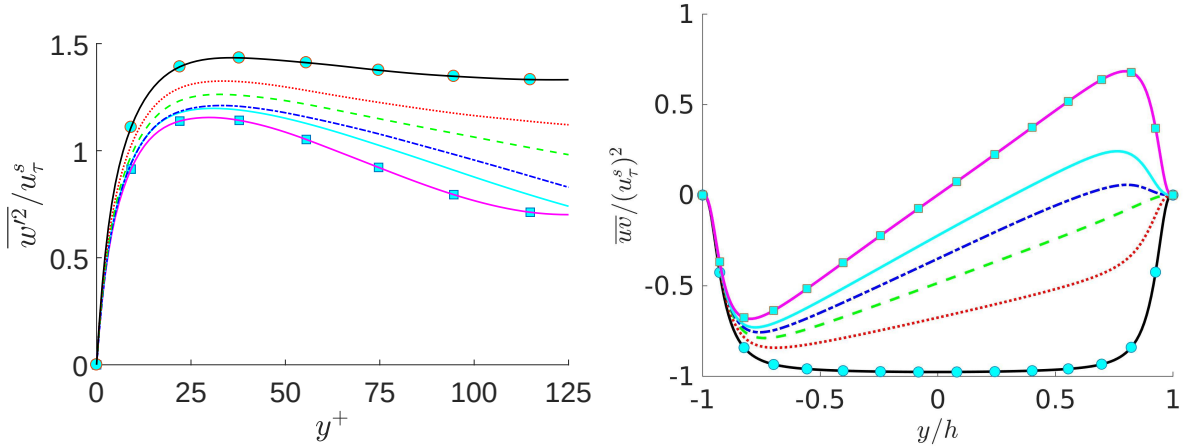


(a) (b)

Figure 3.2: Lines as in Table 3.1. (a) Root-mean-square of velocity fluctuation, $w'$. (b) Root-mean-square of Reynolds stress, $\overline{uv}$. Both are scaled with the shear velocity at the stationary wall, $u_\tau^s$.

turbulent intensities at low $y^+$ are likely to be independent from the case, but not from the Reynolds number [14].

At channel center, the velocity fluctuations in C-flow are higher than those in P-flow, mainly due to the non-zero Reynolds stress. This fact is linked to turbulence production in the center of the domain [20], see Figure 3.2b.

Regarding the distribution of $\overline{uv}^+$, it has a relevant role in the stability of the largest coherent structures in the channel center. As stated in Gandia-Barbera et al. [23], these coherent structures are present as long as the arithmetical sign of $\overline{uv}^+$ remains constant along the Y-axis. That is, approximately from case C06P04 to pure Poiseuille they are no longer present. This idea will be further explained in the coherent velocity structures

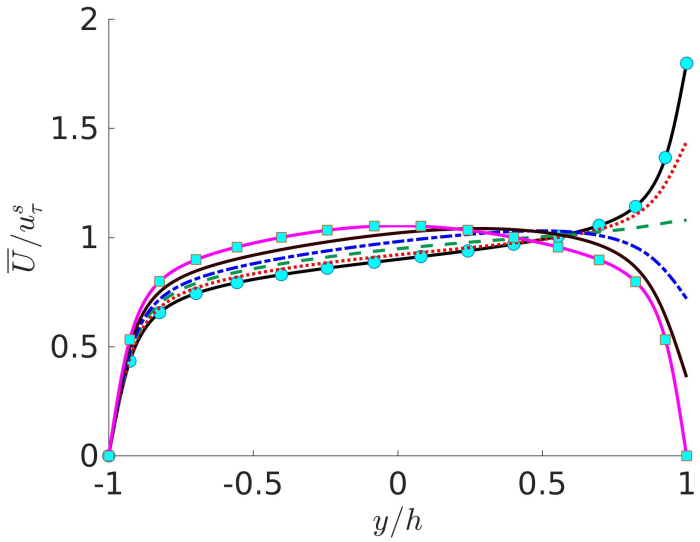


Figure 3.3: Lines as in Table 3.1. Mean velocity $\overline{U}$ for each case. No wall units are used.

chapter; that is Chapter 5.

Case C06P04 presents another characteristic, which is its low Reynolds shear stress near the moving wall. This characteristic was also appreciated in Pirozzoli et al. [3], because their paper analyses a stepped Couette-Poiseuille transition too. The authors state that the main effect of reducing the mean shear at the moving wall is the suppression of the turbulence production term in its vicinity. In this case, near-wall turbulence is dominated by the transport of kinetic energy from the channel core.

Additionally, this fact reduces drastically the friction Reynolds number at this position ($Re_\tau^m$) as stated in Table 3.1. We will see later its effects on the vortex distribution, and on the streamwise fields in Section 5.1 and Section 5.2.

Finally, just further comment that the distributions depicted in Figures 3.1 and 3.2 follow the same trend as in Pirozzoli et al. [3] despite we employ a slightly lower $Re_\tau$. Moreover, in C-flow case it gives similar results as Tsukahara et al. [20], which employed almost the same $Re_\tau$ as in this study. Note that Tsukahara et al. made use of a much bigger domain; however their one-point statistics agree with ours, as both domains are big enough to throw independent results. This fact was stated before.

In Figure 3.3 the averaged U velocity is depicted for each case. Here one can see how the transition takes place between the C- and P- flows. In addition, the boundary conditions employed in C- and P- flows, as commented in Section 2.2, can be also appreciated.

The shear stress along the Y-axis is easy to understand from this figure, considering Eq. 1.3.3, left. In C- flows the shear stress never reaches a null value, which is not the case in P- flows in the channel center. Also the shear stress is quite reduced at C06P04 near the moving wall, which consequently affects the shear velocity (Eq. 3.0.2) and friction Reynolds stress (Eq. 3.0.1), as commented before.

Denote that due to the initial condition that ensures a constant bulk Reynolds number and mass conservation (See Section 2.3), the area covered by each $\overline{U}$ along $y/h$ in Figure 3.3 is the same.

Finally, in Figure 3.4 the mean velocity $\overline{U}$ scaled in wall units in depicted for each case. We can see that there is a perfect collapse among cases in the viscous sublayer, which is defined at $y^+ < 5$. Then, as long as we achieve the buffer layer, defined at $5 < y^+ < 30$, and the log-law region ($y^+ > 30$, $y/h < 0.3$), the different cases tend to separate. Region intervals according to Pope [1], page 275.

This behaviour is also observed in Pirozzoli et al. [3], showing higher values for Poiseuille flow in the log-law region. Moreover, Pirozzoli et al. states that log-law constant B (See Eq. 3.1.1) depends on the type of flow. Hence, it becomes $B = 5.2$ in Poiseuille flow and $B = 4.7$ in Couette flow.

$$\overline{U}^+ = \frac{1}{\kappa} \log\left(y^+\right) + B \tag{3.1.1}$$

where $\kappa$ (Von Kármán Constant) and $B$ are constants. Pope [1] defines this constants as $\kappa = 0.41$ and $B = 5.2$ in a fully developed DNS channel. However, Kraheberger et al. [16] could see that these values change drastically when wall transpiration is present.

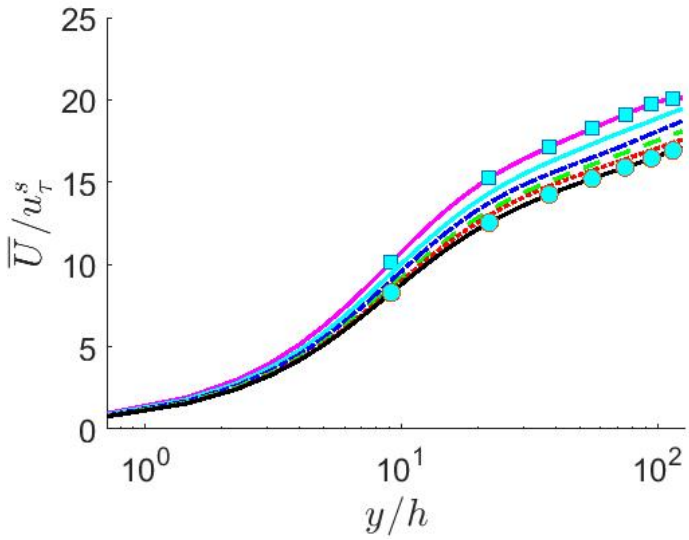


Figure 3.4: Mean velocity profiles near the stationary wall scaled in wall units. Lines as in Table 3.1.

In another interesting paper, M. Lee and Moser [8] get a perfect collapse for Couette flows at diverse $Re_\tau$ from 93 to 550, which covers our case. Nevertheless, the authors conclude that at this Reynolds numbers, Couette flows do not produce a convincing log layer. In addition, they state that in Poiseuille flow, an unambiguous log layer does not appear until $Re_\tau \approx 5000$. They can make these asseverations by observing the value of the log-layer diagnostic $\beta = y^+\langle \partial u^+/\partial y^+ \rangle$ in the log-law region. This value must stay constant around $1/\kappa = 2.604$. However, it neither achieves this values nor stays constant at their Reynolds numbers.

As a consequence, we conclude that there is no proper log layer in our simulations.

# Chapter 4

# Mathematical tools for post-processing

After the simulations were carried out according to the numerical scheme explained in Chapter 2, the results must be post-processed in order to extract relevant conclusions. Therefore, different post-processing tools were developed in Matlab. In this chapter, the tools are presented and an explanation about each one is given. However, Matlab code will not be written here, as this document is merely focused on the tools algorithm and background theory.

## 4.1 Velocity fields and derivatives extraction

The results from the simulations are stored in files with extension .h5. This extension corresponds to a HDF5 file[1], which is a file format for storing and managing extremely large and/or complex data collections, as in our case. The advantages of this extension are the following:

- Complex and heterogeneous data objects can be stored independently of their size.
- Storage allows a wide variety of datatypes, which can vary from each data object.
- High speed raw data acquisition.
- It requires no outside information for applications to interpret the structure and contents of the file.
- It runs on a wide range of computational platforms and programming languages.

Each simulation file contains a header with relevant information about the simulation, as well as the simulation results for $\phi$ and $\omega_y$. This content is expounded in Table 4.1. See that in Matlab each dataset must be specified as a full pathname with a leading '/'. For example, '/Re' for $Re_b$.

[1]More information on https://www.hdfgroup.org/

| Dataset | Definition |
|---|---|
| alp | Wavenumber inverse in streamwise direction |
| bet | Wavenumber inverse in spanwise direction |
| fmap | Technical function employed in the wall normal derivative |
| mx | Number of points in streamwise direction, referred as $N_x$ |
| my | Number of points in wall normal direction, referred as $N_y$ |
| mz | Number of points in spanwise direction, referred as $N_z$ |
| nummpi | Number of MPI processes, in which the code was executed |
| phi | Value of $\phi$ in each domain point |
| Re | Bulk Reynolds number, $Re_b$ |
| time | Simulation time at which the results were recorded |
| u00 | Mean speed in streamwise direction |
| vcon | Initial wall normal velocity |
| vor | Value of $\omega_y$ in each domain point |
| w00 | Mean speed in spanwise direction |
| y | Distribution of the points along the wall normal direction |

Table 4.1: Datasets included in each H5 simulation file.

The process followed for extracting the velocity fields and their derivatives from the simulation results is depicted in Figure 4.1.

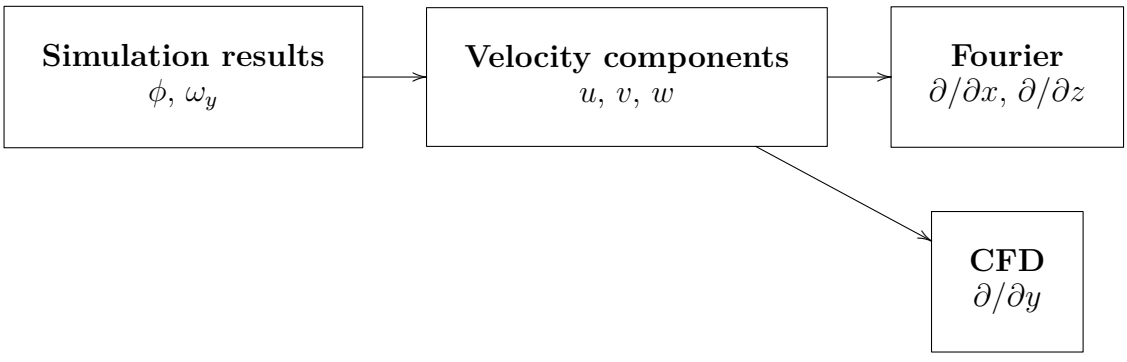


Figure 4.1: Transformation steps for extracting the velocity fields and their derivatives.

Simulation results for $\phi$ and $\omega_y$ are collected in a 3D matrix, whose rows, columns and third dimension are the wall-normal, spanwise and streamwise directions of the channel, respectively. Further, take into account that the results stored are in Fourier domain; this allows us to calculate the derivatives in an easier way, as for a given function $f(x)$

in Fourier domain, it is derived as in Eq. 4.1.2.

$$f(x) = \sum_k \widehat{f}_k \cdot e^{ikx} \tag{4.1.1}$$

$$f'(x) = \sum_k ik \cdot \widehat{f}_k \cdot e^{ikx} \tag{4.1.2}$$

where $k$ represents the wave-number. Hence, in Fourier domain the derivative of a given function is calculated by multiplying its wave-number and the imaginary unit, $i = \sqrt{-1}$.

In regard to our study, the streamwise and spanwise directions have different wave-number arrays to derive from X and Z. These are described in Eq. 4.1.3 and 4.1.4, respectively. Additionally, their distribution is dissimilar. Both arrays were arranged taking into consideration the way the results of the simulations are stored, as well as Fourier transformation preferences in Matlab.

$$xalp = i \cdot \alpha \cdot \left[0 : \frac{mx}{2} - 1\right] \tag{4.1.3}$$

$$xbet = i \cdot \beta \cdot \left[0 : \frac{mz-1}{2},\ \frac{1-mz}{2} : -1\right] \tag{4.1.4}$$

The initial definition of variable $k$ covers the interval $[0,\ 2\pi)$, but in both directions the length is larger than $2\pi$. Therefore, the constants $\alpha$ and $\beta$ are chosen in order to expand this interval; now variable $k$ covers from 0 to $2\pi/\alpha$ or $2\pi/\beta$, respectively. After this explanation, one can understand that the definition of these constants arise from,

$$[\alpha,\ \beta] = \left[\frac{2\pi}{L_x},\ \frac{2\pi}{L_z}\right] \tag{4.1.5}$$

being $L_x$ and $L_z$, the channel length and width, respectively.

In order to extract the velocity fields $(u, v, w)$ from the results $(\phi, \omega_y)$, the procedure solves first Equation 2.1.19. Expanding that equation, we obtain:

$$\frac{\partial^2 v}{\partial x^2} + \frac{\partial^2 v}{\partial y^2} + \frac{\partial^2 v}{\partial z^2} = \phi \tag{4.1.6}$$

Now, the derivative in Fourier domain is applied. Notice that the second derivative is obtained through the derivation of the Eq. 4.1.2:

$$f''(x) = -\sum_k k^2 \cdot \widehat{f}_k \cdot e^{ikx} \tag{4.1.7}$$

from now $k_x^2$ and $k_z^2$ will be referred as $alp_2$ and $bet_2$, respectively; according to the nomenclature in the Matlab script.

Consequently, Eq. 4.1.6 is written as:

$$-xalp^2 \cdot v + \frac{\partial^2 v}{\partial y^2} - xbet^2 \cdot v = \phi \tag{4.1.8}$$

Derivation in wall-normal direction is not straightforward. As stated in the introduction to the Chapter 3, the spacing along the Y direction is not constant. This feature makes necessary to use another derivation scheme in this direction. Concretely, the method utilized is based on seven-point compact finite differences, with fourth-order consistency and extended spectral-like resolution [18]. Its error is of the order $\mathcal{O}(h^{10})$.

In accordance with this method, second-order derivatives are expressed as:

$$B_2 \cdot \frac{\partial^2 v}{\partial y^2} = A_2 \cdot v \tag{4.1.9}$$

where $A_2$ and $B_2$ are $N_y \times N_y$ sparse matrices. These matrices where computed using the methods developed in the last year project of Alfonso Pallarés. In this case, $N_y = 151$.

With this definition, Eq. 4.1.8 is expressed as:

$$B_2^{-1} \cdot A_2 \cdot v - (alp_2 + bet_2) \cdot v = \phi \tag{4.1.10}$$

So, the last step is to extract $v$ from the equation.

$$(A_2 - B_2 \cdot (alp_2 + bet_2)) \cdot v = B_2 \cdot \phi \tag{4.1.11}$$

Note that Eq. 4.1.11 is a matrix equation. Curiously enough, the matrix that multiplies $v$ on the left-side of the equation is a pentadiagonal matrix. This allows us to employ a specific Matlab user-function called *pentsolve* to solve this system, which reduces significantly the calculation time.

However, the results of $\phi$ as well as $\omega_y$ are complex, so the real parts are collected in the odd positions along the rows, and the imaginary parts are collected in the even positions. That is, for a given wall-parallel plane along the domain:

$$\begin{aligned} \omega_y &= vor(1:2:end,:) + i \cdot vor(2:2:end,:) \\ \phi &= phi(1:2:end,:) + i \cdot phi(2:2:end,:) \end{aligned} \tag{4.1.12}$$

This fact is the reason why the resolution of the Eq. 4.1.11 is carried out twice in the Matlab nested function *Lapvdv* inside the script *eddysimplified*.

In order to extract the remaining velocity fields, we still need the first derivative $\partial v/\partial y$, which is described by the compact finite differences method [18] as:

$$A_1 \cdot \frac{\partial v}{\partial y} = B_1 \cdot v \tag{4.1.13}$$

See that when employing the expression in Eq. 4.1.13 in Matlab for deriving, the right side is multiplied by a one-dimensional column called $fmap$. Its purpose is to map the derivative from an equispaced grid to a non-uniform grid, as it is the case in wall-normal direction. This increases the precision of this first derivative.

The streamwise and spanwise velocity field are calculated from the equations system conformed by Eq. 2.1.20 and Eq. 2.1.21. For the $u$ field, Eq. 2.1.20 is derived by $x$ on

its both sides, and Eq. 2.1.21 is derived by $z$ on its both sides. Then, both resulting equations are summed, giving Eq. 4.1.14 as a result.

$$\frac{\partial^2 u}{\partial x^2} + \frac{\partial^2 u}{\partial z^2} = \frac{\partial \omega_y}{\partial z} - \frac{\partial^2 v}{\partial x \partial y} \tag{4.1.14}$$

In a similar way, for extracting $w$ field Eq. 4.1.15 is obtained by deriving Eq. 2.1.20 by $z$, and Eq. 2.1.21 by $x$, on its both sides. Then, second equation is subtracted from the first one.

$$\frac{\partial^2 w}{\partial x^2} + \frac{\partial^2 w}{\partial z^2} = -\frac{\partial \omega_y}{\partial x} - \frac{\partial^2 v}{\partial y \partial z} \tag{4.1.15}$$

The last step on both equations is to apply the Fourier derivation, for obtaining $u$ and $w$, respectively. Thus, Eq. 4.1.14 and 4.1.15 are written the following way in Matlab.

$$\begin{aligned} (alp_2 + bet_2) \cdot u &= \omega_y \cdot xbet - \frac{\partial v}{\partial y} \cdot xalp \\ (alp_2 + bet_2) \cdot w &= -\omega_y \cdot xalp - \frac{\partial v}{\partial y} \cdot xbet \end{aligned} \tag{4.1.16}$$

where $\frac{\partial v}{\partial y}$ was previously computed from Eq. 4.1.13 in function *Lapvdv*.

The last step for completing the velocity fields is adding their mean values at each wall-normal position. Spanwise and wall-normal velocity fields have no mean values due to the description of the studied cases, but the streamwise velocity field has. In order to add these values, which are stored as $u00$ (See Table 4.1), they are written in the first column of the estimated $u$ field, Eq. 4.1.16. So, in Matlab we see:

$$\begin{aligned} uc\,(:,\,1,\,1) &= u_{00} \\ vc\,(:,\,1,\,1) &= 0 \\ wc\,(:,\,1,\,1) &= 0 \end{aligned} \tag{4.1.17}$$

Once each velocity field is computed, we have to derive each one from each spatial dimension; that is, $x$, $y$ and $z$. So, each field develops three different derivatives of the same size as the original field. We do this because they will be further needed for the vortex identification method, which is later explained in Section 4.2.

Derivations are carried out in a Matlab function called *physDer*, in which the inputs are, among others, the extracted velocity fields in Fourier domain; and its output is a Matlab structure containing these velocity fields and their derivatives in the physical domain. The method for deriving in Fourier domain is already explained, so now the transformation from Fourier to Physical is described.

The steps are:

1. Permute the 3D matrix in Fourier domain, so its new dimensions are the third, second and first dimensions of the initial matrix. Check for correctness that the size of the resulting matrix is $mx/2 \times mz \times my$.

2. Making use of a for-loop along the third dimension $[1 : my]$, select each 2D plane and apply the inverse Fourier transform along each row.

3. Rearrange the 2D matrix distribution along the columns. This step is done to create a conjugate symmetry in this direction, so the inverse transform computation in Matlab is faster and the output is real.[2]. The distribution employed is:

$$[u(:,\, k,\, j);\, 0;\, transpose(u(end : -1 : 2,\, k,\, j)')] \tag{4.1.18}$$

   Take into account that for complex numbers, the function *transpose* calculates their conjugate, and then transposes.

4. Apply the inverse Fourier transform along each column of the 2D matrix. Then, select the following 2D matrix employing the For-loop.

5. Once left the For-loop, multiply the resulting 3D matrix by a factor, which arises from the definition of the Fourier transformation. This factor is $mx \cdot (mz + 1)$.

This factor is not applied for calculating the inverse Fourier transform of the mean velocity fields and derivatives. Mean velocity fields are estimated as the mean of all instantaneous fields in physic domain, and later, transformed to Fourier in order to calculate its derivatives. In this process, no factor is used, so in the inverse neither.

## 4.2 Vortex identification method

The analysis of the large turbulent structures in Couette flows will be carried out first by observing and measuring the velocity distribution along the channel, and second by analysing the vortex distribution in the domain. The reason for studying the vortex distribution is to find patterns related to each kind of coherent structure, which are mainly low and high velocity structures.

This approach is already employed in other studies. C. Prus [24] carried out vortex identification in turbulent duct flows of different aspect ratios. Additionally, in this study diverse identification methods were compared. In another interesting paper, Chakraborty et al. [25] stated a relationship between diverse identification schemes based on a threshold relationship. Nevertheless, Alamo et al. [26] reported the defect of considering a constant threshold in wall-bounded turbulence, owing to the inhomogeneity of the flow in the wall-normal direction. This fact complicates the comparison of data from different wall distances when a uniform threshold is used. When the threshold is chosen to visualize properly the vortices of the near-wall layer of the present channels, very few of them are observed in the outer region. Conversely, when the threshold is lowered to visualize the vortices of the outer layer, the near-wall region becomes confusingly cluttered with vortex tubes. This behaviour is proven to worsen with increasing Reynolds number.

According to the information about our study, very large vortex clusters are found in the centre of the channel, which makes necessary a variable threshold.

[2]For more information, read Matlab Documentation for the inverse Fourier transformation function, *ifft*.

Following the steps employed in Alamo et al. [26], in this study we selected the identification method developed by Chong et al. [27] for vortex identification, with a non-uniform threshold along the wall-normal direction. This approach is also shared by C. Prus [24]. For more information about other identification methods, we refer the reader to Chakraborty et al. [25].

The Chong method, sometimes referred as $\Delta$ criterion, is based on a local analysis of the velocity gradient tensor, $\nabla\vec{u}$, defined in Eq. 4.2.1. Here are used the derivatives determined in Section 4.1.

$$\nabla\vec{u} = \begin{pmatrix} U_x & U_y & U_z \\ V_x & V_y & V_z \\ W_x & W_y & W_z \end{pmatrix} \tag{4.2.1}$$

where $U_x = \partial u/\partial x$, $V_y = \partial v/\partial y$, and so on.

According to this method, a vortex region is a domain, where $\nabla\vec{u}$ has complex eigenvalues. Considering a non-rotating reference frame translating with a fluid particle, the instantaneous streamline pattern, which can be obtained from Taylor series expansion of the local velocity to a linear order, is governed by the eigenvalues of $\nabla\vec{u}$.

If two of the eigenvalues form a complex conjugate pair (for both compressible and incompressible flows), these streamlines are closed or spiralling. Note that in an unsteady flow, the usage of instantaneous streamlines implies assuming the velocity field to be frozen at that instant in time [25].

The equation for the eigenvalues of $\nabla\vec{u}$ is written as:

$$\lambda^3 + P\lambda^2 + Q\lambda + R = 0 \tag{4.2.2}$$

where $P$, $Q$ and $R$ are the three invariants of $\nabla\vec{u}$, defined as $P = -\nabla\cdot\vec{u}$ (first invariant[3]), $Q$ (second invariant, defined in Eq. 4.2.3) and $R = -\operatorname{Det}(\nabla\vec{u})$.

$$Q = -\frac{1}{2}\operatorname{Tr}\left(S^2 + \Omega^2\right) \tag{4.2.3}$$

where $S = \frac{1}{2}\left(\nabla\vec{u} + (\nabla\vec{u})^t\right)$ and $\Omega = \frac{1}{2}\left(\nabla\vec{u} - (\nabla\vec{u})^t\right)$ are the symmetric and antisymmetric components of $\nabla\vec{u}$, respectively. For clarity, the superscript $t$ means transposed, and $\operatorname{Tr}()$ is the trace function.

The discriminant for Eq. 4.2.2 is (for incompressible case, $P = 0$):

$$\Delta = \left(\frac{R}{2}\right)^2 + \left(\frac{Q}{3}\right)^3 \tag{4.2.4}$$

Considering a given threshold, which in our case will depend on the position in the wall-normal direction, the condition $\Delta$ is greater than the threshold implies that this point is located in a vortex core. That is why this method is also called $\Delta$ criterion.

[3]Another way to write the first invariant is $P = -div(\vec{u}) = -\left(\frac{\partial u}{\partial x} + \frac{\partial v}{\partial y} + \frac{\partial w}{\partial z}\right)$.

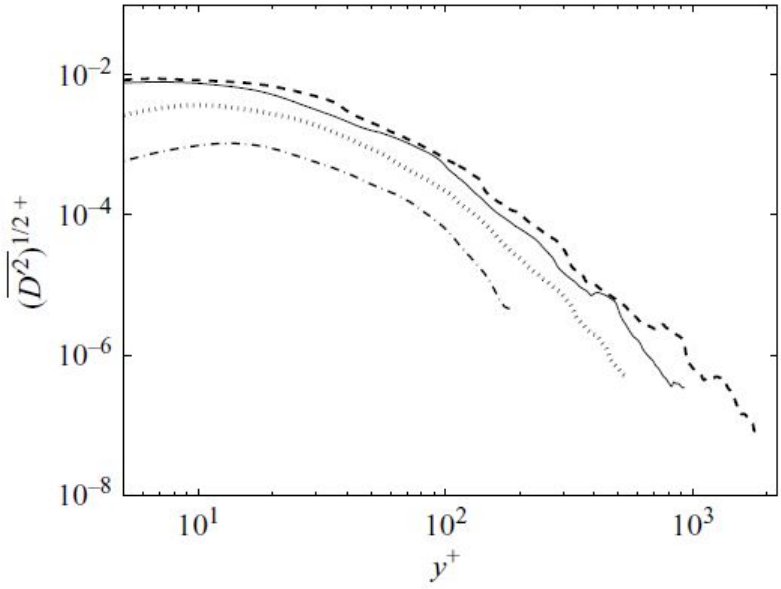


Figure 4.2: Standard deviation of $\Delta$ in wall-parallel planes along $y^+$. Lines in [26].

According to Del Alamo et al. [26], the threshold proposed should vary with wall distance as $\overline{(\Delta'^2)}^{1/2}$; that is, the standard deviation of $\Delta$ over wall-parallel planes. This approach would be enough to reduce the vortex identification difficulties in wall-bounded flows, which were partially described at the beginning of this section. The distribution of the standard deviation of $\Delta$ over wall-parallel planes is depicted in Figure 4.2, extracted from Del Alamo et al. [26]. Here, we can see that its value is higher near the walls than in the channels center. This means that the criterion is more restrictive with near-wall vorticity. Different lines describe increasing $Re_\tau$, as one can notice due to the increasing length in $y^+$ by taking into account Eq. 3.0.3.

Following this idea, we consider that a point $\vec{x}$ belongs to a vortex core if

$$\Delta(\vec{x}) > \alpha \cdot \overline{(\Delta'^2)}^{1/2} \tag{4.2.5}$$

where $\alpha$ is the percolation limit, which has a constant value for a given case.

The purpose of the percolation limit is to select the threshold, which would not collect all vortex cluster points into a big vortex cluster neither would consider many scattered vortex clusters. Both cases would be troublesome for vortex identification. Hence, for selecting the appropriate percolation limit $\alpha$, the following approach is carried out by C. Prus [24] and Del Alamo et al. [26].

To perform the percolation analysis, we first identify the vortex points of a given simulation through Chong method. Note that Chong method makes use of the threshold in Eq. 4.2.5, where $\alpha$ is still an unknown factor. Hence, several identification will be carried out with different values of $\alpha$ inside a given range. Take into account that computational time can increase considerably if many values for $\alpha$ are used.

The result of each identification is a 3D matrix of size $N_x \times N_z \times N_y$, in which the only possible values are 0 and 1. This matrix will be further referred as Chong matrix. If a given point $\vec{x} = (x, z, y)$ accomplishes the condition in Eq. 4.2.5, the identification

matrix has a 1 in the position of that point. Otherwise, it is a 0.

Bearing these facts in mind, we store all the identifications matrices in one by adding them up. As a result, there is only one 3D matrix of size $N_x \times N_z \times N_y$, in which the values go from 0 to the number of identifications carried out. The latter is the same as the amount of values for $\alpha$.

Additionally, since matrix values are limited integers, we can store the Chong matrix efficiently employing *int*8 or *uint*8. This way its size is eight times smaller than storing the matrix as *double*, what Matlab do automatically; i.e. according to the number of points in each direction of the domain (See Table 3.1), only one identification matrix stored as *double* occupies 236.88 MB, which is reduced to 29.61 MB if stored as *int8*.

Secondly, gather the vortex points that are adjacent in any direction. In such manner we can define the vortex clusters present in the domain. For this step, we have developed specific tools for 2D and 3D vortex clusters. Both will be explained in detail in Section 4.4 and Section 4.5, respectively.

In order to determine the optimal value of the percolation limit, Del Alamo et al. [26] recommends to calculate the division between the volume of the biggest cluster encountered $V_{max}$, and the overall volume $V$ occupied by all the clusters; that is, $V_{max}/V$, for each identification made with a given value of $\alpha$. A 3-dimensional cluster is defined by connecting the points satisfying the criterion in Eq. 4.2.5. Connectivity is checked on each point along 26 directions employing unitary vectors.

In other words, if we have a 3-dimensional point $(x_0,\, z_0,\, y_0\,)$, we have $3^3 - 1$ possible connections, considering that there are 3 dimensions and 3 possible directions, which are $0$, $-1$ and $+1$. See that direction $(0,\, 0,\, 0\,)$ is not employed, because it aims to the initial point itself, so it is subtracted.

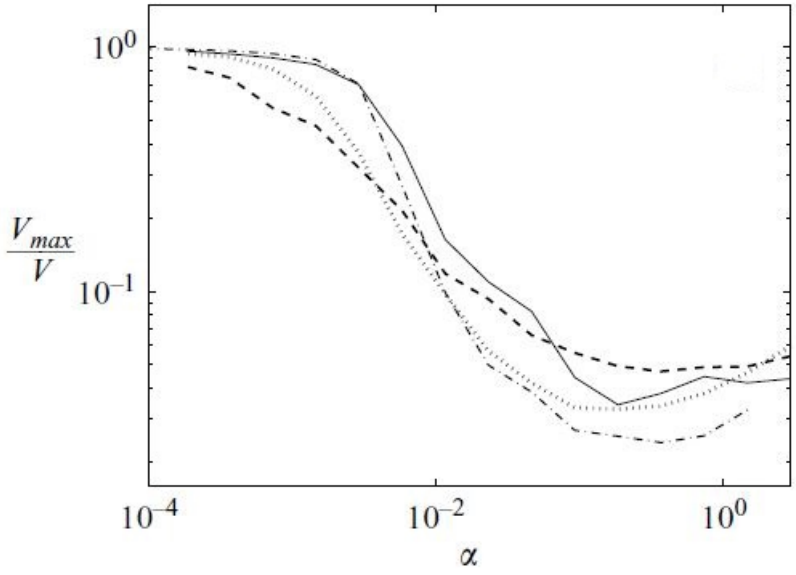


Figure 4.3: Volume $V_{max}$ of the largest cluster normalized with the overall volume $V$ occupied by all the clusters, represented as a function of the threshold $\alpha$.

Figure 4.3 shows the behaviour of $V_{max}/V$ along the percolation limit. For $\alpha \approx 1$, few

small vortex points are identified; so, we expect this relation to have a value near 0. As soon as $\alpha$ decreases, new vortex points appear while others coalesce, and the variation of $V_{max}/V$ with $\alpha$ is the result of the trade-off between the two processes.

Figure 4.3 also exhibits that both processes are balanced above $\alpha \approx 10^{-2}$, so that $V_{max}/V$ remains roughly constant while the number of clusters increases. See that vertical axis is logarithmic. Below this value of the percolation limit, few new clusters are identified and the existing ones merge until only a single, large vortex cluster remains, yielding $V_{max}/V \approx 1$. Finally, see that all lines tend to collapse; this means that the evolution of $V_{max}/V$ is independent from the friction Reynolds number $Re_\tau$.

Taking into account that the percolation limit must ensure that vortex clusters are neither excessively merged nor too scattered, Del Alamo et al. [26] defines this limit where the slope of $V_{max}/V$ is maximum. In Figure 4.3, this value is at $\alpha \approx 0.008$. This criteria is also adopted by C. Prus [24].

Nevertheless, Del Alamo et al. [26] selects as percolation limit the latter value multiplied by 2.5, because the computational time needed by their clustering algorithm diminish significantly, and the volume coefficient remains roughly constant.

In our study, the percolation limit must be calculated for each Couette-Poiseuille case, including the pure ones. Results are published in Section 6.1. Moreover, since we have several instantaneous simulations of each case, the corresponding $\alpha$ to each case will be estimated as the mean of all the instantaneous percolation limits.

## 4.3 Vortex clusters determination

In this section the algorithms for vortex clusters determination in 2D and 3D will be explained. These algorithms take as an input the Chong matrix, in which the only possible values are 0 or 1. Then, they gather vortex points that connect each other, creating a vortex cluster with all the connected points.

The algorithm for 2D clusters determination is a Matlab function called *analizasparse*. The inputs of this function are:

- **matriz_chong**: Identification matrix calculated through Chong method, where the only possible values are 0 and 1. Size: $N_x \times N_z \times N_y$.
- **n**: position of the XZ plane in matriz_chong, where the cluster determination will be carried out. The range of this value is from 1 to $N_y$. Size: $1 \times 1$.

On the other hand, the output of this function is:

- **vortex**: Matlab structure with an only field called *nodes*. Each field position contains the points corresponding to a certain vortex cluster. The size of this structure goes from 1 to the number of identified vortex clusters. Moreover, each field position has a variable size. For calling the $i$-th field position of this structure in Matlab, we make use of the command *vortex(i).nodes*

The algorithm employed in *analizasparse* is detailed in Algorithm 1.

**Algorithm 1:** 2D vortex cluster identification

```
1  Create a variable called A, which contains the XZ plane to analyse;
2  Mirror this plane in another variable called wk, whose content will be later
     modified;
3  Define a matrix with all the possible directions to search, from a given A matrix
     point, when conforming a vortex cluster. These directions are explained in
     Figure 4.4;
4  for i = 1 to N_X do
5      for k = 1 to N_Z do
6          if wk(i, k) = 0 then
7              Jump to the next step in the For loop;
               /* This condition means that this point has no vortex.   */
           /* Start the identification of a cluster of index ind       */
8          Create a queue where all the points that could pertain to this cluster will
             be gathered ;
           /* These points can be repeated, so this is not a result.   */
9          Write the identified (i, k)-point on the first position of the queue;
10         Number of identified points on this vortex cluster set to 1;
                                                          /* Variable np */
11         Position of point in queue being treated set to 1;
                                                          /* Variable nq */
12         Size of the queue set to 1;
                                                          /* Variable sq */
13         while nq ≤ sq and Point treated is not zero do
14             if nq = 581 then
15                 Remove all the values in the queue from position 1 to 580;
16             if wk(i, k) = 0 then
17                 This point was already saved in function output, so it is deleted
                     from the queue. The way we delete a point in queue is by setting
                     it to (0, 0);
18                 nq = nq + 1;
19                 Jump to the next step in the For loop;
20             Save the current point in the function output;
21             Set wk(i, k) = 0;  /* Hence, if this point is written again in
                 the queue, it will be automatically deleted.  */
22             for Each possible direction to look for connected points do
23                 Load the coordinates of the first point in a given direction;
24                 while Loaded coordinates give wk = 1 do
25                     Add the point coordinates to the queue;
26                     sq = sq + 1;
27                     Load the coordinates of the next point following the same
                         direction;
28             Set to 0 the coordinates of the initial point treated nq in the queue;
29             nq = nq + 1;
30         If are still present, remove remaining zero values in function output;
               /* These zeros were created due to preallocation of cluster
           points.  */
31         ind = ind + 1;
           /* Starts with the next vortex cluster.                     */
```

As a single field is around 1.8 GB, it is necessary to optimise the codes as much as possible. Take into account that in Matlab removing a row from a matrix is a computationally expensive task. If every time an analysed point is removed from the queue, the algorithm would be poorly optimized. Consequently, queue positions are removed after a given number of points is checked. This value is of course arbitrary, and can be modified if it is required. Remember that the queue stores identified vortex points, that may conform the cluster being analysed.

By avoiding this step, so no position would be removed, the queue could become so large, that performing operations with it would be also inefficient. Hence, it is necessary to remove queue positions after a given amount of treated points.

On the other hand, in order to identify a treated point in the queue, its coordinates are basically changed to 0. Since Matlab does not accept (0, 0) as a matrix location, we ensure that this is no longer a matrix point.

Regarding the searching direction depicted in Figure 4.4, matrix *dirs* has altogether 8 pointing directions, because (0, 0) is not a direction. In this part of the algorithm, every pointing direction is selected and starts from the initial treated point. If the next point in a given direction, i.e. (0, 1), has a value 1, then it is stored in the queue, and the next point in this direction is checked. Once the checked point has a value 0, stops counting, and the next direction in matrix *dirs* is selected, i.e. (0, −1). Again, this new direction starts from the initial treated point.

Finally, each time the algorithm starts with a new vortex cluster, an array of zeros is created in the Matlab structure position *ind*, which will store this vortex cluster points. If after finishing the identification, some of this zeros still remain, Algorithm 1 removes them in Line 30. This preallocation improves the algorithm if a large vortex is identified.

Remember from Section 2.2 that in wall parallel directions there is periodicity. This fact must be taken into account when following a pointing direction. If searching starts from a point on a domain limit or while following a pointing direction a limit is reached, the algorithm must continue on the beginning of that direction. For instance, if the right wall of the domain is reached, the next point will be located on the left wall. This condition is invoked in streamwise and spanwise indices, which are defined as:

$$\begin{aligned} indx &= [1:N_X,\ 1:N_X,\ 1:N_X] \\ indz &= [1:N_Z,\ \ 1:N_Z,\ 1:N_Z\,] \end{aligned} \tag{4.3.1}$$

Searching directions are always added to the second $1 : N_i$ present in *indx* and *indz*. As a result, at point (*indx*, *indz*) = (1, 1) if direction $(-1, -1)$ is employed, we get (*indx*, *indz*) = ($N_X$, $N_Z$). Following this idea, at point (*indx*, *indz*) = ($N_X$, $N_Z$) if direction $(1, 1)$ is employed, we get (*indx*, *indz*) = (1, 1).

Once explained the algorithm for 2D vortex cluster identification, algorithm for 3D vortex clusters has minor changes from Algorithm 1.

Despite the output is the same as in Algorithm 1, inputs are slightly different.

- **matriz_chong**: Identification matrix calculated through Chong method, where the only possible values are 0 and 1. Size: $N_x \times N_z \times N_y$.

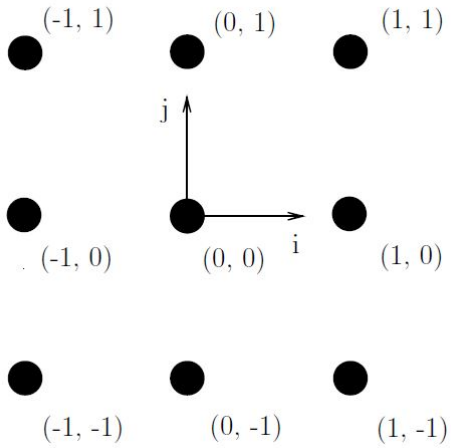


Figure 4.4: All possible directions for connecting points during vortex cluster identification. These directions are stored in matrix *dirs*

- **n_ini**: position of the XZ plane in matriz_chong, from where the cluster determination starts. The range of this value is from 1 to $N_y$. Size: $1 \times 1$.
- **n_fin**: position of the XZ plane in matriz_chong, where the cluster determination ends. The range of this value is from 1 to $N_y$. Size: $1 \times 1$.

Therefore, for a complete cluster determination: $n_{ini} = 1$ and $n_{fin} = N_y$.

Regarding the searching directions, in 3D there are altogether 26 directions. Considering that we have 3 dimensions and 3 possible values at each dimension, i.e. -1, 0 and 1, the number of combinations is $3^3 - 1$. One combination is subtracted because (0, 0, 0) is not a possible direction. As one can imagine, this fact makes the algorithm more computationally demanding in comparison with the 2D algorithm.

In the 3D algorithm the new dimension advance in wall-normal direction. As stated in Section 2.2, wall-normal direction has no periodicity. So, this must be specified when following a given searching direction. In the algorithm we define the indexes in Y as:

$$indy = [-1,\ 1 : ny,\ -1] \tag{4.3.2}$$

which means that if the algorithm tries to cross a wall along the Y direction, the variable *indy* becomes -1. This is clearly not a wall-normal coordinate for a point in Matlab. In addition, While loop present in Algorithm 1 on Line 24, has an additional condition: the third coordinate of a point cannot be -1. If so, stop in that direction and load the next searching direction.

For example, if at point (56, 120, $N_Y$), algorithm follows the direction (1, 0, 1), the resulting point would be (57, 120, $-1$). This result would make the algorithm leave the While-loop, and select the next direction; i.e. (1, 1, 0).

Finally, removal of queue positions is carried out after 98000 points are analysed. As in this algorithm a longer queue is expected, it is optimal to do this step after a larger amount of points is treated in comparison with the 2D algorithm.

## 4.4 Areas of 2D vortex clusters

A useful way of extracting information of the identified vortex clusters is to calculate their area or volume, depending on how many dimensions it has. Our first step will be to develop an algorithm able to calculate the area of 2D vortex clusters. As one can imagine, this is a necessary step in order to develop later an algorithm to calculate the volume of each 3D vortex cluster. The importance of their volume stems from the percolation analysis described in Section 4.2. Remember that volumes are used in one step of the process for measuring the appropriate percolation limit.

The algorithm is coded in a Matlab function called *vortexvol2Doriented*. This function has as inputs:

- **vortex**: Matlab structure with an only field called *nodes*. Each field position contains a matrix with the points corresponding to a certain vortex cluster. The size of this matrix is $2 \times N_{points}$. The size of *vortex* goes from 1 to the number of identified vortex clusters.
- **hx**: constant distance between points in streamwise direction. This distance should be introduced in meters. Size of this variable: $1 \times 1$.
- **hz**: constant distance between points in spanwise direction. This distance should be introduced in meters. Size of this variable: $1 \times 1$.
- **capa**: XZ plane of matrix Chong, where vortex clusters in *vortex* were identified. Size of this variable: $N_x \times N_z$.

On the contrary, the output of this function is:

- **nv**: array with the area of each vortex cluster, preferably in $m^2$.
  Its size is $N_{clusters} \times 1$.

In a comprehensive way, the process of estimating the area of each cluster is based on considering that a cluster is conformed by many small squares of area $(hx \cdot hz)$. As expected, the area of each square is determined by how many of its points have a positive value; that is, 1 in the Chong matrix. Consequently, if a square has 4 points, whose coordinates in Chong matrix have a unitary value, this square contributes an area $(hx \cdot hz)$ to the whole cluster area. As soon as not all its points have unitary values, its contribution decreases by a given factor. This can be appreciated in Algorithm 2, and it is later explained in this section.

Each square is identified by a single cluster point, so each time a cluster point is selected, Algorithm 2 calculates the area of the square referred by this point. This idea is explained in Figure 4.5. Bear in mind that due to the number of positive points conforming the square, it can be in fact, half square, a line (straight or inclined) or a single point.

This stems from the fact that despite the selected point conforms a vortex cluster, the surrounding domain points may not be located in a vortex, so their value is 0 in Chong matrix.

**Algorithm 2:** Measure the area of a 2D vortex cluster.

**Function** `vortexvol2Doriented`:
**Data:** vortex, hx, hz, capa
**Result:** nv

**if** *vortex is not an structure* **then**
    Create a one-field structure with input *vortex*;

Preallocation of output *nv* and variable *areas*;
`/* Variable areas collects all the contributions of the squares, which finally gives the cluster area. */`

Create indexes along streamwise and spanwise direction. Take into account periodicity boundary condition;

**for** *Each vortex clusters gathered* **do**
    Store the cluster nodes in a variable called *wk*;
    **for** *Each node in a vortex cluster* **do**
        Store in diverse variables the values that the neighbouring domain points have in Chong matrix. These variables are N, S, E, and so on;
        `/* This variables are later employed to check which the contribution of the selected square is to the total area. */`
        Based on the way the area contributions are defined, the variables *dots* and *surround* are created.
        **if** *dots = 3* **then**
            `/* Square is complete. */`
            $area = area + 1$;
        **else if** *dots = 2* **then**
            `/* Half square is complete. */`
            $area = area + 0.5$;
        **else if** *All neighbouring points are 0* **then**
            `/* This is a single point. */`
            $area = area + 0.125$;
        **else if** *dots = 1* **then**
            `/* This is a line. */`
            **if** *East Point is 1* ***and*** *surround = 0* **then**
                $area = area + 0.25$;
            **else if** *South Point is 1* ***and*** *West and South-West Points are 0* **then**
                $area = area + 0.25$;
            **else if** *South-East Point is 1* **then**
                $area = area + 0.25$;
        **if** *North Point is 0* ***and*** *East and North-East points are 1* **then**
            $area = area + 0.5$;
            `/* Half square on top */`
            **else if** *North and East points are 0* ***and*** *North-East point is 1* **then**
                $area = area + 0.25$;
                `/* Line inclined up. */`
        Variable *area* is multiplied by $(hx \cdot hz)$, and stored in output vector *nv*.
        Variable *area* is reset.

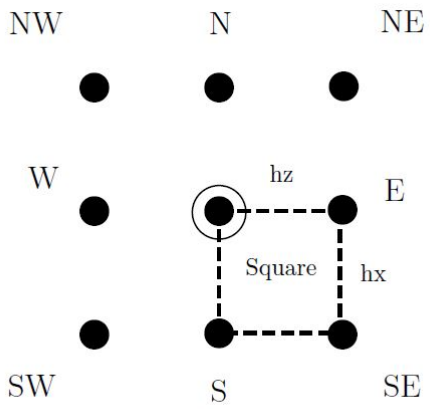


Figure 4.5: Names as used in Algorithm 2. Neighbouring points to a treated point (circled) by the algorithm. The selected point is employed to calculate the area contribution of the depicted square (dashed lines).

The contribution of each square to the whole cluster area follows the next statements. Bear in mind that selected point has always a positive value in Chong matrix, that is the reason why this point is part of a vortex cluster.

From here, the sum of the values in points E, S and SE will be referred as *dots*, as it is done in Algorithm 2. The contribution is later multiplied by $(hx \cdot hz)$ to estimate the area.

- If *dots* is equal to 3, we have a complete square, so its contribution is 1.
- If *dots* is equal to 2, we have a half square, so its contribution is 0.5.
- If *dots* is equal to 1, we have a line, so its contribution is 0.25.
- If *dots* is equal to 0, we have a single point, so its contribution is 0.125.

This approach may look easy to apply, but in fact it has some aspects to consider while gathering all contributions.

See in Figure 4.5 that once the square contribution is counted, in the next steps the algorithm will select the point E for treatment. Thus, it will become the circled one. If its corresponding E and SE points are 0, variable *dots* will still be equal to 1 due to the contribution of its corresponding S point. In short, for a given square its points E and SE can be considered later as a line according to this approach, despite this line was already considered in the square contribution.

In order to avoid this problem we can see in Algorithm 2 that if variable *dots* becomes 1, another condition must be fulfilled in order to consider a line contribution. See that this problem also concerns the horizontal bottom line of a square.

Furthermore, this approach must be modified to contemplate a half square on top or a inclined line if they are conformed by NE and E or just NE, respectively. These modifications are defined in Lines 24 and 26 in Algorithm 2.

For the sake of clarity, an example is depicted in Figure 4.6. Here we can see a vortex cluster constituted by black points. White points are domain points without a vortex. Figure 4.6 could be considered as a piece of a XZ plane belonging to a Chong matrix. See also that periodicity does no affect in this example, this was defined on purpose for simplicity.

Figure 4.6 also includes the area contributions of each domain square, which are in tune with the statements declared before.

See that the half-square contribution on the top in the middle will be calculated in algorithm Line 24, as it is an exception commented before.

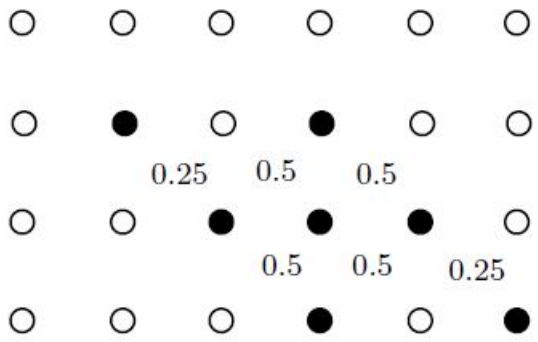


Figure 4.6: Example of a cluster area calculation. Black points are cluster points. White points are domain points without vortex. Each area contribution is depicted in its corresponding position.

In order to resolve example in Figure 4.6 in Matlab, first we define the matrix in Eq. 4.4.1.

$$chong = \begin{pmatrix} 0 & 0 & 0 & 0 & 0 & 0 \\ 0 & 1 & 0 & 1 & 0 & 0 \\ 0 & 0 & 1 & 1 & 1 & 0 \\ 0 & 0 & 0 & 1 & 0 & 1 \end{pmatrix} \tag{4.4.1}$$

Then, it is introduced in the vortex cluster identification code (Algorithm 1) as input *matriz_chong*. Additional input $n$ is 1.

Finally, output *vortex* is introduced in areas calculation code (Algorithm 2). For simplicity, *hx* and *hz* are defined 1, and input *capa* is matrix in Eq. 4.4.1.

The output *nv* is 2.5, as expected.

## 4.5 Volumes of 3D vortex clusters

As stated before, the determination of cluster volumes is relevant for tuning correctly the vortex identification method, described in Section 4.2. However, at first sight this process seems more complex and more computationally demanding than the ones described before, as a 3D cluster is analysed all the way through. Moreover, remember that domain points in wall-normal direction do not have a constant spacing, as it is the case in streamwise and spanwise directions. This fact will be included in Algorithm 3.

The main idea behind the algorithm in charge of estimating a vortex cluster volume is simple. Given a cluster, algorithm takes its points located on the lowest XZ plane, and calculates their area, proceeding as in Algorithm 2. Nevertheless, each time an area contribution is estimated, algorithm checks the points over the selected square, which would conform a rectangular prism. Finally, based on the completeness of the lower and the upper squares, as well as on the wall-normal spacing, Algorithm 3 estimates a volume contribution.

In other words, in Algorithm 2 cluster area was based on the sum of $(hx \cdot hz)$ area contributions. Here, in Algorithm 3, cluster volume rests on the sum of $(hx \cdot hz \cdot \Delta y)$ volume contributions, being $\Delta y$ the spacing in wall-normal direction.

Algorithm 3 is implemented in a Matlab function called *vortexvol3D*. As well as on the previous sections, now the inputs and outputs of this algorithm are presented. The function takes as inputs:

- **vortex**: Matlab structure with an only field called *nodes*. Each field position contains a matrix with the points corresponding to a certain vortex cluster. The size of this matrix is $3 \times N_{points}$. The size of *vortex* goes from 1 to the number of identified vortex clusters.
- **matrix_chong**: Identification matrix calculated through Chong method, where the only possible values are 0 and 1. Size: $N_x \times N_z \times N_y$.
- **hx**: constant distance between points in streamwise direction. This distance should be introduced in meters. Size of this variable: $1 \times 1$.
- **hz**: constant distance between points in spanwise direction. This distance should be introduced in meters. Size of this variable: $1 \times 1$.
- **y**: array with the position of the wall-normal points. Size of this variable: $N_y \times 1$.

On the contrary, the function gives as output:

- **volumes**: array with the volume of each vortex cluster, preferably in $m^3$. Its size is $1 \times N_{clusters}$.

Algorithm 3 describes the structure of the function responsible for estimating the vortex clusters volumes. However, this function has two Matlab nested functions, which constitute inner layers of the algorithm.

The first nested function is called *vortexvol_adapted*. Given a $(hx \cdot hz \cdot \Delta y)$ rectangular prism, its aim is to calculate how many points on the lower wall-parallel plane integrate the lower face of the prism. This approach is completely based on Algorithm 2. The main difference is that *vortexvol_adapted* does not gives a result, but calls the second nested function, which evaluates how many points on the upper wall-parallel plane contribute to the volume. The second nested function is called *makeit3D*, and it is explained in Algorithm 4.

For the sake of completeness, Figure 4.7 depicts an example of how Algorithm 3 and 4 estimate the contribution of the prism referred to a given vortex cluster point. See that as in cluster areas estimation, a given point on the low wall-parallel plane is the reference of a whole geometry.

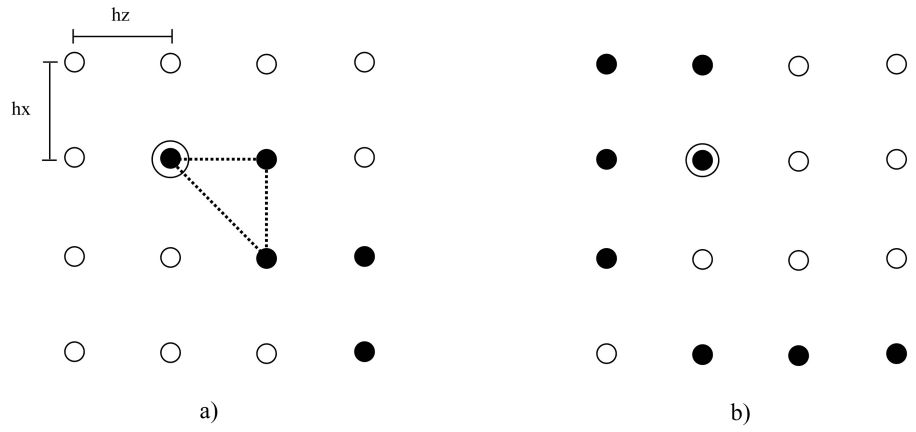


Figure 4.7: Example on how works the cluster volume determination. a) Chong wall-parallel plane (XZ) located below wall-parallel plane in b). Black points denote vortex points, white points denote no-vortex points. Circled point in a) is the reference point. Its position in the upper wall-parallel plane b) is also circled for clarity.

First nested function starts from the circled point in Figure 4.7 a). Acting in accordance with Algorithm 2, it determines that there is half-square associated to the circled point, as we see in the picture. It sends this result to the second nested function, which concludes that over the half-square only one point (circled) constitutes the volume contribution. As a result, we have three points down and one point up. This is a triangular pyramid, whose volume is $\frac{1}{3} \cdot \frac{hx \cdot hz}{2} \cdot \Delta y$. Hence, this is the volume contribution of the reference point in Figure 4.7 a).

All the possible volume contributions are collected in Table 4.2.

Now, main function and second nested function are explained in Algorithm 3 and Algorithm 4, respectively. See that first nested function is namely a slight modification of Algorithm 2, so it will not be further detailed.

**Algorithm 3:** Vortex cluster volume estimation. Main function.

```
1  Function vortexvol3D:
   Data: vortex, matrix_chong, hx, hz, y
   Result: volumes
2  Preallocation of volumes;
3  for Each vortex cluster identified do
4      Create variable vpoints with all the points of a selected cluster;
5      Initialize variable vol, which allocates the cluster volume;
6      All cluster points are sorted. First in streamwise direction; then, spanwise and
        finally, wall-normal direction;
7      Initialize variable pref. This is the first point, whose wall-normal coordinate
        dictates which the first wall-parallel reference plane is;
8      for Each cluster point do
9          if Selected point pertains to the next wall-parallel plane then
10             Calculate wall-normal distance between reference plane and the next
                wall-parallel plane. That is, Δy ;
11             The first nested function is called with all the points placed in
                reference plane;
               /* Now this algorithm jumps to the function
                  vortexvol_adapted.                                    */
12             Variable pref becomes the wall-normal coordinate of the point placed
                on the next wall-parallel plain. This is the n-point.
13     Cluster volume is stored in main function output;
```

Regarding the inputs in Algorithm 4, variable *ap* means area points. This is the number of points detected by the first nested function. Its value goes from 1 to 4.

On the other hand, variable *flag_down* has a more complex background. If function *vortexvol_adapted* detects a half-square or inclined line through Lines 24 or 26 in Algorithm 2, which are modifications on the initial approach, function *makeit3D* must know that the points to analyse in the above wall-parallel plane are E, NE and N, instead of E, SE and S. See Figure 4.5.

Therefore, if *flag_down* is equal to 1, Algorithm 4 considers the points in the square depicted in Figure 4.5 for volume estimation. Otherwise, it considers the square conformed by points Origin (circled), E, NE and N.

Finally, its output *vol* is the volume contribution linked to the reference point selected in first nested function, called *vortexvol_adapted*.

**Algorithm 4:** Vortex cluster volume estimation. Second nested function.

```
1  Function makeit3D:
   Data: ap, flag_down
   Result: vol
2  if flag_down is 1 then
3      Store Chong values of the points conforming the square in Figure 4.5. See
         that value on circled point is now also stored;
4      Sum them in variable vp;
5      else if flag_down is 0 then
6          Store Chong values of the points conforming the upper square in Figure
             4.5. This are Origin, N, NE and E.
7          Sum them in variable vp;
8  if Variable vp is not 0 then
       /* With this condition, algorithm ensures that there are upper
          points to conform a volume.                                    */
9      Sort both variables vp and ap. This ensures that always vp ≤ ap;
10     if Variable vp is 1 then
11         if ap is 1 then
12             vol is 1/3 · (0.125 hx hz) · Δy;          /* Pyramid base per 0.125 */
13             else if ap is 2 then
14                 vol is 1/3 · (0.25 hx hz) · Δy          /* Pyramid base per 0.25 */
15             else if ap is 3 then
16                 Variable vol is 1/3 · (hx hz)/2 · Δy;          /* Triangular pyramid */
17             else if ap is 4 then
18                 Variable vol is 1/3 · (hx hz) · Δy;       /* Rectangular pyramid */
19     if vp is 2 then
20         if ap is 2 then
21             Variable vol is 0.25 · (hx hz) · Δy;       /* Prism base per 0.25 */
22             else if ap is 3 then
23                 Variable vol is 0.5 · (hx hz)/2 · Δy; /* 0.5 Prism of triang.  base */
24             else if ap is 4 then
25                 Variable vol is 0.5 · (hx hz) · Δy;  /* Half rectangular prism */
26     if vp is 3 then
27         if ap is 3 then
28             Variable vol is 0.5 · (hx hz) · Δy;          /* Triangular prism */
29             else if ap is 4 then
30                 Variable vol is 0.75 · (hx hz) · Δy;     /* Rectangular prism per
                     0.75 */
31     if vp is 4 then
           /* Due to sorting, here ap can only be 4.                     */
32         Variable vol is (hx hz) · Δy;                  /* Rectangular prism */
```

For clarity, the volume contribution for each number of area points (ap) and volume points (vp) is presented in Table 4.2. This information is displayed according to Algorithm 4.

| Volume Points ($vp$) | Area Points ($ap$) | Volume Contribution ($vol$) |
|---|---|---|
| 1 | 1 | Triangular pyramid. Base per 0.125 |
| 1 | 2 | Triangular pyramid. Base per 0.25 |
| 1 | 3 | Triangular pyramid |
| 1 | 4 | Rectangular pyramid |
| 2 | 2 | Rectangular prism. Base per 0.25 |
| 2 | 3 | Triangular prism. Base per 0.5 |
| 2 | 4 | Rectangular prism. Base per 0.5 |
| 3 | 3 | Triangular prism |
| 3 | 4 | Rectangular prism. Base per 0.75 |
| 4 | 4 | Rectangular prism |

Table 4.2: Volume contribution according to the number of points on the base and on top of the geometry.

Finally, the volume formula of the geometries named in Table 4.2 are displayed:

- Pyramid: $\frac{1}{3} \cdot Base \cdot \Delta y$
- Prism: $Base \cdot \Delta y$

Base area depends on the base geometry and on the possible reduction factor employed, as specified in Table 4.2.

## 4.6 Field characteristics on vortex points

As seen until now, the size of the vortex clusters present in the simulation is not only relevant, but also necessary for our post-process. One can gather relevant information from the variations in size, when comparing between near-wall and far from wall vortexes. Additionally, size identification makes possible to detect coherent vortex structures near the wall, which are extensively described in numerous papers ([2], [26]), among others.

However, it is also relevant to study the properties of the field; i.e. Reynolds stress or vorticity, on the points where a vortex cluster is present. This idea shows us if there is any tendency between field characteristics and the presence of a vortex. Moreover, we can compare these properties with the streamwise velocity field, when a vortex is present. It may be interesting to observe if there is any influence between vortex clusters and large rolling structures in Couette flow. This is later presented in Section 6.3.

The next algorithm was created in order to study the organization of vortex clusters in comparison with streamwise velocity structures. Furthermore, this algorithm is able to show field properties on vortex cluster points, and finally classify them according to their position on the velocity field.

In other words, our algorithm takes a specified field variable (i.e. $\langle uv \rangle$), sets to 0 all values on points without vortex, and separates positive from negative magnitudes. Then, compares each one with a filtered streamwise velocity field. This filtering let us distinguish high-speed, low-speed and neutral streamwise velocity areas. Finally, our algorithm classifies vortex areas with positive or negative magnitudes according to their position in the filtered streamwise velocity field. That is, if that vortex is on a high-speed structure, or it touches both high-speed and neutral, and so on.

Algorithm 5 is implemented in Matlab script *analisis_areas*. As it is not a Matlab function, it does not need proper inputs. Nevertheless, variables at the beginning act as inputs, so they are explained here:

- **root_dir**: path to case directories (i.e. C02P08). These directories must contain the h5 files of velocity fields.
- **filder**: path to the directory where compact finite difference matrices for wall-normal derivation (Read Section 4.1) are stored.
- **rootout_dir**: path to the directory where output h5 fields will be created, if required.
- **sep**: path separator. It may change depending on the system (Windows, Linux...)

See that in Algorithm 5, percolation limit must be specified, so percolation analysis must be performed before launching this algorithm.

A limitation of this study is that Algorithm 5 can only be applied on wall-parallel planes; in other words, it is a 2D study. Hence, one ought to think which wall-parallel planes to choose in order to obtain proper results. In addition, only 4 characteristics are analysed. These are Reynolds stress $\langle uv \rangle$, and vorticity components ($\omega_x$, $\omega_y$, $\omega_z$).

As well as in Section 4.5, our main algorithm has inner local functions, which are called during execution. First local function is called *file_velocity_expansion*. Its aim is to derive the velocity fields stored in an input h5 file, and give as an output their derivatives in each coordinate as well as the original velocity fields. Since this function is based on the procedure explained in Section 4.1, it will not be further detailed.

Second local function is called *distribucion*. Its steps are explained in Algorithm 6. Here, a vorticity or Reynolds stress field is taken as input in *campo_analisis*. Additionally, the streamwise field is given in *campo_compara*. This local function filters the streamwise field through Algorithm 7 and classifies positive and negative values in *campo_analisis*, separately, based on the filtered streamwise field.

On the other hand, third local function *filtra_campo* is in charge of filtering a velocity field, generally a streamwise field (input $T$). Procedure steps are detailed in Algorithm 7. See that the threshold is the standard deviation of the field. However, the threshold can be multiplied by input *factor*. This would modify the filtering of the field.

**Algorithm 5:** Main script for the analysis of field characteristics on vortex points.

**Result:** Classification of field characteristics based on streamwise velocity field.

1 Load the input data (roots and separator). Set also the name of the velocity fields h5 file;

2 Launch first local function *file_velocity_expansion*; `/* Here, algorithm extracts the derived velocity fields from the original fields. */`

3 Calculate Reynolds stress $\langle uv \rangle$ on a given wall-parallel plane;

4 Calculate vorticity components ($\omega_x$, $\omega_y$, $\omega_z$) on a specified wall-parallel plane;

5 Introduce the percolation limit corresponding to the studied case;

6 Perform vortex identification through Chong method. If desired, specify the studied wall-parallel plane, so unnecessary operations are avoided;

7 Filtrate Reynolds stress and vorticity component planes, so only remain the values on points that contain a vortex;

8 Classify the filtrated Reynolds and vorticity planes according to the streamwise velocity structures. Classification is done for positive values and negative values of the filtrated planes; `/* Here, second local function is called. */`

9 Classifications (outputs) are stored in a h5 file;

10 Show a pseudocolor plot *pcolor* of each filtered field property. Here one can distinguish between positive and negative magnitudes.

**Algorithm 6:** Analysis of field characteristics on vortex points. Local function 2.

**Function** `distribucion`:
**Data:** campo_analisis, campo_compara, hx, hz, modo
**Result:** dist_pos, dist_neg

Define filtering factors for the streamwise velocity field;

Preallocate function outputs;

Filter input *campo_analisis*, so positive values become 1, and negative values become -1. Values on no-vortex points remain 0;

**for** *Each filtering factor* **do**

    Obtain a filtered streamwise velocity field according to the filtering factor selected by the For-bucle. `/* In this step, third local function is launched. */`

    Classify the positive values in *campo_analisis*, based on the filtered velocity field;

    Classify the negative values in *campo_analisis*, based on the filtered velocity field;

        `/* Classification is made by the fourth local function */`

    Store the results in the preallocated matrices;

**if** *Input variable called modo is 'p'* **then**

    Express the results in percentage of total vortex surface;

**Algorithm 7:** Filter the streamwise velocity field. Local function 3.

**Function** `filtra_campo`:
**Data:** T, factor
**Result:** Filtered streamwise velocity field. Possible values are $\{-1, 0, 1\}$

**if** *factor is empty* **then**

    Set *factor* to 1;

Subtract the mean value of the wall-parallel plane from all values; `/* Variable Tm */`

Preallocate function output;

Create filtering threshold ($st$) as the standard deviation of variable $Tm$ multiplied by *factor* `/* 0.5 ≤ factor ≤ 1 */`

At a given point $\vec{x}$: **if** $Tm\,(\vec{x}) > st$ **then**

    Filtered velocity field at $\vec{x}$ becomes 1; `/* High-speed point */`

    **else if** $Tm\,(\vec{x}) < -st$ **then**

        Filtered velocity field at $\vec{x}$ becomes -1; `/* Low-speed point */`

        **else**

            Filtered velocity field at $\vec{x}$ becomes 0; `/* Neutral point */`

The aim of the fourth local function is to perform the classification of vortex clusters, which are filtered according to a given magnitude. For example, positive Reynolds stress. A given vortex cluster can touch a high-, low- or neutral speed region, or even a combination of them. According to this fact, Algorithm 8 classifies this vortex area in a class.

**Algorithm 8:** Classify vortex clusters areas. Local function 4.

```
1  Function filtra_campo:
   Data: Q, nt, hx, hz
   Result: Vortex areas classified according to their position on the filtered velocity
           field.
2  Launch vortex clusters identification;
                                          /* Section 4.2.  Algorithm 1  */
3  Extract the areas of all the clusters;
                                          /* Section 4.4.  Algorithm 2  */
4  Preallocate function output;
5  for Each vortex cluster do
6      Determine which kind of streamwise structures are touched by the selected
        cluster. These can be high-speed, low-speed, neutral or a combination;
       /* Variable aux stores the indicator of these structures; that
       is, a combination of {−1, 0, 1}.  */
7      if aux is 0 then
8          The cluster is classified in neutral;                  /* Class 3 */
9          else if Number of non-zero values in aux is 1 then
               /* Here the possible combinations are 1, −1, {0, 1} or
                  {−1, 0}                                                  */
10             if Length of aux is 1 then
                   /* Possible combinations:  -1, 1                       */
11                 if aux is 1 then
12                     The cluster is classified in high-speed;   /* Class 1 */
13                 else
14                     The cluster is classified in low-speed;    /* Class 2 */
15                 else
                       /* Possible combinations:  {−1, 0}, {0, 1}         */
16                     if Minimum value in aux is -1 then
17                         Cluster is low-speed and neutral;      /* Class 5 */
18                     else
19                         Cluster is high-speed and neutral;     /* Class 4 */
20     else
           /* Combination {−1, 0, 1}                                      */
21         Cluster touches three kinds of structures;             /* Class 6 */
```

# Chapter 5

# Characterization of velocity fields

In this chapter we focus on the description of velocity and vorticity fields present in each case. We will depict our measurements in diverse wall-parallel planes; mainly, near the moving wall, in the channel center and near the stationary wall. Moreover, following the common procedures in the literature, we will see how to extract relevant information from the coherent velocity structures through two-point correlation analysis and spectral-density plots. Indeed this information is becomes relevant when extracted from our very-long computational domain of size $128\pi h \times 2h \times 6\pi h$ (Read Chapter 3), because it shows for the first time the averaged streamwise length of the coherent velocity structures at $Re_\tau = 125$.

Following this line, we will show the link between the coherent velocity structures and the averaged Reynolds stress along the wall-parallel planes. This approach makes easier to understand how these velocity structures, when present, create long counter-rotating rolls, which can extend along the domain length.

Finally, employing the algorithms described in Section 4.6, some quantities on vortex points, such as Reynolds stress or vorticity, will be compared with the velocity structures near these points.

## 5.1 Velocity and Reynolds stress fields

Before extracting the statistical data from the velocity in our cases and domains, it is mandatory to understand which kind of structures we found in our simulations. Bearing this in mind, one achieves a better understanding of the results extracted through two-points correlations and spectral-density.

For this purpose, here we compare wall-parallel planes of filtered instantaneous and mean velocity in each case. Additionally, they are gathered according to their wall-normal distance to the walls. Finally, these results are contrasted with similar studies.

In Figure 5.1 filtered streamwise velocity fields at instantaneous simulation times are depicted on the left. As one can read in each caption, these figures start from case C00P10 (pure Poiseuille) on the top to C10P00 (pure Couette) on the bottom. Filtering in these fields was carried out employing Algorithm 7, explained in Section 4.6. In this case, the threshold was the standard deviation among all the velocity values in the selected wall-parallel plane. See that now one can differentiate between three zones of colour:

- **Yellow**: high-speed regions, where local streamwise speed is above the standard deviation.
- **Light blue**: neutral regions, where local streamwise speed is in the range of the standard deviation.
- **Dark blue**: low-speed regions, where local streamwise speed is below the standard deviation.

All these regions were already mentioned in Section 4.6, as they were employed for the classification of vortex areas with a given magnitude.

On the right column, the streamwise mean velocity of each case is depicted without filtering. This magnitude helps to find patterns visible after analysing many instantaneous fields. Finally, the channel center point at $y/h = 0.065$ was selected on purpose in order to compare these figures with the results in Gandia-Barbera et al. [23].

As we can see in Figure 5.1, in pure Poiseuille there is no clear pattern among the filtered streamwise velocity structures. The filtered field is composed by short and scattered structures. So, we can see that low-speed and high-speed regions come closer and get away with no clear arrangement. Furthermore, if we compare the filtered instantaneous with the mean streamwise velocity field, we can appreciate the lack of organization among these structures.

The same statements agree with the case C02P08, in which the Couette contribution is still considerable small.

In case C04P06 we appreciate for the first time structures of the same kind organizing in order to create longer structures than the ones visualized in previous cases. This tendency is confirmed once we analyse the mean flow in Figure 5.1f.

In case C06P04 the streamwise velocity structures arrange themselves in tight structures. These structures sometimes reach both domain ends in streamwise direction. However, we notice in the mean field that the structure are not strong enough. Additionally, an alternating pattern of structures along the spanwise direction is not developed yet.

Cases C08P02 and C10P00 (pure Couette) show another scenario. Here we can see that streamwise structures have completely arranged creating strong structures that touch both streamwise sides of the domain. Moreover, their mean velocity fields show a clear spanwise pattern, which alternates between low-speed, neutral, high-speed and so on.

The conclusions about case C10P00 are confirmed in Gandía-Barberá et al. [23]. Here the authors state that the clear strip pattern developed in C10P00 is a direct consequence of the too short domain employed and the periodic boundary conditions (Read Section 2.2), specially in streamwise direction.

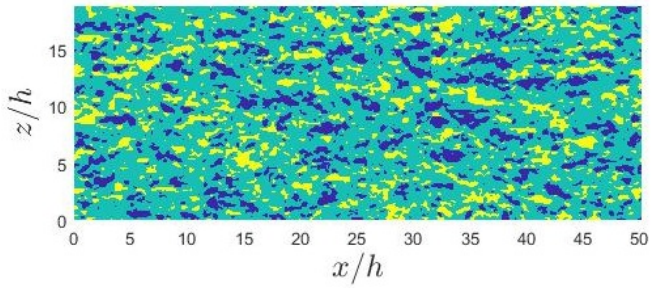


(a) C00P10. Instantaneous

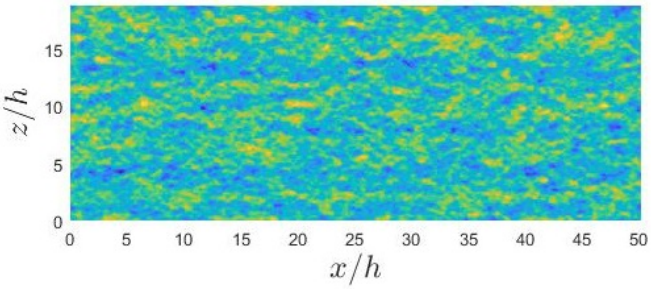


(b) C00P10. Mean

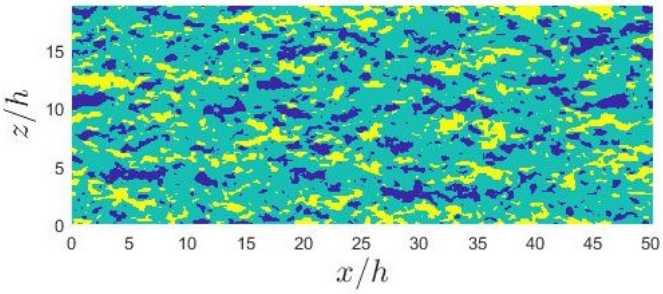


(c) C02P08. Instantaneous

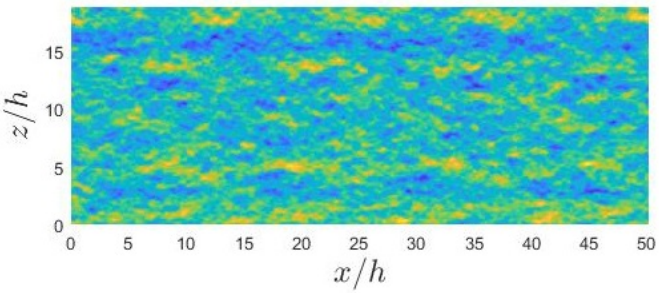


(d) C02P08. Mean

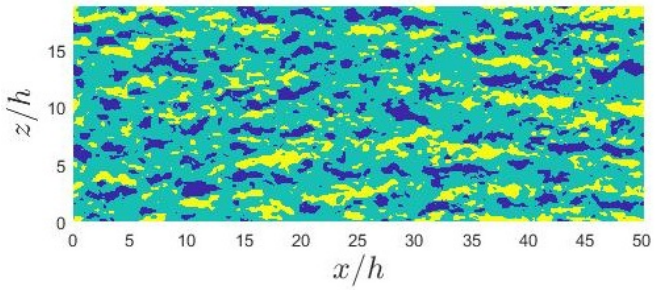


(e) C04P06. Instantaneous

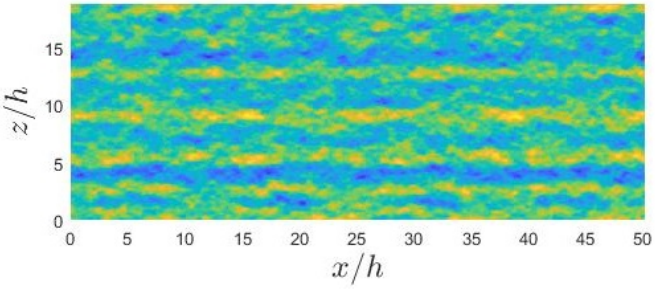


(f) C04P06. Mean

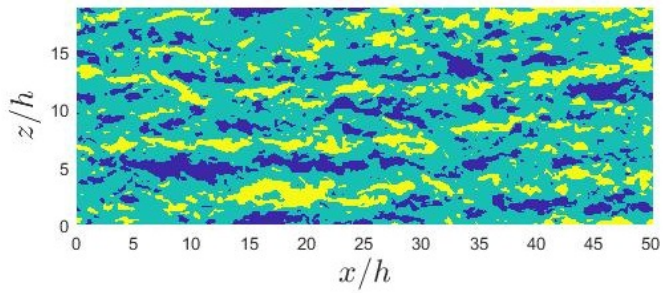


(g) C06P04. Instantaneous

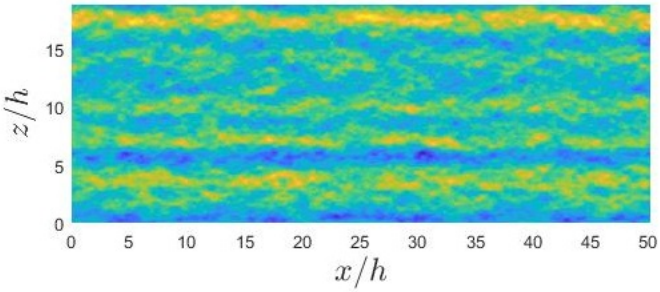


(h) C06P04. Mean

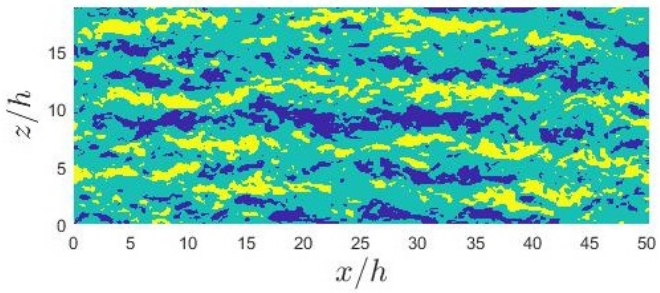


(i) C08P02. Instantaneous

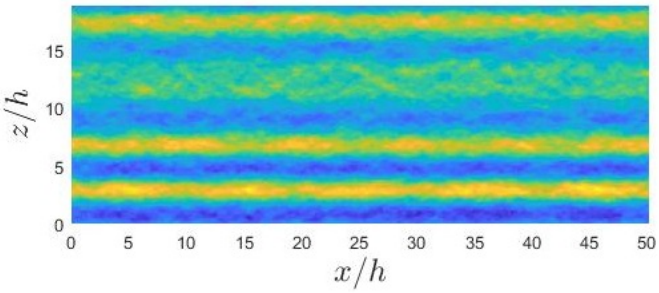


(j) C08P02. Mean

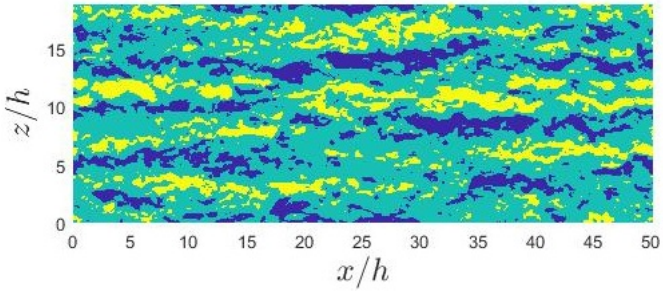


(k) C10P00. Instantaneous

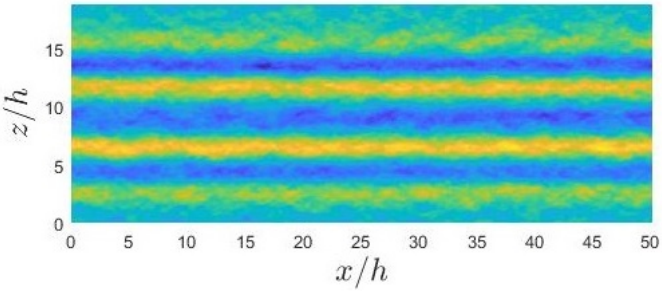


(l) C10P00. Mean

Figure 5.1: Filtered streamwise velocity wall-parallel planes. $y/h = 0.065$, channel center.

This fact was previously described by M. Lee and Moser [8], who compared simulations at a given $Re_\tau$ in short and large domains.

As one can see in Figure 5.1, all pictures are taken from our shortest domain, of length $16\pi h$. As a result, we are not able to determine the streamwise length of the velocity structures present in C10P00 or C08P02. Other authors, such as Pirozzoli et al. [3] or Tsukahara et al. [20], could not measure their length to this issue.

In Figure 5.2 a fragment of a filtered streamwise field of C10P00 in a domain of length $128\pi h$ is presented. Inside the red box of length $100h$ we appreciate on top two velocity structures. A high-speed one covering from 180 to 230, and a low-speed one from 230 to 280. Additionally, a similar pattern is seen on the bottom inside the red box; however, it starts with a low-speed structure and changes at 230 to a high-speed one. This behaviour makes us asseverate that the actual length of a structure is $50h$, approximately [23]. This result will be confirmed later in Section 5.3 by estimating a two-point correlation in streamwise direction.

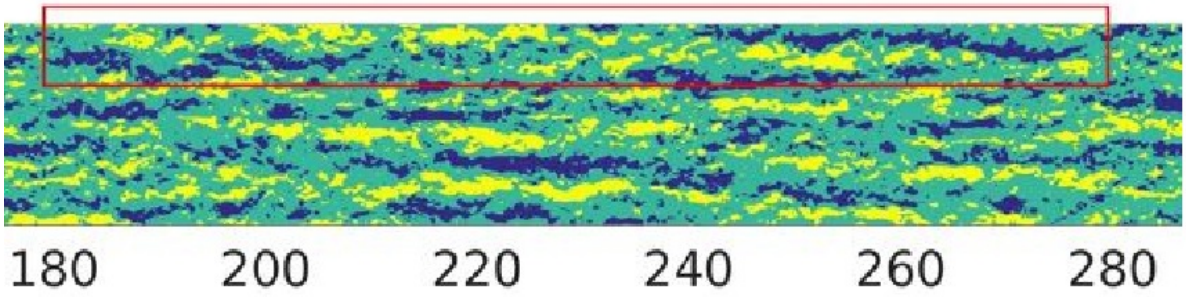


Figure 5.2: Fragment of the filtered streamwise velocity field in case C10P00. Long domain, length $128\pi h$. Extracted from Gandía-Barberá et al. [23]

Furthermore, notice in Figure 5.2 that velocity structures have a slight inclination along the streamwise direction. Once the periodic boundary conditions are far from the analysed region, structures become slightly tilted at moderate $Re_\tau$; that is, around $Re_\tau = 220$ and lower than $Re_\tau = 500$, as M. Lee and Moser [8] could estimate. The authors state that the coherence of the structures underlying the correlations are strongly dependend on the Reynolds number, and their simulation at $Re_\tau = 93$ seems to be too low in Reynolds number to show inclined structures. However, their simulation at $Re_\tau = 500$ shows an insignificant inclination angle, as this angle is also strongly dependent on $Re_\tau$. Since our case at $Re_\tau = 125$ is this interval, we can appreciate an inclination angle in Figure 5.2.

Now, the reader has understand the distribution of streamwise velocity structures in the domain center along the transition between pure Poiseuille flow and pure Couette. However, there is still an important question, which is: why are these structures relevant for our analysis?

As stated in the Abstract, we seek for the longest turbulent structures in Couette flows, in order to determine their stability and origin. Moreover, we want to link these structure with the large contrarrotating rolls present also in Couette flows, which were previously detected by many authors, both experimentally and numerically.

According to Pope [1] in Section 7.4, in the near-wall region ($y^+ < 100$) of turbulent boundary layers pairs of counter-rotating streamwise vortices or rolls are identified as the dominant vortical structures. These structures are described in Figure 5.3. In this simplified picture, the fluid moving away from the wall with a positive wall-normal velocity ($v$) has a relatively reduced axial velocity, which is also depicted in Figure 5.3. The author also asserts that these points are associated with wall bursting, a common event in near-wall turbulence.

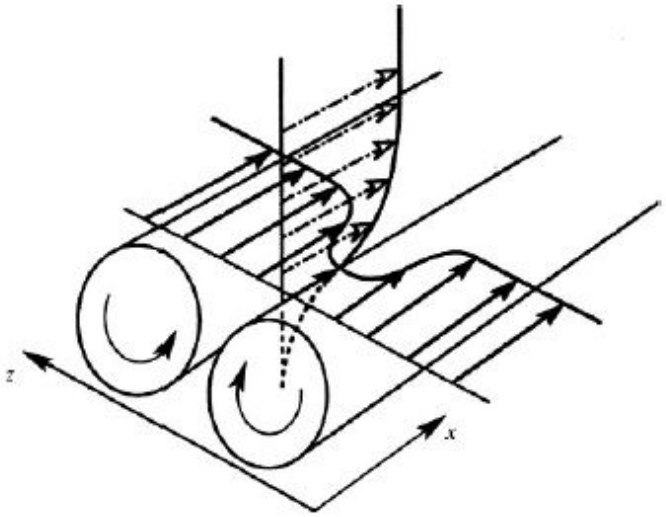


Figure 5.3: Counter-rotating vortices dominant in the near-wall region of turbulent boundary layers. Image from Pope [1], page 326.

On the other hand, in Figure 5.5 we have depicted time- and streamwise-averaged images of $u/u_\tau$ for the transition between pure Couette and pure Poiseuille in the small domain, $16\pi h$. In this Figure we appreciate the distribution of streamwise velocity structures in a YZ plane; that is, along the wall-normal and spanwise directions.

Notice that in Figure 5.5, we have depicted the fluctuating component of the streamwise velocity, according to the Reynolds decomposition (Eq. 1.2.1). Hence, this value may be negative despite the instantaneous streamwise velocity is always positive.

In pure Poiseuille (C00P10) or cases with strong Poiseuille contribution (C02P08) we can see that there is an alternating pattern of high- and low-speed structures near the walls. In the domain center, the mean values are around zero. If we remind the Reynolds stress distribution along the wall-normal direction (Figure 3.2b), we see that Reynolds stress peaks in Poiseuille or quasi-Poiseuille flows are near the walls. This stress is responsible for the production of turbulent kinetic energy is this regions. Moreover, in Figure 3.2b we notice that the Reynolds stress is nullified in the channel's center. The idea of linking the time- and streamwise-averaged fields of $u/u_\tau$ with the Reynolds stress was previously suggested by M. J. Lee and Kim [28], and developed in Gandia-Barbera et al. [23].

As soon as we reach intermediate states, such as C04P06 or C06P04, the structures increase in height from the stationary wall at $y/h = -1$ to the moving wall at $y/h = 1$. This fact stays in accordance with the distribution of Reynolds stress in Figure 3.2b, since

the crossing position tends to the moving wall as the Couette contribution increases.

Finally, in Couette dominant cases (C08P02 and C10P00) we can see for the first time that the streamwise velocity structures occupy the whole height of the channel. Additionally, by comparing the colorbars of each case we also conclude that these structures become stronger as soon as the Couette contribution becomes relevant enough.

M. J. Lee and Kim [28] identified these structures and their distribution for a plane Couette flow at $Re_\tau \approx 170$ in a domain of size $(L_x, L_z, L_y) = \left(4\pi h, \frac{8}{3}\pi h, 2h\right)$. The authors employed the same approach as in Figure 5.5. However, they went one step further and projected on their figure the velocity vectors in wall-normal and spanwise direction. This is depicted in Figure 5.4. Notice that dark blue regions in Figure 5.5 are represented with a continuous line in Figure 5.4. Yellow regions are represented with intermittent lines. Green regions depict the transition between both kind of lines.

On the one hand, we can see on the right region of Figure 5.4 (b), the tendency is to develop strong negative wall-normal velocity ($v << 0$) in the core of high-speed structures (yellow regions in Figure 5.5), and strong positive wall-normal velocity ($v >> 0$) in the core of low-speed velocity structures (blue regions in Figure 5.5). Moreover, at both regions the spanwise velocity is almost null.

On the other hand, regions of strong spanwise velocity are located near the walls on the transitions between positive and negative $u$ regions. In addition, transitions in the channel center create regions of almost no spanwise or wall-normal velocity.

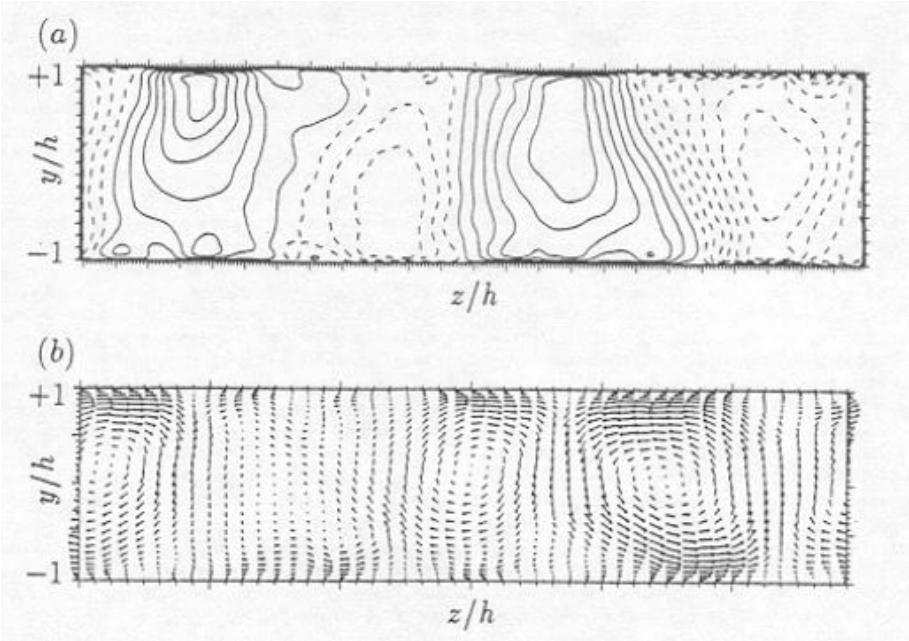


Figure 5.4: Velocity field of the time-averaged large-eddy field in a plane Couette flow; (a) contours of $u$ in the yz-plane, where —— is $u \geq 0$ and - - - - is $u < 0$; (b) velocity vectors $(v, w)$ projected on the yz-plane. Extracted from M. J. Lee and Kim [28].

Based on the above description of Figure 5.4, one can easily see the relation between the coherent streamwise velocity structures and the secondary flow movement, which develop counter-rotating pairs of vortices.

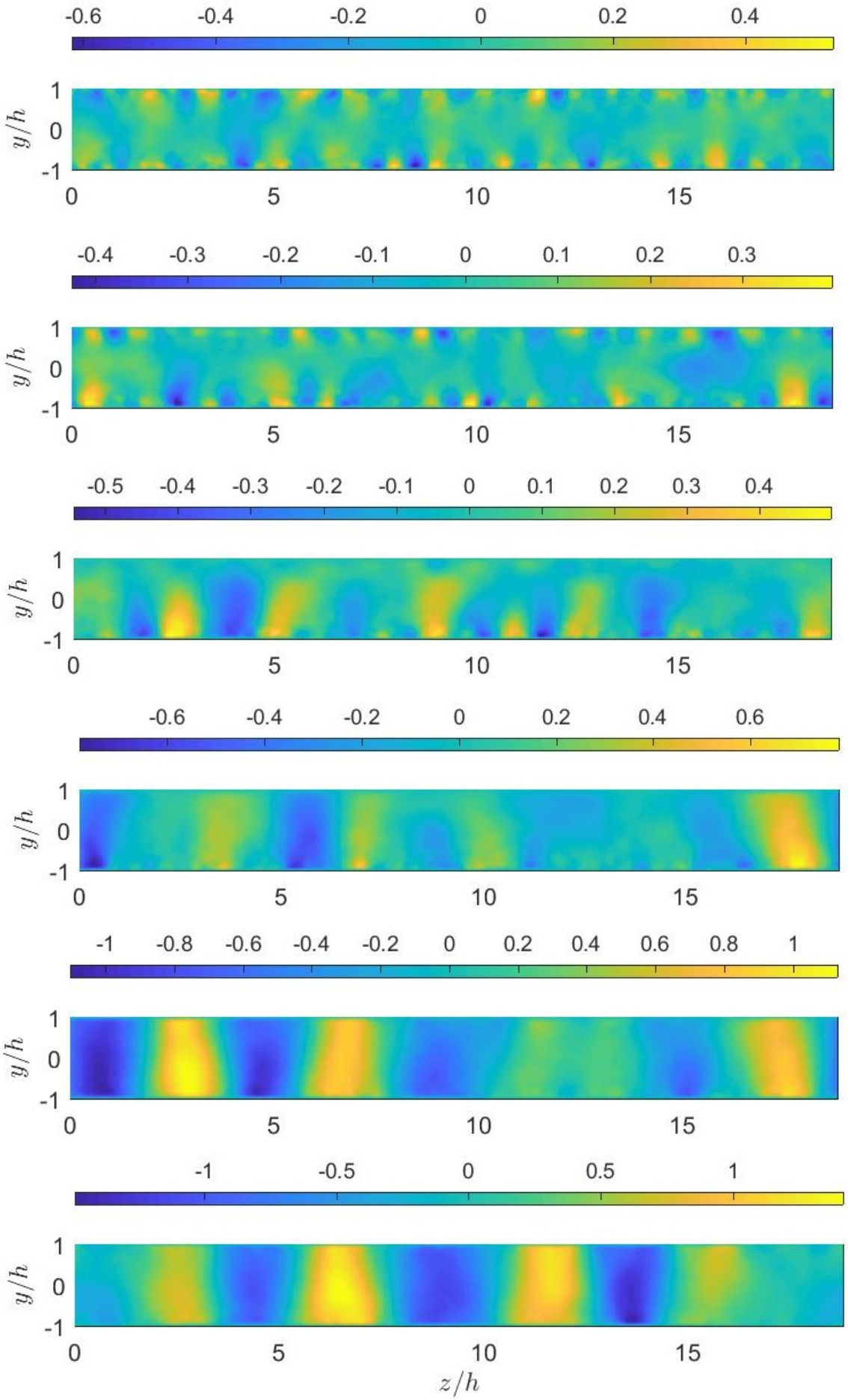


Figure 5.5: Time- and streamwise-averaged images of $u/u_\tau$ for the cases, top to bottom, C00P10, C02P08, C04P06, C06P04, C08P02 and C10P00

Now, going back to Figure 5.1, we can demostrate that as the streamwise structure occupy the whole channel length in short domains, the counter-rotating rolls do so. This explains why we employed a very-long domain in order to analyse the real extent of these rolls.

Going one step further, in Gandia-Barbera et al. [23] the authors performed a similar analysis by illustrating the contours of Reynolds stress in yz-planes, instead of velocity vectors as in Figure 5.4. Through this approach, the presence of counter-rotating rolls is linked to the distribution of Reynolds stress along the wall-normal direction. These fields are depicted in Figure 5.6, following the same order as in Figure 5.5. Additionally, each case can be compared with the Reynolds stress distribution depicted in Figure 3.2b.

In pure Poiseuille flow we notice both layers of substantial Reynolds stress near both walls. Near $y/h = 1$ its value is positive, and near $y/h = -1$ it is negative. However, if we compare this field with the $u/u_\tau$ field of the same case in Figure 5.5, we notice an alternating pattern of positive and negative wall-normal velocity near both walls. For understanding this step, see Table 5.1.

| | | |
|---|---|---|
| $uv/u_\tau^2 > 0$ | $u/u_\tau > 0$ | $v/u_\tau > 0$ |
| | $u/u_\tau < 0$ | $v/u_\tau < 0$ |
| $uv/u_\tau^2 < 0$ | $u/u_\tau > 0$ | $v/u_\tau < 0$ |
| | $u/u_\tau < 0$ | $v/u_\tau > 0$ |

Table 5.1: Relationship between Reynolds stress ($uv^+$), and stream- or spanwise fluctuating velocity.

The alternating wall-normal fluctuating velocity at near-wall region creates counter-rotating rolls of small width and length. For visualizing these near-wall rolls, their axis are located in the near-zero $u/u_\tau$ regions between positive and negative values. Moreover, each positive or negative value is the border region between both counter-rotating rolls, where wall-normal velocity reaches its maximum. These characteristics were also seen in Figure 5.4, thanks to velocity vectors.

As the reader might remember, near-wall ($y^+ < 100$) counter-rotating structures were previously described in this section, according to Pope [1], and depicted in Figure 5.3.

As soon as some Couette contribution is applied in case C02P08, the Reynolds stress magnitude decreases and zero values move slightly to the moving wall at $y/h = 1$, as one can see also in Figure 3.2b.

In cases C04P06 and C06P04, counter-rotating rolls are developing due to the increasing contribution of Couette flow. Concretely, in C04P06 Reynolds stress distributions do not reach the moving wall yet. This wall is reached in case C06P04 and so on. So we state that counter-rotating rolls are present in this range of cases, as it was asseverated in Gandia-Barbera et al. [23].

However, we see that as soon as some Poiseuille contribution is present in the flow, Reynolds stress magnitude decreases. Thus, strongest values are only present in pure Couette flow; that is, case C10P00. This is also confirmed in Figure 3.2b.

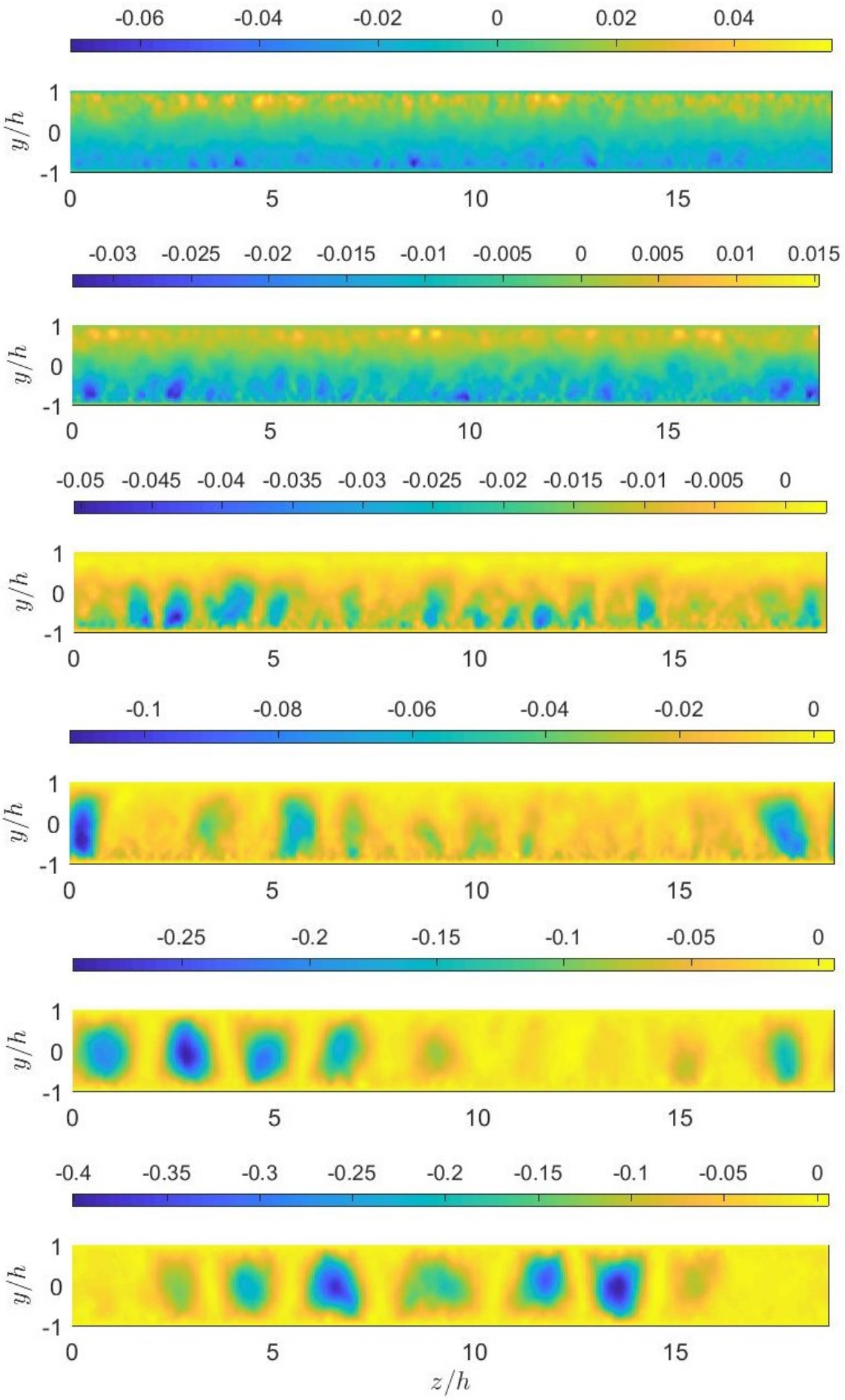


Figure 5.6: Time- and streamwise-averaged images of $\langle uv \rangle / u_\tau^2$ for the cases, top to bottom, C00P10, C02P08, C04P06, C06P04, C08P02 and C10P00

Finally, following Table 5.1 we can relate our $u^+$ and $\langle uv \rangle^+$ fields at C10P00 with velocity vectors depicted by M. J. Lee and Kim [28] in Figure 5.4. Notice that each positive and negative $u^+$ structure at C10P00 in Figure 5.5 is located on a strong negative Reynolds stress region at C10P00 in Figure 5.6. Therefore, we have an alternating positive and negative fluctuating wall-normal velocity, as described in Figure 5.4.

Now the reader will understand that in regions of $\langle uv \rangle^+ \approx 0$, the wall-normal velocity becomes zero. Here, located in the channel center, we encounter the center of the counter-rotating rolls.

In Figure 5.7 time- and streamwise-averaged fields of $w/u_\tau$ are depicted following the same case order as in the previous figures. In pure Poiseuille flow, we can detect near the walls some positive structures above negative structures or vice versa. One pair of structures represent a roll. However, we can also see that these structures do not follow a clear pattern near the wall. One must remember that their velocity intensities are not as strong as Couette rolls.

Surprisingly once a slight Couette contribution is present; i.e. C02P08, spanwise velocity magnitude as well as all the other magnitudes depicted ($u^+$ and $\langle uv \rangle^+$) tend to slightly diminish. Additionally, we see that the alternating pattern of the spanwise fluctuating velocity suddenly disappears near the moving wall at $y/h = 1$. At the stationary wall intensities also decreased.

During the Poiseuille-Couette transition; i.e. C04P06 and C06P04, we detect two steps. First, spanwise velocity near the moving wall increases its isotropy, and near the stationary wall, structures elongate. An overall positive spanwise velocity is shown in the channel center. Second, an alternating pattern of large structures near both walls is present at C06P04; however, its intensity is still low.

We notice that this pattern strengthens in the following cases until pure Couette. Here we see a clear alternating pattern which indicates the presence of counter-rotating rolls that occupy all the channel height. This pattern is less clearly depicted in Figure 5.4 through velocity vectors.

Therefore, we can properly state that at C06P04 counter-rotating rolls are present despite their intensity is low. Additionally, see that as long as Couette contribution increases from C06P04 until C10P00, the structures length slightly increases. Hence, the rolls width increases. We will later see through two-points correlation that this is the tendency.

In this section we have proven the existence of strong counter-rotating rolls in cases from C06P04 to C10P00. Hence, we can relate our results to the stability of these structures at $Re_\tau = 125$, when a Poiseuille contribution is present. This stability could not be broken in other studies. For example, Kraheberger et al. [16] found out that these rolls at $Re_\tau = 1000$ are strongly stable against wall transpiration up to $V_0^+ = 0.071$, being $V_0$ the mean wall-normal velocity.

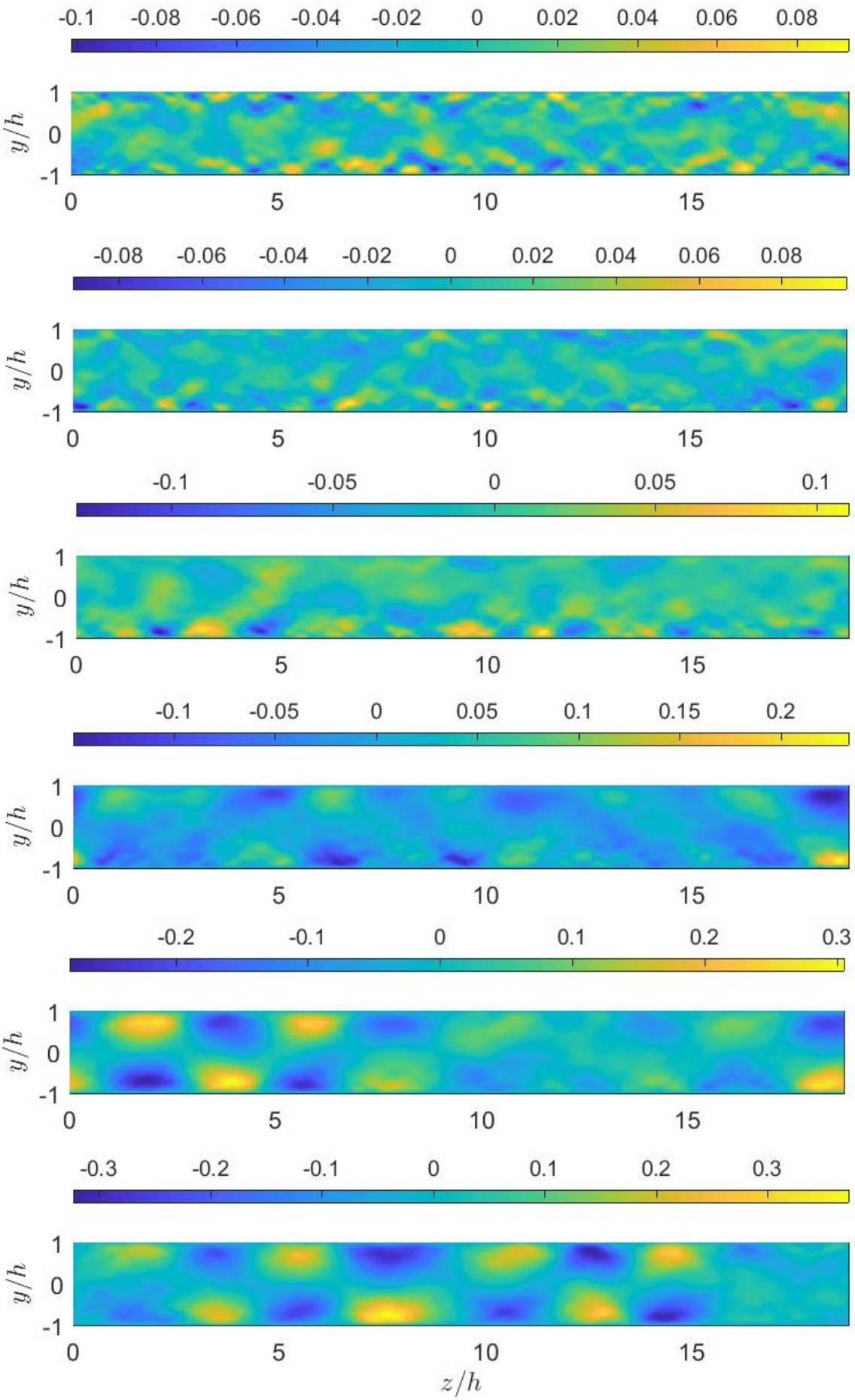


Figure 5.7: Time- and streamwise-averaged images of $w/u_\tau$ for the cases, top to bottom, C00P10, C02P08, C04P06, C06P04, C08P02 and C10P00

Now, it is relevant to explain the influences of these rolls in the flow, and also give a deeper description of them. Pirozzoli et al. [3] describe them as momentum-carrying eddies or low wave-number flow mode. This is because counter-rotating rolls in Couette flow are identified as large wave-lengths in a pre-multiplied energy spectra; that is, as low wave-numbers.

The authors also linked these rolls to the occurence of streaky patterns of alternating momentum through the channel, as we could see from the inspection of the streamwise velocity filtered field in wall-parallel planes, showed in Figure 5.1. The authors also suggest that streaks are not expected to occur in the regions, where the local mean shear is near zero.

We can proven this asseveration by comparing the streaky patterns of Couette driven flows (i.e. C06P04) and the lack of this pattern in pure Poiseuille flow (C00P10) in Figure 5.1. Moreover, we can appreciate this more clearly in the filtered streamwise velocity fields near the moving wall in Figure 5.10. Case C06P04 achieves near-zero Reynolds stress near the moving wall as seen in Figure 3.2b; this affects the pattern of its velocity structures, and develops quasi-isotropic ones.

The explanation behind this phenomena was studied by Lee, Kim & Moin [29], who discovered that streaks are not an exclusive feature of wall-bounded flows, and the presence of a solid boundary is indeed not a necessary condition. The authors showed that homogeneous turbulence subjected to intense shear exhibits coherent flow patterns which closely resemble the streaks found in the near-wall region of wall-bounded flows.

In our case, we have homogeneous turbulence along the streamwise and spanwise directions as we already stated in Section 2.2. That is the reason why our simulations can adopt periodic boundary conditions in both directions. Moreover, we appreciate that there is a intense shear stress (Reynolds stress) in the channel center for Couette-driven flows; exactly the ones that show defined streaks in this region. Thus, we agree on the statement of Lee, Kim & Moin [29].

We will see later in Figure 5.8 that near-wall regions at a stationary wall show always streaky patterns, for every case.

Following the conclusions of Lee, Kim & Moin [29], the authors noted that the formation of streaky structures is primarily controlled by the value of a dimensionless shear parameter $\sigma k/\varepsilon$, where $\sigma$ is the mean shear, $k$ is the turbulent kinetic energy, and $\varepsilon$ is its dissipation rate. This dimensionless parameter can also be considered as a measure of the ratio between the eddy turnover time $k/\varepsilon$ and the time scale of mean deformation $1/\sigma$.

However, Lam & Banerjee [30] identified the turbulent production-to-dissipation ratio $\sigma\langle uv\rangle/\varepsilon$ as the controlling parameter for the occurrence of streaks. This parameter is easier to understand as we already have the distribution of Reynolds stress in our cases. Therefore, we can forecast the presence of streaks in the streamwise velocity field by observing Figure 3.2b.

Regarding the influence of the largest structures in Couette flow with the near-wall region, Pirozzoli et al. [3] states that these large-scale motions superpose onto the near-wall turbulence, causing deviation from the universal wall scaling at sufficiently large Reynolds number. Furthermore, positive large-scale velocity fluctuations above the wall cause increased small-scale near-wall turbulent activity.

## 5.2 Near-wall velocity fields

We present in this section the filtered streamwise velocity fields near both walls, the moving and the stationary wall. We will discuss here the features present in each region of the domain for our different cases. Notice that as in Figure 5.1 we will employ a small domain of size $L_X \times L_Y \times L_Z = 16\pi h \times 2h \times 6\pi h$. Moreover, the filter employed is the same as in Section 5.1, which was previously described in Algorithm 7 in Section 4.6.

In Figure 5.8 the filtered streamwise velocity field near the stationary wall are depicted for each case. Their specific position is $y/h = -0.9178$, as it stays near $y^+ \approx 10$, where we could measure a peak of streamwise fluctuating velocity $u$ in Figure 3.1a. This is also confirmed in Pope [1] or Pirozzoli et al. [3].

We notice that the streamwise velocity fields at $y/h = -0.9178$ are quite similar among cases, when observing the instantaneous cases. All of them show a streaky and meandering pattern along the wall-normal plane. Comparing both kind of structure at pure Poiseuille flow we see that low-speed ones are thinner and longer than high-speed structures. Moreover, after the wholes transition to pure Couette flow, the main difference is that both structures become slightly wider.

This similarity among cases was expected as we could proven a perfect collapse of all velocity fluctuations and Reynolds stress near the stationary wall in Section 3.1. Additionally, in Figure 3.3 we could notice that the shear stress (based on velocity slope) near the stationary wall was not zero in any case. Consequently, streaks in all cases were expected. Therefore, we can proven that the streamwise velocity field remains unaffected by the movement of the opposite wall.

Pirozzoli et al. [3] shows instantaneous velocity fields for cases C00P10, C06P04 and C10P00 at $y/h = -0.96$ employing $Re_\tau \approx 250$ in a box of size $L_X \times L_Y \times L_Z = 12\pi h \times 2h \times 4\pi h$. The authors appreciate a similar streaky pattern. According to the non-dimensional parameter suggested by Lam & Banerjee [30], streaks are present if the ratio of local turbulent kinetic energy production to local viscous dissipation is at least of order unity. So, Pirozzoli et al. [3] estimates that the parameter is around 1.72 in all cases at this position.

Curiously, despite the similarity among cases in instantaneous flows, mean flows show the same tendency as in channel center, which denote the presence of counter-rotating rolls. However, near the stationary wall the presence of these rolls is only clear in cases C08P02 and C10P00, despite we saw in the channel center that the rolls are also present in case C06P04. We can conclude that in case C06P04 rolls are weak in intensity as well as they do not occupy the whole channel height. See in Figures 5.5, 5.8 and 5.10 that rolls extend along the wall-normal dimension in cases C08P02 and C10P00.

In Figure 5.10 instantaneous filtered and mean streamwise velocity fields are depicted near the moving wall, at $y/h = 0.9269$. Notice that there is almost no difference between the instantaneous and mean fields observed near the stationary or the moving wall in pure Poiseuille flow. This is evident as in Poiseuille flow both walls are stationary. See Section 1.3.

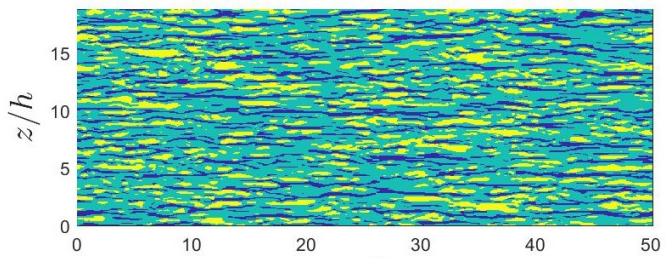


(a) C00P10. Instantaneous

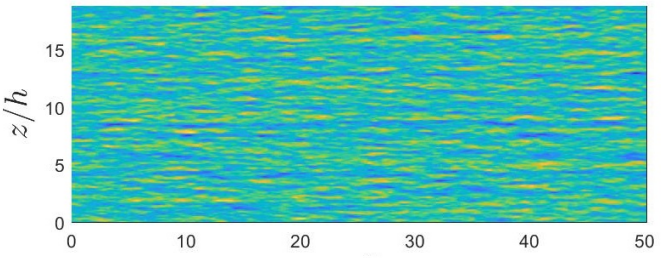


(b) C00P10. Mean

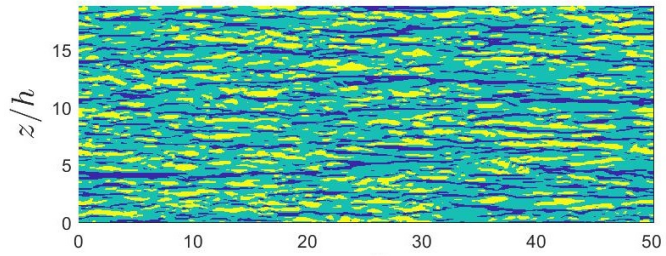


(c) C02P08. Instantaneous

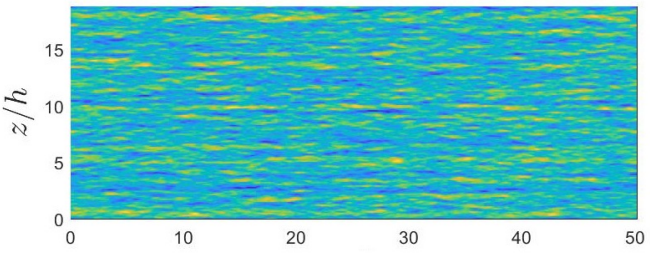


(d) C02P08. Mean

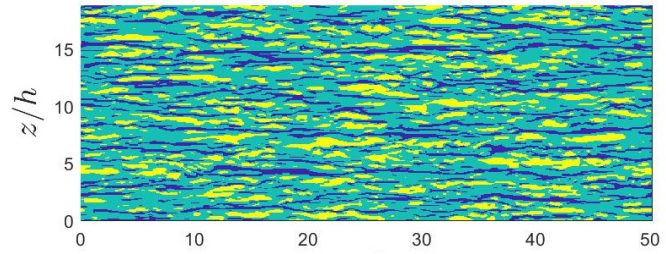


(e) C04P06. Instantaneous

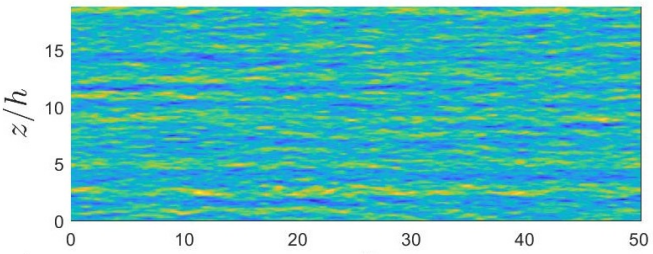


(f) C04P06. Mean

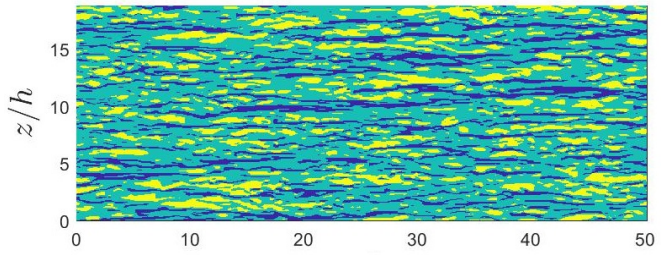


(g) C06P04. Instantaneous

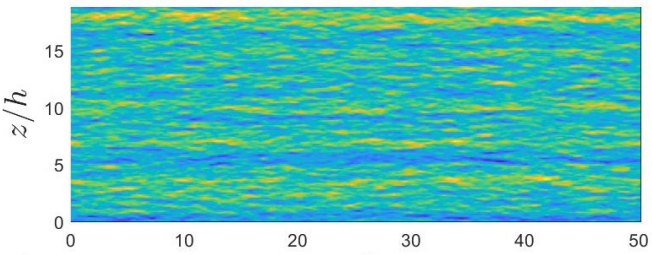


(h) C06P04. Mean

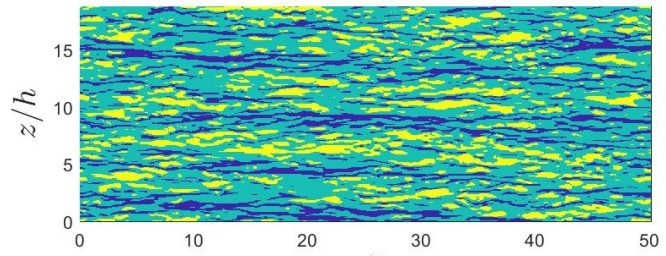


(i) C08P02. Instantaneous

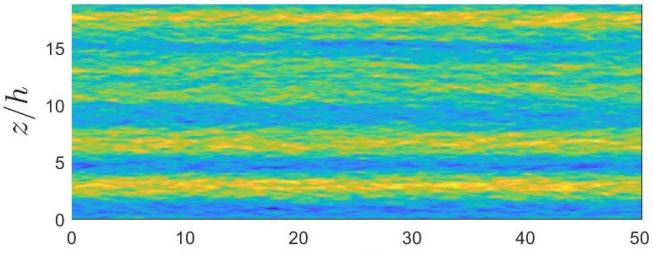


(j) C08P02. Mean

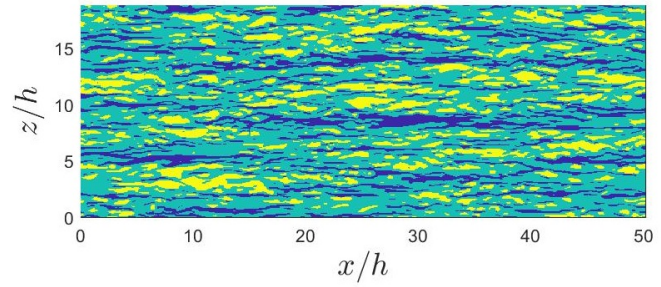


(k) C10P00. Instantaneous

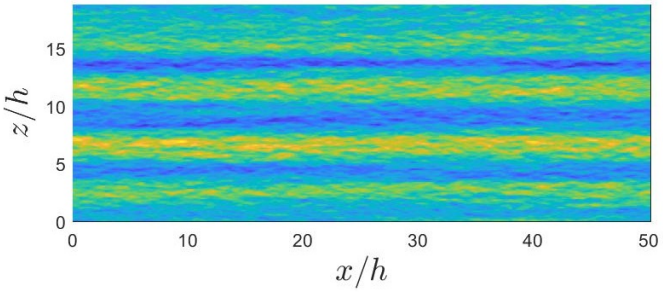


(l) C10P00. Mean

Figure 5.8: Filtered streamwise velocity wall-parallel planes. $y/h = -0.9178$, near stationary wall.

However, the moment that a slight Couette contribution is applied (i.e. C02P08), streamwise fields are different near walls. See that in C02P08 we can distinguish two types of structures: thin and elongated structures characteristic of Poiseuille flows and thick structures from Couette flow in channel core (See Figure 5.1k). This suggestion was also proposed by Pirozzoli et al. [3], who also analysed this fact through a two-points correlation near the moving wall.

Something more interesting occurs in case C04P06, and specially in case C06P04 near the moving wall. We see in Figures 5.10e and 5.10g, that the streaks tend to disappear. Recalling Figure 3.3 and observing each slope near $y/h = 1$; that is, the shear stress, we notice that shear stress is much lower in these cases than the other ones. Hence, as Pirozzoli et al. [3] estimated, the ratio of local turbulent kinetic energy production to local viscous dissipation is near 0.

One may say that this is also the case in the channel center for pure Poiseuille flow; however, there are differences between Figures 5.1a and 5.10g. The dissimilarity arises from the blocking effect of the moving wall in the C06P04 case, as proposed by Pirozzoli et al. [3].

Finally, in cases C08P02 and C10P00 we find a perfect meandering pattern among high-speed structures, while low-speed ones show thicker and shorter streaks. Here we can perfectly see that there are two kind of patterns, and that the meandering ones compare with the ones present at pure Poiseuille flow near the moving wall (Figure 5.10a).

On the other hand, mean streamwise field near the moving wall are not as clear as instantaneous ones. One can only distinguish the presence of counter-rotating rolls from cases C06P04 to C10P00. Notice however that near the stationary wall we could not find these rolls for case C06P04 (See Figure 5.8h).

Finally, for a better understanding of the the ratio of local turbulent kinetic energy production to local viscous dissipation, we have extracted Figure 5.9 from Pirozzoli et al. [3], which shows the distribution of this parameter along wall-normal dimension among different cases. Notice that in Figure 5.9, moving wall is located at $y/h = -1$ and stationary wall at $y/h = 1$.

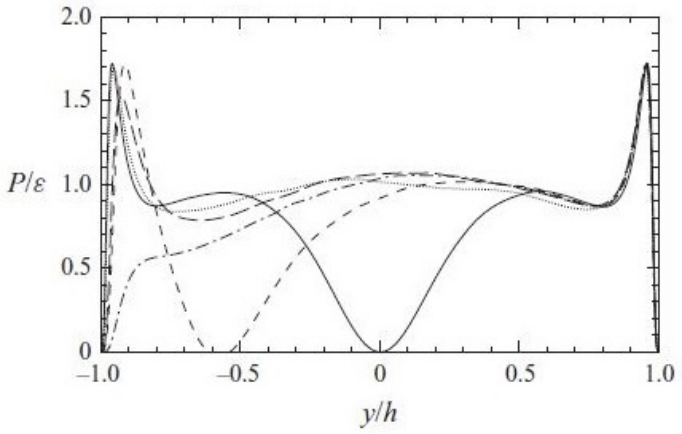


Figure 5.9: Ratio of local turbulent kinetic energy production ($P$) to local viscous dissipation ($\varepsilon$). C00P10 —— ; C02P08 – – – ; C06P04 – · –· ; C08P02 — — ; C10P00 · · ·. Image extracted from [3].

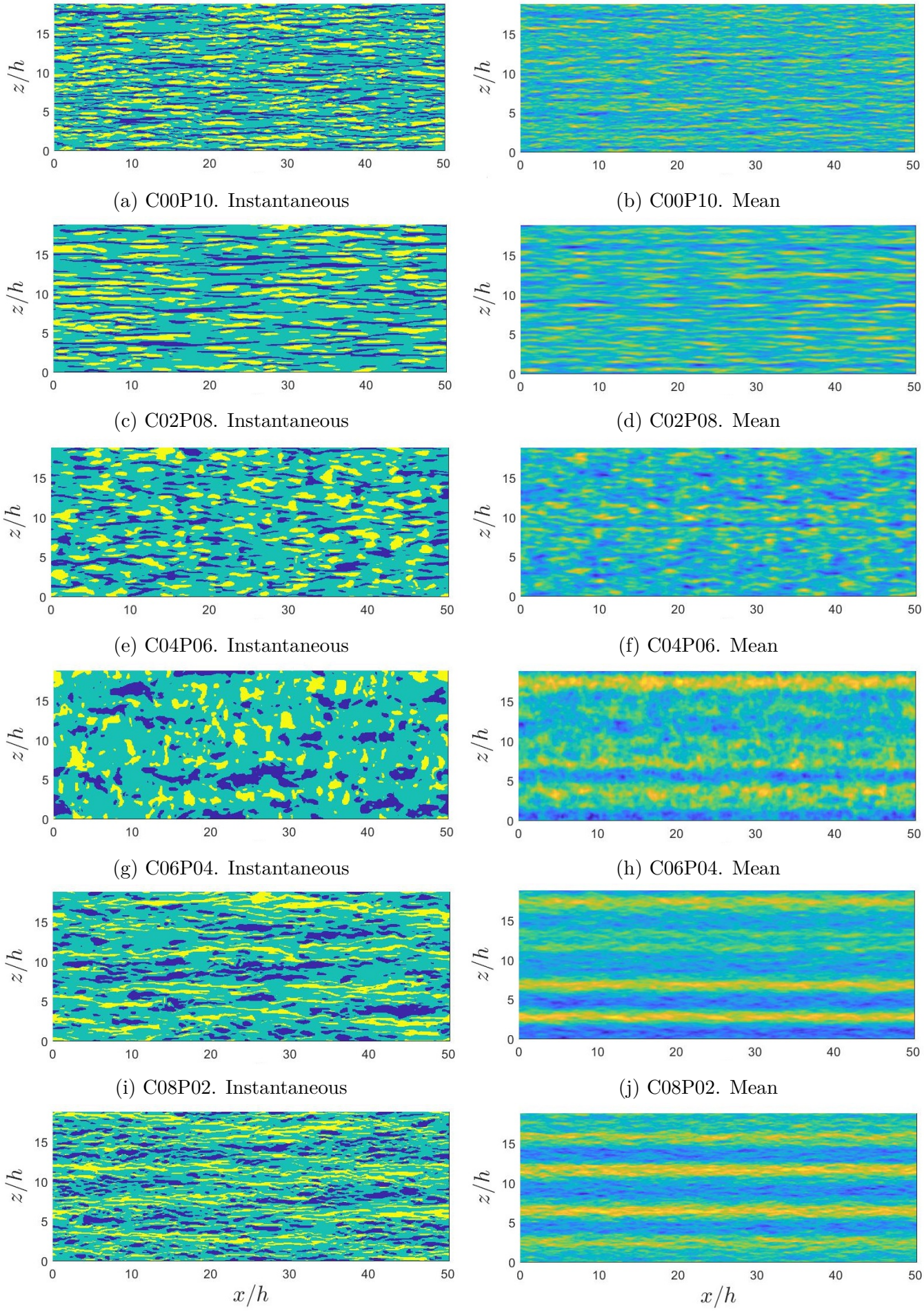


(a) C00P10. Instantaneous

(b) C00P10. Mean

(c) C02P08. Instantaneous

(d) C02P08. Mean

(e) C04P06. Instantaneous

(f) C04P06. Mean

(g) C06P04. Instantaneous

(h) C06P04. Mean

(i) C08P02. Instantaneous

(j) C08P02. Mean

(k) C10P00. Instantaneous

(l) C10P00. Mean

Figure 5.10: Filtered streamwise velocity wall-parallel planes. $y/h = 0.9269$, near moving wall.

## 5.3 Two-points correlation

In previous sections, we could analyse the structures distribution during the transition and in pure Poiseuille flow near both walls. In this section, we are going to measure the rolls size at each case through two-points correlation. Results will be compared with other studies.

Two-points correlation is a mathematical tool commonly employed in the literature in order to find repeating patterns, such as the presence of a periodic signal obscured by noise, or identifying a fundamental frequency.

Two-points correlation of a random process, sometimes known as autocorrelation function, is defined as:

$$R_{ij}\left(r,\, t\right) = \frac{u_i\left(x + r,\, t\right) u_j\left(x,\, t\right)}{\sqrt{u_i^2}\sqrt{u_j^2}} \tag{5.3.1}$$

where $u_i$ is the fluctuating velocity component in $i$-direction, and $r$ is an advancing step in $x$-direction.

The possible values for $R_{ij}$ lie in the range $[-1,\, 1]$, with 1 indicating perfect correlation and $-1$ indicating perfect anti-correlation. Do not confound anti-correlation $(-1)$ with no correlation between values, in which $R_{ij}$ becomes 0.

According to Pope [1] in page 68, notice that a turbulent flow, after an initial transient perior, can reach a statistically stationary state in which, even though the flow variables (i.e. $U\left(t\right)$) vary with time, the statistics are independent of time.

Hence, our two-points correlations are independent of time, and only depend on the advancing step.

Moreover, based on its definition in Eq. 5.3.1, a two-points correlation has the properties:

$$R_{ij}\left(0,\, t\right) = 1 \tag{5.3.2}$$

$$\left|R_{ij}\left(r,\, t\right)\right| \leq 1 \tag{5.3.3}$$

Remind that our principal aim is to extract information on the width and length of the counter-rotating rolls present in Couette-driven cases; that is, case C06P04 until pure Couette. Consequently, among the possible two-points correlations, we are specially interested in $R_{11}$ in streamwise and spanwise directions applied in the channel center. Notice that $R_{11}$ correlates only the streamwise fluctuating velocity term along a given direction. We saw in Section 5.1 that this term defines well the rolls.

The two-point correlation of our simulations along the streamwise direction at $y/h = 0.065$ was published in Gandía-Barberá et al. [23], from where we extracted Figures 5.11a and 5.11b. Notice that both correlations were carried out on the large domain of length $128\pi h$, in order to extract the proper length of the structures.

Additionally, see that both figures fulfil the conditions stated in Eq. 5.3.2 and Eq. 5.3.3.

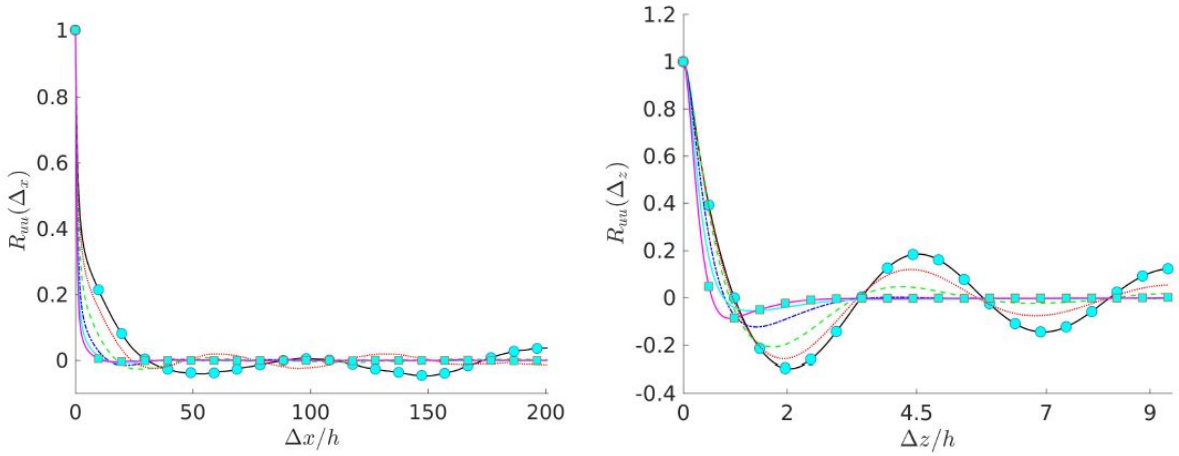


(a) (b)

Figure 5.11: Autocorrelation of $U$ at $y/h = 0.065$ in streamwise (a) and spanwise (b) direction. Lines as in Table 3.1. Images extracted from [23].

The length of the rolls can be gained from Figure 5.11a. The extremely long domain employed shows the second minimum of the correlation for the first time; this could not happen in previous studies such as Pirozzoli et al. [3] or Tsukahara et al. [20]. Hence, the length of the longest structures, which is half of the distance between two consecutive minima of the curve, can be estimated in pure Couette flow as $50h$, approximately.

Notice that the length of these structures gets shorter when the Couette contribution is reduced. This fact could not be seen in the small domain fields depicted in Section 5.1. Finally, the different minima cannot be truly appreciated beyond C06P04, as we also stated from Figure 5.1.

Recalling Figure 5.2, which shows a filtered streamwise velocity field in the center of the large domain, we can estimate that a low- or high-speed structure has an approximate length of $50h$.

Furthermore, in an interesting study M. Lee and Moser [8] performed two-points correlations in a box of length $100\pi h$ for Couette flows at $Re_\tau = 220$ and $Re_\tau = 500$. For the first case, the authors concluded that streamwise oscillations have a wavelength of $25\pi h$; however, they could no extract information from the case at $Re_\tau = 500$, because the second minimum was not present. This fact suggest us that the length of the rolls is highly dependent on the friction Reynolds number of the simulation.

On the other hand, two-points correlation of $U$ in spanwise direction (Figure 5.11b) estimates that the width of the rolls is approximately $2.5h$. This value agrees with the results in Avsarkirov et al. [14], Kraheberger et al. [16], and M. Lee and Moser [8]. However, it differs from Tsukahara et al. [20] and Pirozzoli et al. [3]. These two authors give a smaller value: $1.3h$ and $1.7h$, respectively. The main reason for this discrepancy is the width and length of their domain, which are not sufficient to simulate a full cycle of the rolls.

Additionally, Avsarkirov et al. [14] showed that this spanwise length remained constant for Couette flows from $Re_\tau = 125$ to $Re_\tau = 550$ in a domain of size $L_X \times L_Y \times L_Z =$

$20\pi h \times 2h \times 6\pi h$. This is also confirmed by M. Lee and Moser [8] at $Re_\tau = 500$ in a larger domain. Finally, Kraheberger et al. [16] estimated a similar value of the rolls spanwise length at $Re_\tau = 1000$, without wall transpiration.

Therefore, we can conclude that the spanwise length of the rolls remains independent from friction Reynolds number in the range from $Re_\tau = 125$ to $Re_\tau = 1000$.

## 5.4 Spectral densities

Another mathematical tool for the study of turbulence is the velocity spectra. This tool shows how the velocity structure sizes are distributed. A velocity spectra is based on the Fourier series of the velocity. Hence, if the wavenumber associated to a given length $l$ is $k = 2\pi/l$, streamwise velocity is estimated as:

$$u\left(x\right) = \int_{-\infty}^{\infty} \widehat{u}\left(k\right) e^{ikx} dk \tag{5.4.1}$$

This representation in Fourier series (Eq. 5.4.1) is only valid in homogeneous directions, such as our streamwise and spanwise directions.

Indeed, a Fourier representation makes easier to estimate the energy associated to a given range of scales or wavelengths.

Moreover, Fourier coefficients in Eq. 5.4.1 could be considered as $u$ components in different bases specified by $v^k\left(x\right) = e^{ikx}$, which are orthogonal.

As a consequence, the scalar product between $u$ and the bases $v$ is expressed as the averaged sum of the products of each vector component. This leads us to Perceval theorem:

$$u \cdot v = \left\langle u\left(x\right) \overline{v\left(x\right)} \right\rangle = \frac{2\pi}{L} \int_{-\infty}^{\infty} \widehat{u}\left(k\right) \overline{\widehat{v}\left(k\right)} dk \tag{5.4.2}$$

For the particular case $u = v$, Eq. 5.4.2 represents the mean square of variable $u$. Consequently, if $u$ is a velocity, the term $|\widehat{u}\left(k\right)|^2$ represents the energy spectra, and estimates the energy related to the wavenumber $k$.

However, for representing we are not interested in comparing $k$ with $k+1$, but $10^1\, k$, $10^2\, k$, and so on. Therefore, it is more useful to represent $|\widehat{u}\left(k\right)|^2$ as a function of $\log\left(k\right)$.

This approach makes us lose the main property of an integral; that is, calculate the accumulated energy in a range of wavenumbers as the area enclosed by the $|\widehat{u}\left(k\right)|^2$ curve. Thus, in order to maintain the attribute, we will not represent the original spectra, but the premultiplied spectra $k\,|\widehat{u}\left(k\right)|^2$ as a function of $\log\left(k\right)$:

$$\langle u^2 \rangle = \int_0^{\infty} |\widehat{u}\left(k\right)|^2 dk = \int_0^{\infty} k|\widehat{u}\left(k\right)|^2 d\left(\log k\right) \tag{5.4.3}$$

Through the premultiplied spectra, sometimes referred as velocity spectra, we will estimate which are the wavenumbers that carry the largest amount of energy in our simulations, as other authors have already done; i.e. M. Lee and Moser [8] or Pirozzoli et al. [3].

The streamwise velocity spectra of our simulations in the large domain is depicted in Figure 5.12. Moreover, it was published in Gandía-Barberá et al. [23], from where Figure 5.12 is extracted.

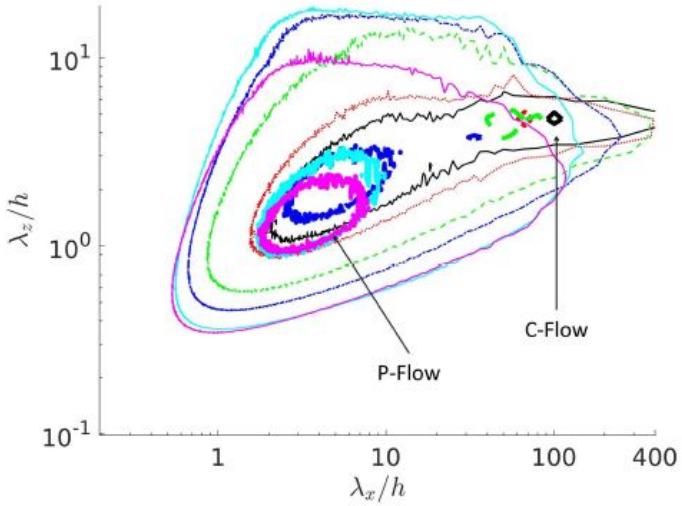


Figure 5.12: Lines as in Table 3.1. Spectral density at $y/h = 0.065$ for $U$. The thin line represents the 10% of the energy maximum and the thick one the 75%. In every case, $L_X = 128\pi h$.

Figure 5.12 shows how the energy is organized among the streamwise (X-axis) and spanwise (Y-axis) wavelengths in each simulation case. Notice that it is much easier to identify the rolls wavelengths in Figure 5.12 than in Figure 5.11, specially for intermediate cases; i.e. C04P06.

By analysing Figure 5.12, we extract similar conclusions about the length and width of the rolls as in Figure 5.11. Notice that the thick line of pure Couette flow is highly concentrated in $\lambda_x/h = 100$ and $\lambda_z/h = 5$. Something similar occurs at C08P02; however, now the energetic region moves to $\lambda_x/h = 70$. At C06P04 these energetic structures are still present, but the region has moved to $\lambda_x/h = 50$, as well as it has expanded.

Case C04P06 also shows a energetic region far from low values of $\lambda_x/h$; nevertheless, the thick line also covers the small wavelengths, which did not happen in previous cases. This energetic region present in C04P06 is similar to the one we find in C02P08 and C00P10. Therefore, we conclude that rolls are no longer present in case C04P06.

It is also relevant to indicate that according to Figure 5.12, Figure 5.11 and streamwise velocity fields in Section 5.1, there is a smooth and stepped transition from the presence of the rolls to the complete disappearance of them. This is an important conclusion we did not expect at the beginning of our study.

On the other hand, M. Lee and Moser [8] showed the premultiplied spectra of $u_i u_j$ along the streamwise and spanwise direction for different Couette flows and for a Poiseuille flow.

The first aspect the authors notice is that the spectra of each Reynolds component $u_i u_j$ close enough to the wall ($y^+ < 60$) and for small wavelengths is the same regardless of Reynolds number and including the Poiseuille flow. This occurs due to the approximate

universality of small-scale near-wall turbulence, as we stated in Section 1.1 for turbulent small-scales.

Furthermore, in streamwise Couette flow spectra at $Re_\tau = 220$ the authors find a strong peak at $\lambda_x/h = 78$ that covers the whole wall-normal dimension of the domain. This is similar to what we could demonstrate in Figure 5.5 or in Figure 5.4. The same occurs in spanwise direction.

The authors also notice that the peaks of $E_{ww}$ in spanwise direction are stronger far from the channel center. This is in accordance with Figure 5.7 at C10P00, where we see that the strongest structures are aligned near both walls.

Finally, the authors also perform this study in a Couette flow at $Re_\tau = 500$. They show that the premultiplied spectra of $u$ along the streamwise direction is distributed across a range of wavenumbers. This differs from the results at $Re_\tau = 220$ and our results at $Re_\tau = 125$. However, authors noticed through two-points correlations that their domain at $Re_\tau = 500$ is not long enough to capture these energetic structures. Thus, their assessments regarding this case cannot be definitive.

It is also relevant to point that M. Lee and Moser [8] could not probe the existence of strong counter-rotating rolls in pure Couette flow at $Re_\tau = 93$.

We will not comment here the pre-multiplied spectra calculated by Pirozzoli et al. [3], because the domain employed is too small to extract information about the most energetic structures in any case. Therefore, what we see in their spectra is only the approximate universality of small-scale near-wall turbulence described by M. Lee and Moser [8]. This fact makes their spectra for pure Poiseuille and pure Couette flows really similar.

# Chapter 6

# Vortex structures and classification

Our last analysis is focused on the characteristics of the vortex structures present in each case. This kind of study is not carried out frequently, in fact among our references only in Kraheberger et al. [16] performed a vortex analysis of several Couette flows at $Re_\tau = 1000$ with different transpiration flow velocities. Also C. Prus [24] performed a vortex analysis on Poiseuille flows, but the author focused primarily on square ducts, and slightly on channel flows.

In this chapter we will first explain our results of the percolation analysis. All the theory behind this analysis as well as the vortex identification method was described in Section 4.2. However, in Section 6.1 we show for each case the mean percolation limit and standard deviation among instantaneous simulations. We will also see the distribution of discriminant standard deviation along the wall-normal direction, as in Figure 4.2 on Section 4.2.

## 6.1 Percolation analysis

Recalling the explanation in Section 4.2, percolation analysis is necessary in order to find the optimal value for the threshold parameter $\alpha$ in vortex identification method, according to Equation 4.2.5. The relevance for this value stems from its influence on the vortex cluster identification. As explained, for near-zero values of $\alpha$, identified cluster would merge until only a single large object remains in the channel. On the contrary, near-one values of $\alpha$ would lead the method to identify few small clusters, which would be dispersed in the channel. For detailed information, the interested reader is referred to Del Alamo et al. [26].

This explanation is quite comprehensible by observing Equation 4.2.5. For near-zero values of $\alpha$, the threshold becomes zero; which is a poor filter in Galilean invariant vortex identification techniques, as stated by Chakraborty et al. [25]. For large values of $\alpha$, the threshold becomes highly restrictive; thus, the scheme identifies just few vortex points.

No more explanation will be given about the percolation analysis steps as they were previously described in Section 4.2.

The mean optimal value for $\alpha$ at each simulation case is presented in Table 6.1 as variable $\alpha_{opt}$. We also found interesting to add in Table 6.1 the standard deviation of the optimal $\alpha$'s obtained in each instantaneous simulation of a given case. Standard deviation is defined as variable $\left(\overline{\alpha^2}\right)^{1/2}$. According to a normal distribution, by adding and subtracting the deviation to the mean value one can estimate with a probability of approximately 70% where the correct value of $\alpha_{opt}$ is. These limits are also described in Table 6.1.

| Case | $\alpha_{opt} - \left(\overline{\alpha^2}\right)^{1/2}$ | $\alpha_{opt}$ | $\alpha_{opt} + \left(\overline{\alpha^2}\right)^{1/2}$ | $\left(\overline{\alpha^2}\right)^{1/2}$ |
|---|---|---|---|---|
| C00P10 | 0.0070 | 0.0086 | 0.0103 | 0.0016 |
| C01P09 | 0.0060 | 0.0075 | 0.0090 | 0.0015 |
| C02P08 | 0.0063 | 0.0079 | 0.0095 | 0.0016 |
| C03P07 | 0.0064 | 0.0080 | 0.0096 | 0.0016 |
| C04P06 | 0.0056 | 0.0077 | 0.0098 | 0.0021 |
| C05P05 | 0.0061 | 0.0081 | 0.0100 | 0.0019 |
| C06P04 | 0.0057 | 0.0076 | 0.0095 | 0.0019 |
| C07P03 | 0.0069 | 0.0088 | 0.0107 | 0.0019 |
| C08P02 | 0.0075 | 0.0094 | 0.0112 | 0.0018 |
| C09P01 | 0.0089 | 0.0105 | 0.0121 | 0.0016 |
| C10P00 | 0.0094 | 0.0109 | 0.0125 | 0.0016 |

Table 6.1: Mean optimal percolation limit at each case, as $\alpha_{opt}$. Standard deviation among instantaneous results is presented as $\left(\overline{\alpha^2}\right)^{1/2}$. By subtracting and adding the deviation to the mean value, the range of $\alpha_{opt}$ is estimated with 70% of probability.

By comparing our optimal percolation limit at pure Poiseuille flow in Table 6.1 with the value obtained by Del Alamo et al. [26], we see that the difference is negligible. Notice that the authors employ the same value for all their simulation cases at $185 \leq Re_\tau \leq 1901$. Additionally, we see that all our results are in the same order as the one estimated by the authors. Regarding the analysis of C. Prus [24], we can not compare our results because the author employs a different vortex identification method, so the author does not calculate the discriminant $\Delta$.

Finally, the study of Kraheberger et al. [16] employed a constant threshold, so Equation 4.2.5 does not apply. As a consequence, their distribution of vortices along the wall-normal direction is more abundant near the walls. This is not our case due to employing a variable threshold. Following Kraheberger et al. [16], in Figure 6.1 we have plotted the mean percentage of identified vortices along the wall-normal direction for our

analysis cases. This defined by parameter $\phi(y)$, which is described in Equation 6.1.1.

$$\phi(y) = \sum_x \sum_z H(x,\, z,\, y) \cdot \frac{100}{N_X\, N_Z} \tag{6.1.1}$$

In this equation, $H(x,\, z,\, y)$ is the Chong matrix, explained in Section 4.2.

Notice that in Figure 6.1a the percentage of vortices along the wall-normal direction in C10P00 remains constant around 8% across the channel in our study. This differs from the $\phi(y)$ distribution of a Couette flow in Kraheberger et al. [16], obtained through a constant threshold. Regarding the other cases, all of them remain in a range between 5% and 12%, despite case C04P06 which shows a peak of 16% near the moving wall.

It is relevant to see in Figure 6.1a that case C06P04 shows a clear decrease of vortex population near the moving wall. We saw previously in Table 3.1 or in Figure 3.3, that this case has a very low shear stress near the moving wall, hence its friction Reynolds number stays around $Re_\tau \approx 13$. In this region we assume that the flow is laminar.

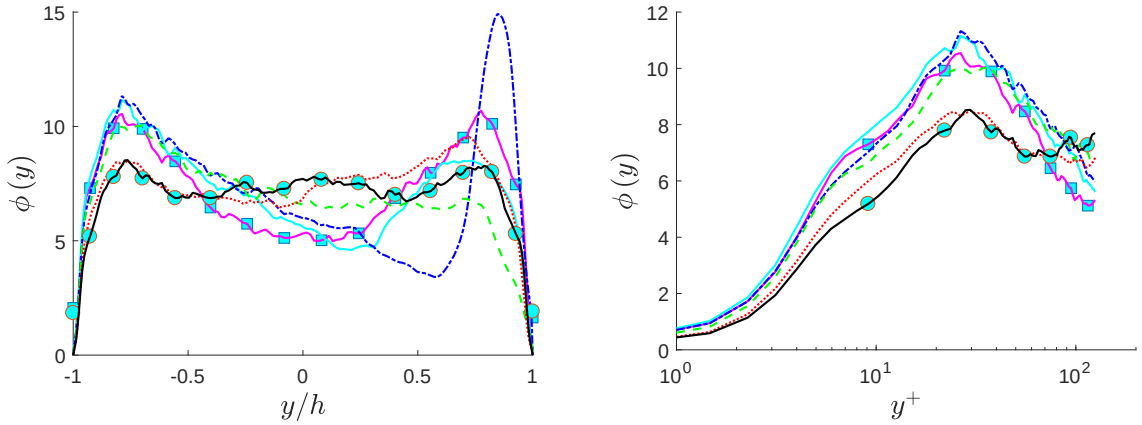


Figure 6.1: Lines as in Table 3.1. Percentage of points where Chong identification method was positive depicted along (a) $y/h$, (b) $y^+$. For each case its corresponding $\alpha_{opt}$ presented in Table 6.1 was employed.

Furthermore, it is also interesting to depict the standard deviation of the discriminant $\Delta$ averaged among the instantaneous simulations of a given case. This distribution shows how the variable threshold changes along the wall-normal direction from pure Poiseuille flow to pure Couette.

In Figure 6.2a, we appreciate this distribution along $y/h$. Notice also that only cases C00P10 and C10P00 show an evident symmetry. The remaining cases show values of $\Delta$ almost negligible near the moving wall; curiously all of them are transition cases. Previous authors have not commented this fact in their studies, as none of them conducted a percolation analysis along a stepped transition from Poiseuille to Couette flow.

However, by comparing Figure 6.2a with Figure 6.1a, we notice that despite the variable threshold decreases notably near the moving wall, the percentage of vortex identified in this region for transition cases remains constant.

In Figure 6.2b, the same distribution is depicted in wall-units near the stationary wall. We see a similar behaviour as the one depicted in Figure 4.2, and described by Del Alamo et al. [26]. See that in all cases the standard deviation has a peak near $y^+ \approx 10$; that is, the threshold of the identification method becomes more restrictive in this region. Recalling Figure 3.1a and Figure 5.9, we notice both peaks of fluctuating streamwise component $u'$ and turbulent production near $y^+ \approx 10$; therefore, it is comprehensive to find a numerous amount of vortex points.

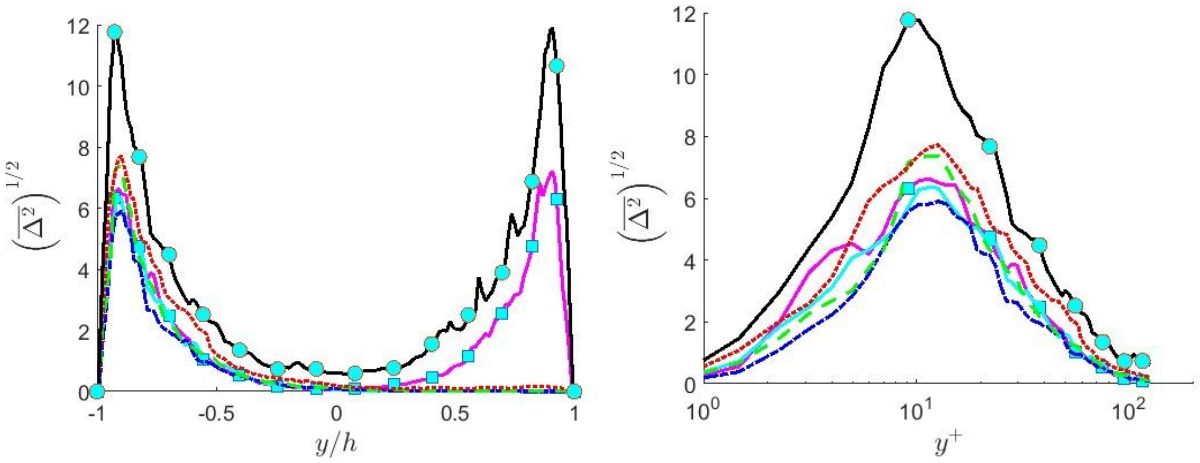


(a) (b)

Figure 6.2: Lines as in Table 3.1. Distribution of the standard deviation of discriminant $\Delta$ along the wall-normal direction depicted along (a) $y/h$, (b) $y^+$.

By observing the vortex distribution parameter $\phi(y)$ in Kraheberger et al. [16], we see that a constant threshold identifies a larger amount of vortices near both walls than in the channel center, for a pure Couette flow. Applying a variable threshold depending on wall distance as specified by Del Alamo et al. [26], the threshold becomes more restrictive near the walls at pure C- and P- flows, and remains less restrictive in the channel center. Hence, we ensure that near-wall vortices do not influence our measures in the channel center, which is more important in our study.

Finally, Kraheberger et al. [16] proposes the integral of $\phi(y)$ for estimating the part of volume of the channel where vortical structures exists. Following this statement, we have performed a numerical integration of $\phi(y)$ according to Simpsons rule. See Equation 6.1.2.

$$V_\phi = \int_{-h}^{h} \phi(y)\, dy \approx \sum_{i=1}^{N_Y-2} \int_{h_i}^{h_{i+2}} \phi(y)\, dy = \sum_{i=1}^{N_Y-2} \frac{h_{i+2}-h_i}{6} \cdot \left(\phi(h_i) + 4\,\phi(h_{i+1}) + \phi(h_{i+2})\right) \tag{6.1.2}$$

For the cases depicted in Figure 6.1 and Figure 6.2, we have estimated the volume percentage $V_\phi$ presented in Table 6.2. Recalling the value estimated by Kraheberger et al. [16] for a pure Couette flow, the authors state $V_\phi = 34.25$. This value is similar to our result at C10P00. Hence, we conclude that the variable threshold adapts itself to decrease the identified vortex population near walls, but at the same time it increases

this population in the channel center. That is why despite observing strong peaks in $\phi$ at Kraheberger et al. [16], their value of $V_\phi$ remains similar to ours.

Finally, volume percentage $V_\phi$ remains in the same order at all cases. This is in accordance with the depicted distribution of $\phi$ in Figure 6.1. Notice that the minimum value of $V_\phi$ appears in case C06P04 due to its low shear stress near the moving wall.

| Case | C00P10 | C02P08 | C04P06 | C06P04 | C08P02 | C10P00 |
|---|---|---|---|---|---|---|
| $V_\phi$ (%) | 28.626 | 28.435 | 28.811 | 27.616 | 29.058 | 28.126 |

Table 6.2: Percentage of volume occupied by vortices at each case. For each case its corresponding $\alpha_{opt}$ presented in Table 6.1 was employed.

Once presented the results of our percolation analysis, and compared them with the results after employing a constant threshold in a pure Couette flow, we are going to show the vortex distributions at diverse wall-parallel planes. Additionally, these planes will be compared with the streamwise velocity wall-parallel planes explained in Section 5.1.

## 6.2 Vortex distribution along wall-parallel planes

In this section the distribution of vortices in wall-parallel planes at diverse distances from the wall are presented. Then, the distributions will be analysed using statistical methods in order to extract relevant conclusions. In this process, the vortex volumes around three regions will be calculated among cases, and later their Probability Distribution Function (PFD) compared.

In Figure 6.3 diverse wall-parallel planes of a Chong identification matrix are depicted near the stationary wall at $y/h = -0.9178$, as well as near the moving wall at $y/h = 0.9269$. The yellow points denote vortex points, where the value of the identification matrix is 1. On the contrary, in the blue region no vortex was detected by the Chong method.

Among the wall-parallel planes near the stationary wall there is a notorious similarity. All cases show vortex clusters following a streaky pattern. The similarity among cases in this domain region was previously observed in the instantaneous streamwise velocity fields in Figure 5.8. Moreover, other magnitudes, such as the mean streamwise velocity profile (Figure 3.3), the Reynolds stress (Figure 3.2b) and the velocity fluctuating components (Figure 3.1 and Figure 3.2a) show a great similarity in this near-wall region around $y^+ \approx 10$.

On the contrary, the wall-parallel planes near the moving wall do not show a streaky pattern in cases C04P06 and C06P04. In these cases vortices are gathered in thicker and compact clusters, which decrease notably in case C06P04. As commented before, case C06P04 has a very poor friction Reynolds stress in these region. Additionally, both commented cases described the same tendency in their instantaneous streamwise velocity fields in Figure 5.10.

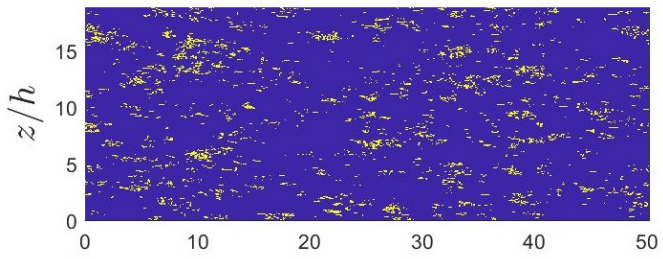


(a) C00P10. Stationary wall

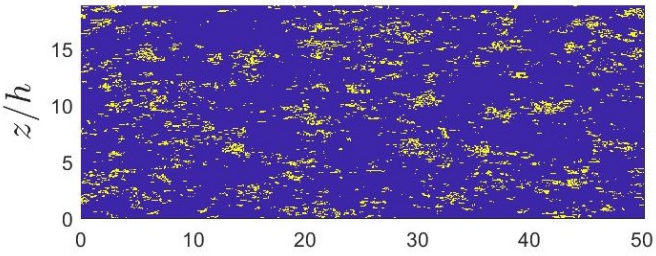


(b) C00P10. Moving wall

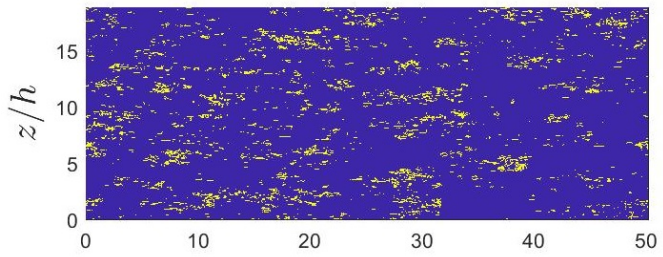


(c) C02P08. Stationary wall

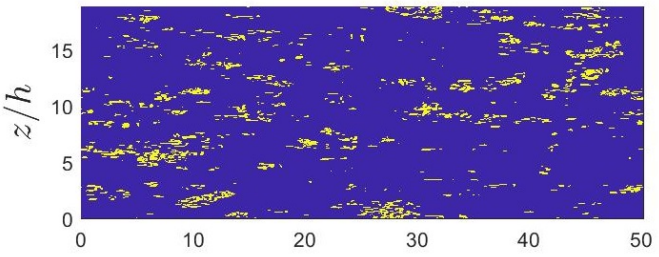


(d) C02P08. Moving wall

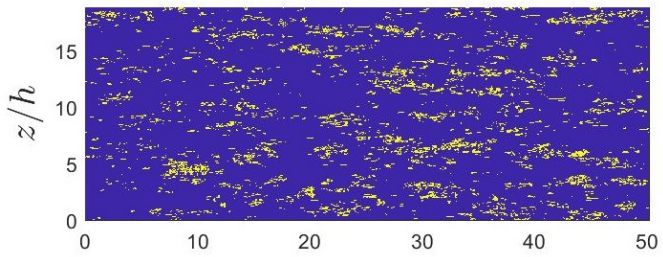


(e) C04P06. Stationary wall

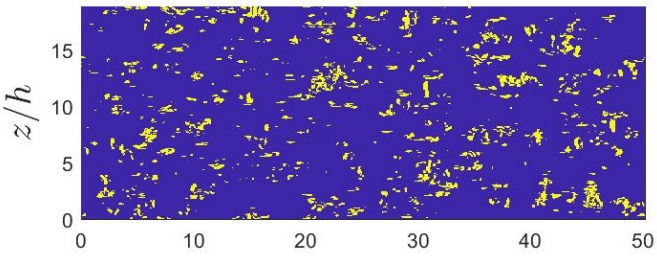


(f) C04P06. Moving wall

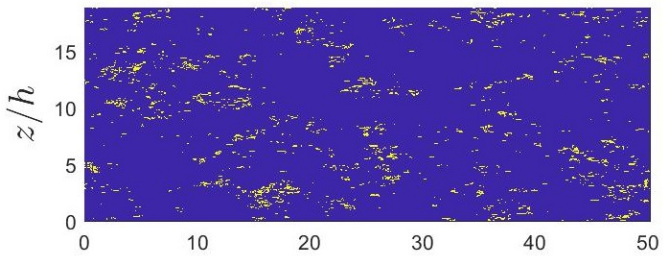


(g) C06P04. Stationary wall

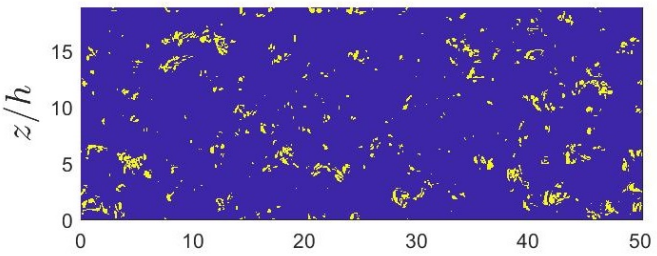


(h) C06P04. Moving wall

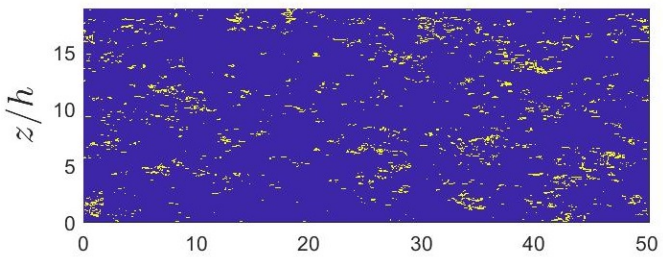


(i) C08P02. Stationary wall

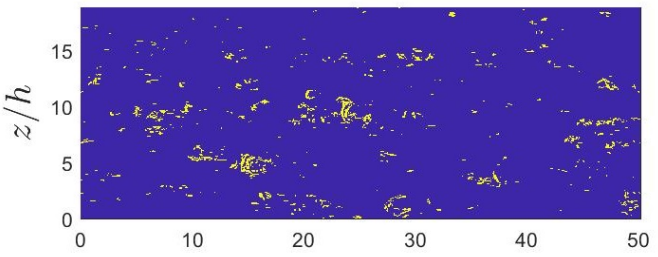


(j) C08P02. Moving wall

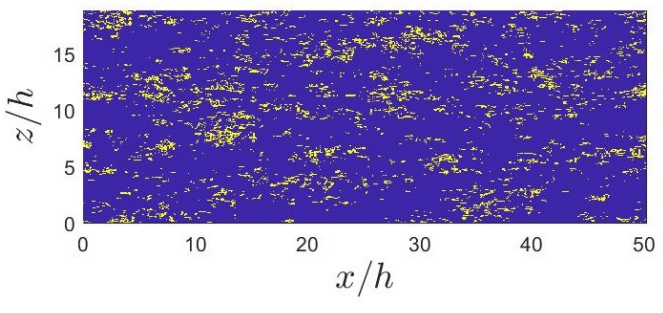


(k) C10P00. Stationary wall

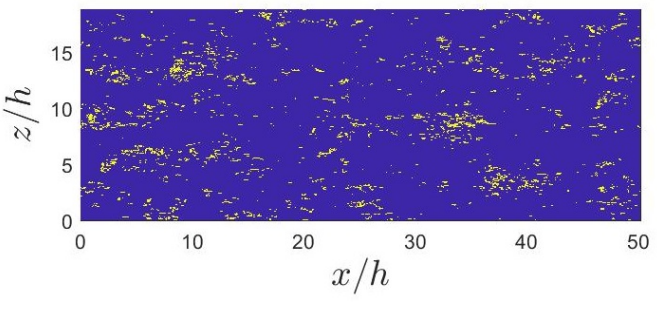


(l) C10P00. Moving wall

Figure 6.3: Chong matrix wall-parallel planes near the stationary wall (left) at $y/h = -0.9178$, and near the moving wall (right) at $y/h = 0.9269$.

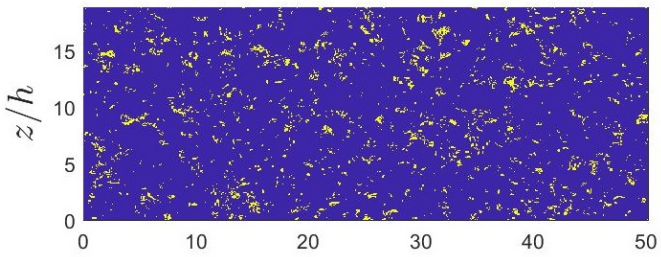


(a) C00P10. Channel center

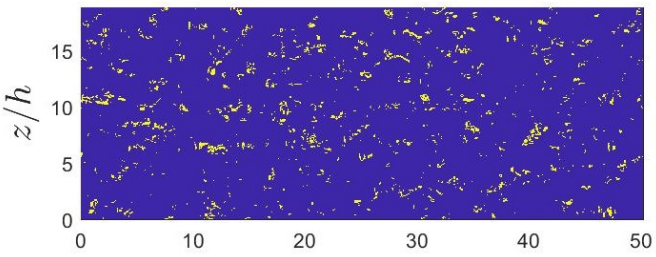


(b) C02P08. Channel center

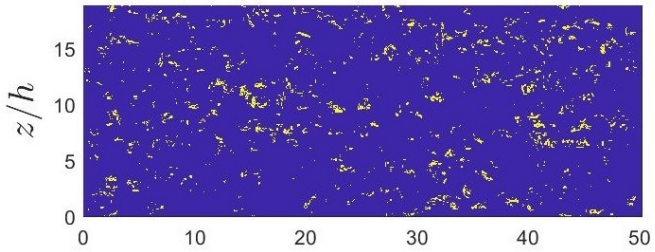


(c) C04P06. Channel center

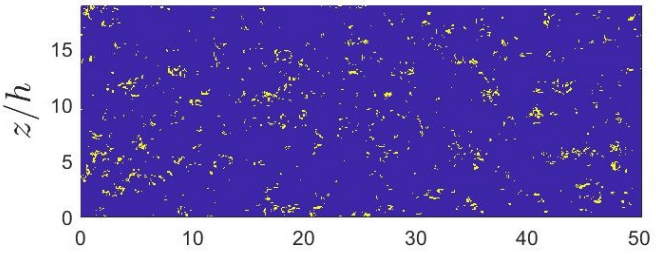


(d) C06P04. Channel center

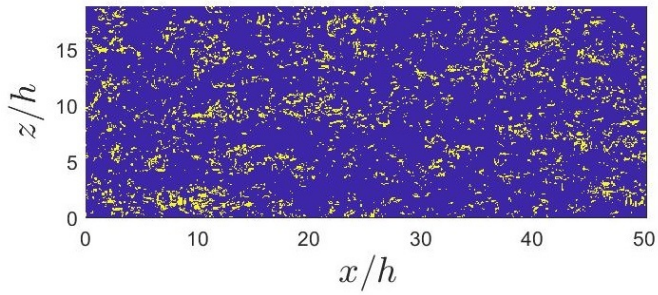


(e) C08P02. Channel center

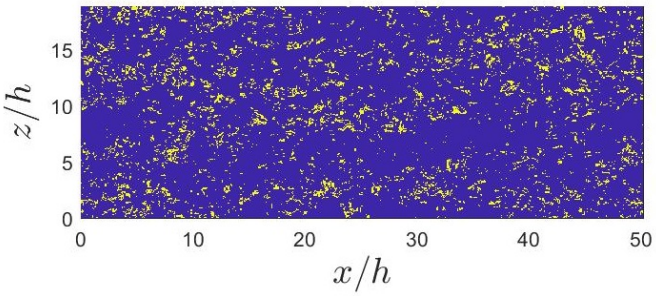


(f) C10P00. Channel center

Figure 6.4: Chong matrix wall-parallel planes in the channel center at $y/h = 0.065$.

Finally, wall-parallel planes at the channel center are depicted in Figure 6.4. See that the vortex population increases in cases C08P02 and C10P00 in this region. Remind that in Section 5.1 the presence of large counter-rotating rolls was demonstrated in these cases. It may be a relation between these structure and the increase of vortex clusters in the channel center. However, notice that more vortices in pure Poiseuille case were detected than in transition cases.

As one can see, a visual analysis of Figure 6.3 and Figure 6.4 is not optimal, as few conclusions can be extracted. Therefore, the next step is to perform a statistical analysis of the volume of the vortices present in the regions depicted. All volumes were estimated using Algorithm 3 and 4, described in Section 4.5. Two-dimensional approaches were considered, such as measuring stream- and spanwise dimensions at the presented planes, or measuring vortex areas, however the results could not shed light on vortex tendencies in these regions.

The regions were arbitrarily described according to the following wall-distances, where subscript $s$ denotes from stationary wall, and $m$ from moving wall.

- Near stationary wall: from $y_s^+ \approx 1$ to $y_s^+ \approx 20$.
- Channel center: from $y/h \approx -0.25$ to $y/h \approx 0.25$.
- Near moving wall: from $y_m^+ \approx 1$ to $y_m^+ \approx 20$.

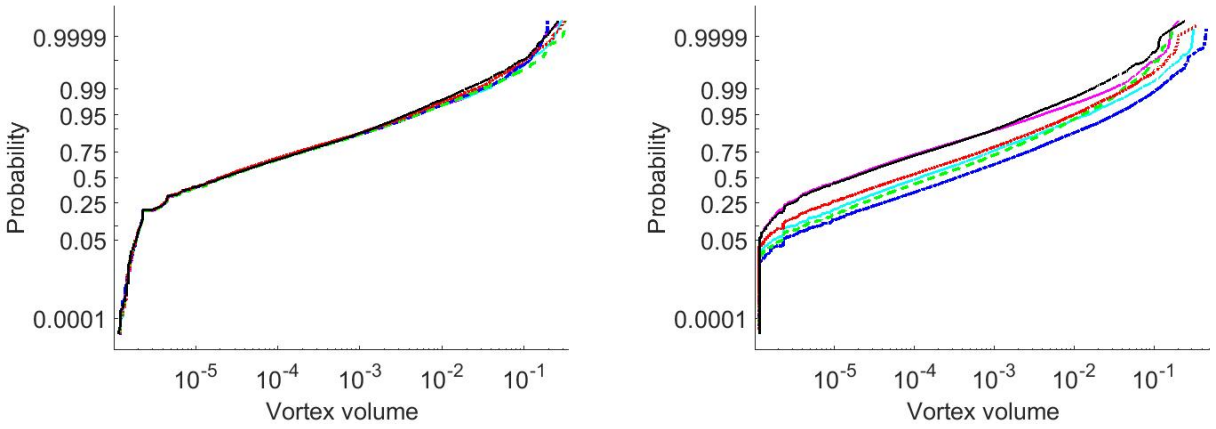


Figure 6.5: Lines as in Table 3.1. Probability plot of vortex volumes (a) near the stationary wall, and (b) near the moving wall. For each case its corresponding $\alpha_{opt}$ presented in Table 6.1 was employed.

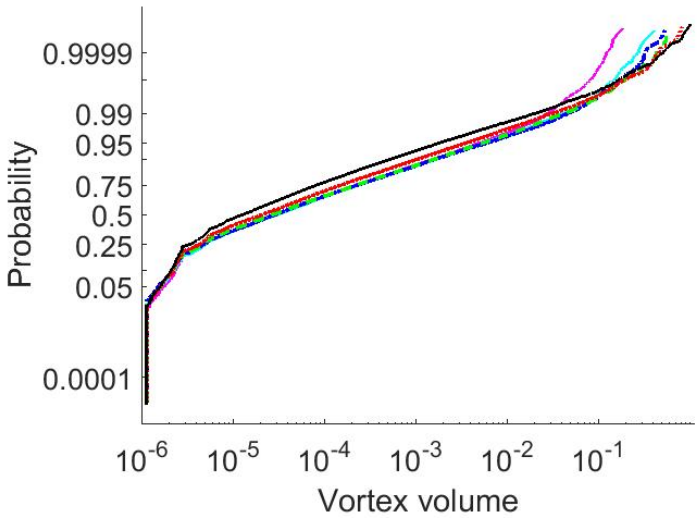


Figure 6.6: Lines as in Table 3.1. Probability plot of vortex volumes in the channel center region. For each case its corresponding $\alpha_{opt}$ presented in Table 6.1 was employed.

For all distributions, the vortex volumes in the regions previously described were extracted from twelve instantaneous cases. All Figures use a *Lognormal* distribution. In Figure 6.5a the probability plot in the region near the stationary wall is depicted. Notice a perfect collapse among all simulation cases. Hence, in this region we see that the vortex volumes follow the same distribution independently of the case. Even the biggest volumes present remain in the same range, around $10^{-1}h^3$.

This result stays in accordance with the similarity of the streamwise velocity structures in this region, as seen in Figure 5.8. Therefore, Figure 6.5a denotes a link between the vortex volumes and the streamwise velocity structures.

Distributions near the moving wall in Figure 6.5b only achieve a good collapse in pure Couette and Poiseuille flows. However, transition cases show bigger vortex clusters in this region in comparison with pure cases, specially in case C04P06. See that the largest scales in case C04P06 are four times bigger than in pure cases. Recalling the streamwise velocity fields near the moving wall, depicted in Figure 5.10, one can see that case C04P06 shows a clear different pattern, in which the structures are more compact and thicker. Nevertheless, in the remaining cases a streaky pattern is defined, which develops elongated and thin structures. This is specially notorious in pure cases.

Moreover, we saw in Figure 6.1a that case C06P04 has a reduced vortex population near the moving wall. This was also observed in the measures gathered, which are 50% less than other cases.

Therefore, by comparing Figure 6.5b with Figure 5.10, one can understand why pure cases have vortices with less volume than in transition cases.

Before analysing the channel center, see in Figure 6.5 that most of the probability is related to small volumes in all cases. According to the volume data from Algorithm 3, each vortex cluster introduces one volume value; hence, many small vortex clusters were identified in all cases, which develop a great probability around them. On the contrary, a large cluster, if present, only introduces one value; therefore, despite it is relevant for the study, the graphics show that its probability is pretty low. One must bear this in mind, in order to not neglect large volume values present at very low probabilities.

Furthermore, in order to check if the small clusters population was an effect of the selected optimal percolation limit (See Table 6.1), the same volume analysis was performed employing a more restrictive threshold; that is, 1.7 times $\alpha_{opt}$. However, the results that are not presented here, showed the same distributions for all cases and regions.

The vortex volume distribution in the channel center is presented in Figure 6.6. Here a good collapse is achieved until a vortex volume equal to $0.04h^3$. This fact indicates that the channel center has also a great population of small vortices. However, it is more interesting to observe the results in Figure 6.6 once the collapse is lost. Pure Poiseuille flow reaches all the probability in a region near $0.1h^3$. Then, each transition case in a stepped way reaches higher volumes in the channel center. And finally, cases C08P02 and C10P00 collapse at the end of the curves in a region around $h^3$.

By comparing Figure 6.6 with the instantaneous streamwise velocity structures in the channel center, depicted in Figure 5.1, one notice that the size of the structures increase gradually from pure Poiseuille to pure Couette flow. This is also the result observed in the vortex volume probability.

As a conclusion, statistical distributions of vortex volumes in diverse domain regions following a stepped transition from P- to C- flow are presented for the first time. A link between the vortex volumes and the two-dimensional representations of the instantaneous streamwise velocity structures is observed. As described by velocity magnitudes and Reynolds stress, the region near the stationary wall remains unaffected by the type of flow simulated. However, this is not the case near the moving wall as observed in Figure 5.10 and Figure 6.5b. This idea is also supported by Pirozzoli et al. [3]. Finally, in the channel center the volume of the largest clusters grow gradually in accordance with the Couette contribution, increasing one order of magnitude from P-flow as soon as the very large counter-rotating rolls are present in the flow.

Notice that wall-parallel vortex distributions in these regions (Figures 6.3 and 6.4) were not useful at all, as they showed similar scenarios among the cases in a given region. Additionally, they could not describe the volume patterns.

## 6.3 Flow properties on vortex clusters

In this section diverse flow parameters are analysed on vortex clusters, in order to find any tendency present. For the regions presented in Section 6.2, in each wall-parallel plane each flow parameter (i.e. positive Reynolds stress) values are only considered on vortex points. Then, these points are gathered into clusters, and their position is compared with the filtered instantaneous streamwise velocity structures. The filter is the standard deviation. Therefore, any tendency regarding the position of the vortices will be observed. Additionally, in order to obtain an accurate result, instead of counting number of clusters, their area is classified. The classification is done by observing which kind of regions the vortex touches. According to the three filtered regions, the classification is:

- H: high-speed structure.
- L: low-speed structure.
- N: neutral region.
- HN: high-speed and neutral region.
- NL: neutral region and low-speed structure.
- HNL: all regions touched.

For obtaining the results in this section, Algorithm 5 and its local functions described in Section 4.6 were employed. The classified parameters are the Reynolds stress and the vorticity components $\vec{\omega}$.

In the channel center, Table 6.3 shows a greater amount of classified vortex area than near the walls. As seen in Figure 6.1, the presence of vortices decrease in the near-wall positions.

Notice a greater presence of vortices with positive Reynolds stress, specially in cases where the counter-rotating rolls are not present. Recalling Figure 3.2b, see that the mean Reynolds stress has positive regions in the channel center for Poiseuille dominant cases. The presence of negative Reynolds stress in vortices increases in Couette like flows; however, there is not a clear difference. Consequently, we propose a more conservative threshold for $\langle uv \rangle$.

It is relevant to indicate that in Table 6.3 most of the vortices in all classifications are rarely located on regions of high- (H) or low-speed (L) structures. According to the classification, they are usually located on regions where a neutral zone (N) is present; that is, on the transition between high- and low speed regions.

Regarding the distribution of the vorticity components, $\omega_x$ and $\omega_y$ follow the same tendency among the different cases, in which they tend to be located in neutral zones. In this case, it seems that region NL is predominant.

On the contrary, vorticity component $\omega_z$ shows an equilibrated pattern in case C00P10, but as soon as a Couette contribution is present, negative $\omega_z$ vortices are much more predominant. Recalling the definition of $\omega_z$ as $\omega_z = \partial v/\partial x - \partial u/\partial y$, a negative vorticity means that the wall-normal derivative of $u$ is larger than the streamwise derivative of $v$. In Figure 3.3 one can see how the pure Poiseuille flow achieves a maximum of $U$ in the channel center, while transition and pure Couette cases have a constant increase of $U$ in this region. Hence, one can expect that in channel center the tendency is to achieve negative values of $\omega_z$.

Table 6.4 presents the vortex area classification in the region near the stationary wall. As we could observe in previous analysis in Section 3.1 and Section 5.2, the flow conditions in this region remain little affected by the type of flow simulated. See consequently how the same tendencies and similar values are achieved in each classification among the diverse cases. Here, as well as in the channel center, we see that vortices tend to be located where a neutral region is present.

Regarding the Reynolds stress classification, vortices with positive values are usually located on NL zones, while vortices with negatives values tend to HN zones. As NL regions denote fluctuating $u < 0$, and HN regions $u > 0$, this tendency indicates that near the stationary wall, the fluctuating $v$ is lower than 0.

The vorticity components $\omega_x$ and $\omega_y$ follow a similar trend as in the channel center. However, component $\omega_z$ shows a prevailing negative distribution. Recalling the explanation for this fact, Figure 3.3 shows even a greater wall-parallel derivative of $u$ in this region, and similar among cases. Moreover, we could observe in Figure 5.8 that the instantaneous structures near the stationary wall show a clear thin and streaky pattern; hence, great vortices of negative $\omega_z$ will touch all kind of regions, so HNL predominates.

Table 6.5 presents the vortex area classification near the moving wall. It was observed in previous Section 3.1 and Section 5.2 that the flow conditions in this region are highly dependent on the flow simulated. Recalling Figure 6.1a, see that case C04P06 shows a vortex peak near the moving wall, while case C06P04 shows a decrease in vortex population. As a result, a greater amount of area is classified in case C04P06, and the opposite occurs in case C06P04.

Regarding the Reynolds stress classification, the pattern previously observed near the stationary wall is lost. However, the vortices still tend to occupy neutral regions.

Notice that both vorticity components $\omega_x$ and $\omega_y$ describe separately the same distribution in their positive and negative values. However, $\omega_z$ shows a curious pattern, in which positive values have a larger area from pure Poiseuille until case C04P06. Then, the opposite occurs. See that the transition takes place when the counter-rotating rolls appear in the flow; that is, case C06P04 as described in Section 5.1.

Once again in Figure 3.3, observe that the cases in which positive $\omega_z$ predominates, the slope of $U$ becomes negative; that is, the wall-parallel derivative of $U$. On the other hand, from C06P04 to C10P00 the slope is positive, which also develops a positive $\omega_z$.

| Parameter | C00P10 | | | | | | C02P08 | | | | | |
|---|---|---|---|---|---|---|---|---|---|---|---|---|
| | H | L | N | HN | NL | HNL | H | L | N | HN | NL | HNL |
| $\langle uv \rangle > 0$ | 0.281 | 0.256 | 1.820 | 1.195 | 2.186 | 1.083 | 0.301 | 0.281 | 2.680 | 2.017 | 4.273 | 2.506 |
| $\langle uv \rangle < 0$ | 0.345 | 0.229 | 1.916 | 1.519 | 1.909 | 0.915 | 0.242 | 0.229 | 1.711 | 1.017 | 1.478 | 0.404 |
| $\omega_x > 0$ | 0.323 | 0.243 | 2.046 | 1.532 | 2.281 | 0.916 | 0.277 | 0.286 | 2.338 | 1.712 | 3.149 | 1.358 |
| $\omega_x < 0$ | 0.332 | 0.249 | 1.979 | 1.494 | 2.233 | 0.947 | 0.292 | 0.250 | 2.324 | 1.821 | 3.114 | 1.412 |
| $\omega_y > 0$ | 0.348 | 0.270 | 2.113 | 1.421 | 2.044 | 0.681 | 0.310 | 0.306 | 2.487 | 1.633 | 2.894 | 1.028 |
| $\omega_y < 0$ | 0.355 | 0.271 | 2.110 | 1.412 | 2.019 | 0.616 | 0.311 | 0.280 | 2.446 | 1.641 | 2.934 | 0.972 |
| $\omega_z > 0$ | 0.335 | 0.225 | 1.956 | 1.681 | 2.107 | 1.120 | 0.226 | 0.200 | 1.686 | 1.097 | 1.754 | 0.562 |
| $\omega_z < 0$ | 0.291 | 0.247 | 1.921 | 1.333 | 2.359 | 1.168 | 0.335 | 0.306 | 2.830 | 2.215 | 4.509 | 2.813 |
| Parameter | C04P06 | | | | | | C06P04 | | | | | |
| | H | L | N | HN | NL | HNL | H | L | N | HN | NL | HNL |
| $\langle uv \rangle > 0$ | 0.329 | 0.356 | 2.991 | 2.183 | 5.204 | 2.699 | 0.319 | 0.392 | 3.021 | 1.806 | 4.941 | 2.122 |
| $\langle uv \rangle < 0$ | 0.247 | 0.264 | 1.796 | 0.926 | 1.726 | 0.427 | 0.257 | 0.264 | 1.831 | 0.911 | 1.702 | 0.419 |
| $\omega_x > 0$ | 0.300 | 0.304 | 2.550 | 1.781 | 3.828 | 1.516 | 0.278 | 0.314 | 2.624 | 1.554 | 3.790 | 1.279 |
| $\omega_x < 0$ | 0.298 | 0.313 | 2.570 | 1.807 | 3.797 | 1.481 | 0.317 | 0.346 | 2.510 | 1.552 | 3.539 | 1.205 |
| $\omega_y > 0$ | 0.321 | 0.358 | 2.689 | 1.735 | 3.540 | 1.028 | 0.315 | 0.371 | 2.699 | 1.420 | 3.479 | 0.914 |
| $\omega_y < 0$ | 0.307 | 0.354 | 2.693 | 1.712 | 3.482 | 1.085 | 0.317 | 0.361 | 2.721 | 1.463 | 3.185 | 0.865 |
| $\omega_z > 0$ | 0.212 | 0.240 | 1.758 | 1.054 | 2.025 | 0.634 | 0.231 | 0.256 | 1.865 | 0.936 | 2.020 | 0.447 |
| $\omega_z < 0$ | 0.354 | 0.367 | 3.174 | 2.350 | 5.503 | 2.940 | 0.351 | 0.385 | 3.148 | 1.988 | 5.211 | 2.417 |
| Parameter | C08P02 | | | | | | C10P00 | | | | | |
| | H | L | N | HN | NL | HNL | H | L | N | HN | NL | HNL |
| $\langle uv \rangle > 0$ | 0.409 | 0.579 | 3.330 | 1.780 | 4.938 | 1.585 | 0.436 | 0.505 | 3.102 | 1.424 | 3.556 | 0.877 |
| $\langle uv \rangle < 0$ | 0.511 | 0.404 | 2.734 | 1.613 | 2.760 | 0.713 | 0.660 | 0.420 | 3.086 | 1.991 | 2.809 | 0.887 |
| $\omega_x > 0$ | 0.506 | 0.509 | 3.144 | 1.870 | 4.030 | 1.141 | 0.573 | 0.470 | 3.272 | 1.953 | 3.438 | 0.929 |
| $\omega_x < 0$ | 0.438 | 0.491 | 3.199 | 2.021 | 4.368 | 1.313 | 0.568 | 0.472 | 3.267 | 1.869 | 3.415 | 0.901 |
| $\omega_y > 0$ | 0.484 | 0.537 | 3.332 | 1.663 | 3.689 | 0.870 | 0.610 | 0.520 | 3.346 | 1.630 | 3.062 | 0.664 |
| $\omega_y < 0$ | 0.512 | 0.547 | 3.299 | 1.806 | 3.813 | 0.903 | 0.586 | 0.498 | 3.344 | 1.688 | 3.019 | 0.660 |
| $\omega_z > 0$ | 0.397 | 0.380 | 2.374 | 1.287 | 2.416 | 0.552 | 0.467 | 0.360 | 2.413 | 1.242 | 2.043 | 0.478 |
| $\omega_z < 0$ | 0.542 | 0.585 | 3.857 | 2.353 | 5.865 | 1.995 | 0.663 | 0.558 | 3.948 | 2.302 | 4.718 | 1.511 |

Table 6.3: Vortex clusters area classified according to flow properties. Channel center. For each case its corresponding $\alpha_{opt}$ presented in Table 6.1 was employed.

| Parameter | C00P10 | | | | | | C02P08 | | | | | |
|---|---|---|---|---|---|---|---|---|---|---|---|---|
| | H | L | N | HN | NL | HNL | H | L | N | HN | NL | HNL |
| $\langle uv \rangle > 0$ | 0.185 | 0.237 | 2.178 | 1.383 | 3.089 | 1.282 | 0.194 | 0.232 | 2.241 | 1.469 | 3.458 | 1.477 |
| $\langle uv \rangle < 0$ | 1.070 | 0.063 | 1.846 | 3.388 | 0.666 | 0.885 | 1.023 | 0.068 | 1.969 | 3.431 | 0.660 | 0.824 |
| $\omega_x > 0$ | 0.419 | 0.183 | 1.826 | 3.118 | 2.186 | 1.972 | 0.406 | 0.185 | 1.946 | 3.098 | 2.383 | 2.214 |
| $\omega_x < 0$ | 0.410 | 0.184 | 1.869 | 2.974 | 2.265 | 2.149 | 0.399 | 0.181 | 1.932 | 3.197 | 2.473 | 2.273 |
| $\omega_y > 0$ | 0.473 | 0.154 | 1.837 | 2.576 | 1.946 | 1.990 | 0.465 | 0.162 | 2.014 | 2.619 | 2.077 | 2.084 |
| $\omega_y < 0$ | 0.482 | 0.155 | 1.875 | 2.615 | 1.960 | 1.986 | 0.469 | 0.162 | 1.987 | 2.671 | 2.178 | 2.027 |
| $\omega_z > 0$ | 0.057 | 0.024 | 1.170 | 0.589 | 1.010 | 0.227 | 0.071 | 0.029 | 1.246 | 0.718 | 1.008 | 0.264 |
| $\omega_z < 0$ | 0.531 | 0.244 | 2.424 | 4.894 | 2.785 | 6.696 | 0.535 | 0.249 | 2.612 | 4.850 | 3.043 | 6.804 |

| Parameter | C04P06 | | | | | | C06P04 | | | | | |
|---|---|---|---|---|---|---|---|---|---|---|---|---|
| | H | L | N | HN | NL | HNL | H | L | N | HN | NL | HNL |
| $\langle uv \rangle > 0$ | 0.195 | 0.214 | 2.105 | 1.413 | 3.060 | 1.237 | 0.180 | 0.190 | 1.997 | 1.340 | 2.684 | 1.154 |
| $\langle uv \rangle < 0$ | 0.991 | 0.056 | 1.839 | 3.180 | 0.618 | 0.739 | 0.945 | 0.047 | 1.784 | 2.984 | 0.524 | 0.503 |
| $\omega_x > 0$ | 0.399 | 0.161 | 1.877 | 2.881 | 2.212 | 1.612 | 0.395 | 0.146 | 1.775 | 2.838 | 1.932 | 1.712 |
| $\omega_x < 0$ | 0.403 | 0.165 | 1.833 | 2.990 | 2.225 | 2.053 | 0.382 | 0.148 | 1.810 | 2.747 | 2.057 | 1.504 |
| $\omega_y > 0$ | 0.459 | 0.145 | 1.889 | 2.467 | 1.917 | 1.651 | 0.435 | 0.129 | 1.815 | 2.363 | 1.697 | 1.550 |
| $\omega_y < 0$ | 0.443 | 0.145 | 1.862 | 2.590 | 1.952 | 1.834 | 0.457 | 0.131 | 1.822 | 2.309 | 1.737 | 1.331 |
| $\omega_z > 0$ | 0.057 | 0.024 | 1.101 | 0.632 | 0.887 | 0.215 | 0.067 | 0.024 | 1.108 | 0.587 | 0.799 | 0.157 |
| $\omega_z < 0$ | 0.540 | 0.222 | 2.443 | 4.794 | 2.874 | 6.008 | 0.518 | 0.194 | 2.394 | 4.610 | 2.651 | 4.878 |

| Parameter | C08P02 | | | | | | C10P00 | | | | | |
|---|---|---|---|---|---|---|---|---|---|---|---|---|
| | H | L | N | HN | NL | HNL | H | L | N | HN | NL | HNL |
| $\langle uv \rangle > 0$ | 0.167 | 0.143 | 1.536 | 1.035 | 1.934 | 0.868 | 0.215 | 0.149 | 1.804 | 1.380 | 1.917 | 0.966 |
| $\langle uv \rangle < 0$ | 0.749 | 0.041 | 1.344 | 2.314 | 0.352 | 0.327 | 0.980 | 0.040 | 1.525 | 2.633 | 0.368 | 0.369 |
| $\omega_x > 0$ | 0.318 | 0.109 | 1.437 | 2.171 | 1.390 | 1.231 | 0.412 | 0.117 | 1.633 | 2.879 | 1.374 | 1.184 |
| $\omega_x < 0$ | 0.331 | 0.113 | 1.413 | 2.254 | 1.406 | 1.184 | 0.423 | 0.113 | 1.655 | 2.770 | 1.442 | 1.134 |
| $\omega_y > 0$ | 0.389 | 0.103 | 1.484 | 1.812 | 1.127 | 0.990 | 0.475 | 0.105 | 1.671 | 2.294 | 1.185 | 1.044 |
| $\omega_y < 0$ | 0.355 | 0.102 | 1.418 | 1.807 | 1.177 | 1.029 | 0.492 | 0.103 | 1.642 | 2.227 | 1.211 | 0.978 |
| $\omega_z > 0$ | 0.060 | 0.022 | 0.938 | 0.568 | 0.602 | 0.155 | 0.084 | 0.022 | 1.018 | 0.588 | 0.507 | 0.126 |
| $\omega_z < 0$ | 0.466 | 0.146 | 1.860 | 3.455 | 1.816 | 3.379 | 0.581 | 0.148 | 2.163 | 4.565 | 1.882 | 3.831 |

Table 6.4: Vortex clusters area classified according to flow properties. Near the stationary wall. For each case its corresponding $\alpha_{opt}$ presented in Table 6.1 was employed.

| Parameter | C00P10 | | | | | | C02P08 | | | | | |
|---|---|---|---|---|---|---|---|---|---|---|---|---|
| | H | L | N | HN | NL | HNL | H | L | N | HN | NL | HNL |
| $\langle uv \rangle > 0$ | 0.479 | 0.353 | 2.585 | 1.617 | 2.099 | 0.863 | 0.318 | 0.229 | 2.261 | 2.617 | 3.068 | 2.216 |
| $\langle uv \rangle < 0$ | 0.572 | 0.492 | 3.253 | 1.792 | 2.099 | 0.632 | 0.443 | 0.269 | 2.909 | 3.020 | 3.074 | 1.589 |
| $\omega_x > 0$ | 0.529 | 0.387 | 3.064 | 2.244 | 2.801 | 1.145 | 0.363 | 0.211 | 2.544 | 3.124 | 3.603 | 3.030 |
| $\omega_x < 0$ | 0.517 | 0.384 | 3.089 | 2.164 | 2.678 | 1.198 | 0.336 | 0.223 | 2.617 | 3.232 | 3.589 | 2.763 |
| $\omega_y > 0$ | 0.547 | 0.421 | 3.133 | 2.056 | 2.422 | 0.786 | 0.428 | 0.264 | 2.672 | 3.366 | 3.494 | 2.329 |
| $\omega_y < 0$ | 0.555 | 0.424 | 3.143 | 2.004 | 2.474 | 0.766 | 0.368 | 0.215 | 2.858 | 3.271 | 3.636 | 2.552 |
| $\omega_z > 0$ | 0.652 | 0.518 | 3.992 | 3.319 | 4.549 | 5.223 | 0.530 | 0.315 | 3.960 | 5.300 | 6.338 | 10.24 |
| $\omega_z < 0$ | 0.200 | 0.150 | 1.244 | 0.637 | 0.742 | 0.126 | 0.029 | 0.016 | 0.291 | 0.385 | 0.298 | 0.114 |
| Parameter | C04P06 | | | | | | C06P04 | | | | | |
| | H | L | N | HN | NL | HNL | H | L | N | HN | NL | HNL |
| $\langle uv \rangle > 0$ | 0.351 | 0.217 | 2.542 | 2.736 | 4.373 | 4.126 | 0.116 | 0.107 | 1.206 | 1.294 | 2.332 | 2.047 |
| $\langle uv \rangle < 0$ | 0.466 | 0.320 | 3.444 | 3.370 | 4.794 | 4.550 | 0.143 | 0.100 | 1.102 | 0.950 | 1.339 | 0.860 |
| $\omega_x > 0$ | 0.385 | 0.219 | 2.819 | 3.551 | 5.483 | 5.207 | 0.126 | 0.106 | 1.221 | 1.244 | 2.054 | 1.561 |
| $\omega_x < 0$ | 0.328 | 0.248 | 3.016 | 3.422 | 5.224 | 5.936 | 0.135 | 0.097 | 1.150 | 1.246 | 2.012 | 1.816 |
| $\omega_y > 0$ | 0.357 | 0.298 | 3.444 | 3.785 | 5.510 | 3.967 | 0.162 | 0.108 | 1.262 | 1.237 | 1.897 | 1.408 |
| $\omega_y < 0$ | 0.489 | 0.279 | 3.447 | 3.956 | 5.469 | 4.044 | 0.147 | 0.127 | 1.316 | 1.185 | 1.901 | 1.242 |
| $\omega_z > 0$ | 0.586 | 0.363 | 4.499 | 6.143 | 9.465 | 18.59 | 0.048 | 0.032 | 0.316 | 0.267 | 0.515 | 0.250 |
| $\omega_z < 0$ | 0.007 | 0.006 | 0.051 | 0.029 | 0.048 | 0.007 | 0.170 | 0.128 | 1.736 | 2.028 | 3.521 | 4.836 |
| Parameter | C08P02 | | | | | | C10P00 | | | | | |
| | H | L | N | HN | NL | HNL | H | L | N | HN | NL | HNL |
| $\langle uv \rangle > 0$ | 0.238 | 0.253 | 1.899 | 1.293 | 2.483 | 0.968 | 0.273 | 0.268 | 1.948 | 0.909 | 1.350 | 0.351 |
| $\langle uv \rangle < 0$ | 0.262 | 0.327 | 2.220 | 1.342 | 1.970 | 0.746 | 0.347 | 0.353 | 2.310 | 1.048 | 1.450 | 0.347 |
| $\omega_x > 0$ | 0.210 | 0.282 | 2.219 | 1.586 | 2.729 | 1.380 | 0.316 | 0.298 | 2.319 | 1.400 | 1.857 | 0.513 |
| $\omega_x < 0$ | 0.261 | 0.276 | 2.229 | 1.600 | 2.730 | 1.274 | 0.317 | 0.288 | 2.337 | 1.321 | 1.959 | 0.597 |
| $\omega_y > 0$ | 0.254 | 0.346 | 2.291 | 1.510 | 2.574 | 0.879 | 0.331 | 0.327 | 2.278 | 1.121 | 1.511 | 0.324 |
| $\omega_y < 0$ | 0.299 | 0.317 | 2.317 | 1.460 | 2.449 | 0.874 | 0.339 | 0.325 | 2.342 | 1.061 | 1.594 | 0.310 |
| $\omega_z > 0$ | 0.060 | 0.071 | 0.605 | 0.313 | 0.407 | 0.079 | 0.127 | 0.125 | 1.051 | 0.456 | 0.540 | 0.068 |
| $\omega_z < 0$ | 0.360 | 0.395 | 3.359 | 2.664 | 4.772 | 4.564 | 0.450 | 0.410 | 3.164 | 2.051 | 3.238 | 1.873 |

Table 6.5: Vortex clusters area classified according to flow properties. Near the moving wall. For each case its corresponding $\alpha_{opt}$ presented in Table 6.1 was employed.

# Chapter 7

# Conclusions

A stepped transition from a pure Poiseuille to a pure Couette flow has been studied in channel domains of diverse length. Two main approaches were carried out. On the one hand, the streamwise velocity structures and the Reynolds stress at diverse regions were studied. On the other hand, an identification of the vortices present in the flow and a classification of their features were performed.

From the results obtained, the following conclusions were extracted:

- It is proven that the stability of the large counter-rotating rolls that extent from wall to wall is affected by the pressure gradient applied, as well as on the friction Reynolds number. In addition, the use of a small domain increases the intensity of the rolls due to the effect of the periodicity boundary conditions. In our study, these huge structures are present from case C06P04 to pure Couette.

- The presence of large counter-rotating rolls is demonstrated by the streaky pattern of the streamwise velocity structures in the channel center. This is observed in both instantaneous and mean velocity fields. Additionally, the distribution of Reynolds stress along the wall-normal direction describes the presence of these rolls.

- A link between the distribution of the mean Reynolds stress along the wall-normal dimension and the presence of the rolls is verified. As soon as the Reynolds stress distribution changes its arithmetical sign, the rolls are no longer present. As a result, this idea was published in detail in a scientific article [23], written by the authors of this thesis, among others.

- The region near the stationary wall remains almost unaffected by the movement of the upper wall. It was proven that the mean velocity and Reynolds stress show a good collapse in this region among cases. Additionally, other analysis, such as vortex distribution or velocity structures in this region, shown the same pattern for all cases.

- On the contrary, the region near the moving wall is highly affected by the movement of the wall. One can see a great disparity in the mean velocity and Reynolds stress profiles. Moreover, case C06P04 achieves in this region a low friction Reynolds number, which no longer sustains turbulence.

- The use of a threshold dependent on the distance to the wall results in most of the cases on a constant vortex population along the wall-normal dimension. This threshold becomes more restrictive near the walls in case of pure Couette or Poiseuille flows. However, its distribution is not symmetric in transition cases. In case of a constant threshold, the population shows great peaks near walls, and a severe decrease in the channel center.

- Vortex clusters tend to locate in the regions where the fluctuating streamwise velocity ($u'$) is below its standard deviation; that is, regions called neutral. Sometimes they also touch other high- or low-speed regions. However, seldom situate the vortex clusters only in regions where the absolute value of the fluctuating streamwise velocity is higher than its standard deviation.

# Chapter 8

# Project specifications

## 8.1 Workstation conditions

While conducting a project, the worker is under specific conditions that may affect their health as well as their performance. Due to this fact, it is necessary to regulate these working conditions in order to diminish the worker risks. The regulations covering the workstation conditions in Spain are gathered in *Real Decreto 488/1997*, released on 14th of April.

Regarding the conditions related to security and health while working with a computer and a screen, the regulation states in Spanish: *"el constituido por un equipo con pantalla de visualización provisto, en su caso, de un teclado o dispositivo de adquisición de datos, de un programa para la interconexión persona-máquina, de accesorios ofimáticos y de un asiento y mesa o superficie de trabajo"*.

The project planning must take care of at least four points in order to prevent the worker from diverse risks:

- Time spent working in front of a screen.
- Amount of time with a high degree of attention to the screen.
- Complexity and exigency of the tasks performed with a screen.
- The need of processing information fast.

On the contrary, the risks may arise from:

- Electric circuits
- Workstation hygiene: illumination, noise, ambient temperature, humidity...
- Ergonomics: visual, physical and mental fatigue.

### 8.1.1 Workspace

The workspace where the project tasks will be carried out, must stay in accordance with *Real Decreto 486/1997*, regarding on the minimum security and hygiene conditions present in the workspace. This also applies to additional spaces, where eventual project activities take place, such as meetings, experiments, and so on.

### 8.1.2 Emergency measures: paths and exits

The owner of the facilities must have implemented emergency measures. These include the required evacuation paths and exits, which would be employed in case of emergency. All these measures must be announced to the workers.

### 8.1.3 Protection against fire emergency

All measures against a fire emergency must be depicted, implemented and maintained by duly authorized companies.

### 8.1.4 Electrical wiring

The electrical wiring must be projected, operating and maintained by a duly authorized company. The installation must avoid any contact with workers, as well as ensure safe working conditions without possible ignition or explosion. Its specific regulations are collected in *Reglamentos de Baja y Alta Tensión*.

According to the regulations related to the use of screens, the electrical wiring must ensure:

- Piddling levels of electromagnetic radiation.
- Proper maintenance of wires and connections.
- Separation between electrical and phone wires.
- Use of wires long enough in order to perform future installation changes.
- Accessibility and maintenance of the wire without jeopardizing workers operations.

### 8.1.5 Ambient conditions

*Real Decreto 488/1997* established the following rules on ambient conditions in a workspace with computers and screens. This normative guarantees the well-being and comfort of the employees.

- The ambient temperature should stay in a range from 23 to 26°C in summer, or from 20 to 24°C in winter.
- Relative humidity should stay always between 45% and 65%.

### 8.1.6 Workspace lighting

The lighting can be natural or artificial, although natural light is more recommended. However, as its intensity depends on diverse factors, such as the hour of the day, the meteorology or the season, it must be complemented with artificial lighting. The lighting installation must avoid dazzle and excessive contrasts.

The lighting intensity should be suitable for the development of the project tasks. Additionally, the lights location and orientation should avoid too much reflected light and dazzle.

### 8.1.7 Ergonomics

The lack of ergonomics in the workspace is closely related to postural problems. Considering that the use of a screen means maintaining a static position during a long time, one can assure that an inappropriate position would reduce drastically the well-being of an employee. Therefore, the workspace tools must follow these indications.

The height and inclination of the chair must be adjusted according to the requirements of the employees. The chair back should have a smooth bump where the lower back can rest. It is recommended to use chairs with wheels; however, the wheels resistance must avoid involuntary movements.

The table surface must not be reflective, and its dimensions must allow the worker's movement and position change. Moreover, it must be wide enough to place a screen, a keyboard, documents and material.

The optimal distance between the user and the screen should be between 45 and 75 cm, to ensure visual comfort. The screen location should assure that the screen is inside the horizontal visual line and 60° below. In a horizontal plane, the screen must be located inside the user vision range of 70°.

The screen must be stable, and not reflective. Its contrast and lighting should be easily modified by the user. Furthermore, the screen orientation and inclination should adapt to the user requirements.

The keyboard must be inclined, and independent from the screen. In this manner, the employee has a correct position, which does not leads to physical pain.

It is highly recommended the use of a screen protector. This is a polarized plate, which is placed on the screen. Consequently, it protects the user eyesight and improves the image quality.

### 8.1.8 Noise

According to *Real Decreto 1316/1989*, the employer must measure the noise level in the workspaces, in order to estimate if the noise limits are exceeded. To avoid reaching the maximum at 55 dB, equipment with low noise emissions should be used, and the workspace acoustic should be improved.

## 8.2 Conditions of computer tools

The calculations performed in this project needed high performance computer tools. These tools are divided in: *hardware* and *software*.

Due to the huge size of the simulations, a high performance computer with large data storage was employed. This computer is connected to a local net, so it is accessible once connected through the university WiFi or VPN connection. Additionally, it allowed us to perform uninterrupted calculations that lasted several days. This kind of machines need a regular maintenance in order to ensure a high performance without interruptions.

On the other hand, a normal computer Acer E1-572 was used in this project for performing easy calculations, analysis, looking for information and writing the document.

Diverse softwares were used in this project. All simulation codes were written in FORTRAN programming language, which is open source. Then, the results post-processing and studies were performed with Matlab. Finally, the master thesis document is written in LaTeX.

### 8.2.1 Hardware conditions

- **Laptop Acer E1-572**

**Processor**: Intel Core i7 4500U at 1.8 GHz
**Number of processors**: 2
**RAM memory**: 8 GB
**ROM memory**: 750 GB
**Graphics card**: Intel HD Graphics
**OS**: Windows 10

### 8.2.2 Software conditions

- FORTRAN code

The code used for performing all simulations was written in FORTRAN. It is a general-purpose, compiled imperative programming language that is especially suited to numeric computation and scientific computing. It was originally developed by IBM in the 1950s for scientific and engineering applications.

- Matlab

All post-process routines were developed in Matlab, specifically for this project. Here, a student license was employed, which is available for all UPV students. The costs of this license according to Matlab webpage are specified among the project costs.

- LaTeX

This open-source software was used to write the thesis document. All packages are for free, and are developed by independent users. So, no costs arise from this software.

# Chapter 9

# Project costs

In this chapter the costs related to the duties and stages of this project will be evaluated. Thus, the project is chronologically divided, and the hours spent in each part are indicated. In each stage, a short explanation of its objectives and material employed is given. Later, the hours in each part are multiplied by the work cost in Euros per worked hour. This cost depends on the worker's qualification.

Among the material used, the costs related to the work office; i.e. table, chair, space and so on, will be added as indirect costs. The same occurs with the computer used for coding and post-processing, whereas the computer hours done in the supercomputer SuperMUC will not be considered, since it is not a part of this master thesis project.

In order to quantify the effort made by the staff, the units used are worked hours. Accordingly, the costs are expressed in Euros per worked hour.

## 9.1 Project stages

The master thesis was carried out by following these stages:

**1. Information compilation and processing**

First, read scientific papers published in the recent years, which are closely or partially related to the project topic. Second, understand the approaches employed by the authors, and take into account their limitations. Finally, look for other articles for a deeper understanding.
This stage is based on the use of papers, a printer, a laptop and office material.

**2. Post-process Matlab code implementation**

First, write the code for extracting the physical velocity fields from simulation files. Second, implement the identification method as well as other relevant algorithms described in Chapter 4. Notice that most of these codes require testing before applying them in this project.

**3. Post-process of velocity fields**

Here, the velocity field are treated in order to extract relevant information about the presence of the large counter-rotating rolls. This stage requires Matlab coding as well as critical analysis of the results. Moreover, the conclusions were published in Gandia-Barbera et al. [23]; hence, additional time was spent in this stage.

**4. Vortices identification**

Here, the vortices present in the velocity fields are identified, and classified. As well as in Stage 3, this part requires a critical analysis. In addition, as few authors performed this analysis, it required extra time to think about the proper approach.

**5. Report elaboration**

The report was elaborated using open-source software LaTeX. Hence, no additional cost due to software license is considered.

## 9.2 Budget

In this section the detailed budget for each stage is presented. The project supervisor is here referred as Superior Engineer, while the author is referred as Technical Engineer. The electricity price considered is 0.12 €/kWh. Additionally, the office is provided with four lights of 20 W each.

The material described in the first Stage refers to a notebook and several printed papers. The software license refers to a Matlab student license, and Fortran license.

- **First stage**

| Stage | Description | Hours | €/ Hour | Amount |
|---|---|---|---|---|
| 1 | Superior Engineer | 18 | 50 | 900 € |
| | Technical Engineer | 155 | 30 | 4650 € |
| | Material | 1 | 7.4 | 7.4 € |
| | Electricity | 155 | $9.6 \cdot 10^{-3}$ | 1.48 € |
| | Total | | | 5559 € |

Table 9.1: Budget for the first stage.

- **Second stage**

| Stage | Description | Hours | €/ Hour | Amount |
|---|---|---|---|---|
| 2 | Superior Engineer | 36 | 50 | 1800 € |
| | Technical Engineer | 312 | 30 | 9360 € |
| | Matlab License | 1 | 400 | 400 € |
| | Fortran License | 1 | 0 | 0 € |
| | Electricity | 312 | $9.6 \cdot 10^{-3}$ | 3 € |
| | Total | | | 11563 € |

Table 9.2: Budget for the second stage.

- **Third stage**

| Stage | Description | Hours | €/ Hour | Amount |
|---|---|---|---|---|
| 3 | Superior Engineer | 50 | 50 | 2500 € |
| | Technical Engineer | 260 | 30 | 9360 € |
| | Electricity | 260 | $9.6 \cdot 10^{-3}$ | 2.5 € |
| | Total | | | 11863 € |

Table 9.3: Budget for the third stage.

- **Forth stage**

| Stage | Description | Hours | €/ Hour | Amount |
|---|---|---|---|---|
| 4 | Superior Engineer | 24 | 50 | 1200 € |
| | Technical Engineer | 126 | 30 | 3780 € |
| | Electricity | 156 | $9.6 \cdot 10^{-3}$ | 1.5 € |
| | Total | | | 4981.5 € |

Table 9.4: Budget for the forth stage.

- **Fifth stage**

| Stage | Description | Hours | €/ Hour | Amount |
|---|---|---|---|---|
| 5 | Superior Engineer | 10 | 50 | 500 € |
| | Technical Engineer | 144 | 30 | 4320 € |
| | LaTeX License | 1 | 0 | 0 € |
| | Electricity | 144 | $9.6 \cdot 10^{-3}$ | 1.38 € |
| | Total | | | 4821.4 € |

Table 9.5: Budget for the fifth stage.

- **Project cost**

| Stage | First | Second | Third | Forth | Fifth | Project Cost |
|---|---|---|---|---|---|---|
| Cost | 5559 € | 11563 € | 11863 € | 4981.5 € | 4821.4 € | 38788 € |

Table 9.6: Budget summary.

- **Additional cost**

+ Additional Cost = 11636 €

+ IVA = 10589 €

- **Total cost**

The total cost of the project is:

**sixty-one thousand thirteen €.**

# Bibliography


[1] S. B. Pope. *Turbulent flows*. Cambridge University Press, 2000.

[2] J. Jiménez. Near-wall turbulence. *Physics of Fluids*, 25(10):101302, 2013.

[3] S. Pirozzoli, M. Bernardini, and P. Orlandi. Large-scale motions and inner/outer layer interactions in turbulent Couette—Poiseuille flows. *Journal of Fluid Mechanics*, 680:534–563, 2011.

[4] N. Tillmark. *Experiments on transition and turbulence in plane Couette flow.* PhD thesis, KTH, Royal Institute of Technology, 1995.

[5] O. Kitoh and M. Umeki. Experimental study on large-scale streak structure in the core region of turbulent plane Couette flow. *Physics of Fluids*, 20(2):025107, 2008.

[6] K. Bech, N. Tillmark, P. Alfredsson, and H. Andersson. An investigation of turbulent plane Couette flow at low Reynolds numbers. *Journal of Fluid Mechanics*, 286:291–325., 1995.

[7] S. Pirozzoli, M. Bernardini, and P. Orlandi. Turbulence statistics in couette flow at high reynolds number. *Journal of Fluid Mechanics*, 758:323–343, 2014.

[8] M. Lee and R. Moser. Extreme-scale motions in turbulent plane couette flows. *Journal of Fluid Mechanics*, 842:128–145, 2018.

[9] Yoshinobu Yamamoto and Yoshiyuki Tsuji. Numerical evidence of logarithmic regions in channel flow at $Re_\tau = 8000$. *Physical Review Fluids*, 3:012602(R), 2018.

[10] H. Tennekes and J. L. Lumley. *A First Course in Turbulence*. MIT Press, 1973.

[11] J. Kim, P. Moin, and R. Moser. Turbulence statistics in fully developed channels flows at low Reynolds numbers. *Journal of Fluid Mechanics*, 320:259–285, 1987.

[12] Sergio Hoyas and Javier Jiménez. Scaling of the velocity fluctuations in turbulent channels up to $Re_\tau = 2003$. *Physics of Fluids*, 18(1):011702, 2006.

[13] S. Hoyas and J. Jiménez. Reynolds number effects on the Reynolds-stress budgets in turbulent channels. *Physics of Fluids*, 20(10):101511, 2008.

[14] V. Avsarkisov, S. Hoyas, M. Oberlack, and J.P. García-Galache. Turbulent plane Couette flow at moderately high reynolds number. *Journal of Fluid Mechanics*, 751:R1, 2014.

[15] V. Avsarkisov, M. Oberlack, and S. Hoyas. New scaling laws for turbulent Poiseuille flow with wall transpiration. *Journal of Fluid Mechanics*, 746:99–122, 2014.

[16] S. Kraheberger, S. Hoyas, and M. Oberlack. Dns of a turbulent couette flow at constant wall transpiration up to $Re_\tau = 1000$. *Journal of Fluid Mechanics*, 835:421–443, 2018.

[17] F. Lluesma-Rodríguez, S. Hoyas, and MJ Peréz-Quiles. Influence of the computational domain on dns of turbulent heat transfer up to $Re_\tau = 2000$ for $Pr = 0.71$. *International Journal of Heat and Mass Transfer*, 122:983–992, 2018.

[18] S. K. Lele. Compact finite difference schemes with spectral-like resolution. *Journal of Computational Physics*, 103(1):16–42, 1992.

[19] Philippe R Spalart, Robert D Moser, and Michael M Rogers. Spectral methods for the Navier-Stokes equations with one infinite and two periodic directions. *Journal of Computational Physics*, 96(2):297–324, 1991.

[20] T. Tsukahara, H. Kawamura, and K. Shingai. DNS of turbulent Couette flow with emphasis on the large-scale structure in the core region. *Journal of Turbulence*, 7:1–16, 2006.

[21] M. Bernardini, S. Pirozzoli, and P. Orlandi. The effect of large-scale turbulent structures on particle dispersion in wall-bounded flows. *International Journal of Multiphase Flow*, 51:55–64, 2013.

[22] A. Lozano-Durán and J. Jiménez. Effect of the computational domain on direct simulations of turbulent channels up to $Re_\tau = 4200$. *Physics of Fluids*, 26(1):011702, 2014.

[23] Sergio Gandía-Barberá, Sergio Hoyas, Martin Oberlack, and Stefanie Kraheberger. Letter: The link between the Reynolds shear stress and the large structures of turbulent Couette-Poiseuille flow. *Physics of Fluids*, 30(4):041702, 2018.

[24] Cezary Prus. Coherent structures identification in turbulent duct flow and analysis of their influence on secondary flow based on dns data. Master's thesis, KTH Stockholm, 2018.

[25] P. Chakraborty, S. Balachandar, and R.J. Adrian. On the relationships between local vortex identification schemes. *Journal of fluid mechanics*, 535:189–214, 2005.

[26] J. C. del Álamo, J. Jiménez, P. Zandonade, and R. Moser. Self-similar vortex clusters in the turbulent logarythmic region. *Journal of Fluid Mechanics*, 561:329–358, 2006.

[27] M.S. Chong, A.E. Perry, and B.J. Cantwell. A general classification of three-dimensional flow fields. *Journal of Physics A.*, 2(5):765–777, 1990.

[28] M. J. Lee and J. Kim. The structure of turbulence in a simulated plane couette flow. *Proceedings of the 8th Symposium on Turbulent Shear Flows, Munich*, pages 5.3.1–5.3.6., 1991.

[29] Moon Joo Lee, John Kim, and Parviz Moin. Structure of turbulence at high shear rate. *Journal of Fluid Mechanics*, 216:561–583, 1990.

[30] K. Lam and S. Banerjee. On the condition of streak formation in a bounded turbulent flow. *Physics of Fluids A: Fluid Dynamics*, 4(2):306–320, 1992.